DEVELOPMENT OF DIFFUSE SOURCE UPSCALING

A Thesis

by

PENG ZHOU

Submitted to the Office of Graduate and Professional Studies of
Texas A&M University
in partial fulfillment of the requirements for the degree of

MASTER OF SCIENCE

Chair of Committee,	Michael J. King
Committee Members,	Akhil Datta-Gupta
	Richard Gibson
Head of Department,	Dan Hill

December 2015

Major Subject: Petroleum Engineering

Copyright 2015 Peng Zhou

ABSTRACT

Recently, a novel diffuse source (DS) upscaling method has been successfully applied for the upscaling of US tight gas reservoir model. However, this approach does not work very well in the conventional SPE10 waterflood reservoir model. Therefore, in this work, the goal is to figure out why this approach does not work in another model and how to improve this DS upscaling algorithm.

Detailed analysis shows that there are three issues that need to be resolved for a more robust algorithm. The first issue is about the specification of the diffuse source time that is needed to define the transient state diffuse source in the fine cell. In the previous work, the time selection rule is not clearly stated. Too small or too large time values can lead to an overestimated or underestimated upscaling result. In this study, I find that the diffuse source time can be correlated with the fine cell diffusive time of flight (DTOF). By means of a series of sensitivity test, I get the conclusion that we can use the pore volume weighted average of the DTOF square to determine the diffuse source time.

The second issue is related to the calculation of the effective transmissibility. In the case of upscaling the homogenous model, the previous proposed effective transmissibility calculation method gives us a wrong result. In this study, by studying the internal pressure profile in the coarse cells, I propose to use the fine cell pressures immediately adjacent to the coarse cell interface to determine an effective face permeability and apply the effective permeability to the calculation of steady state transmissibility in the simulator. The

effective transmissibility obtained from this method is correct when the model is homogenous.

The third issue has to do with the no flow boundary condition used in the local upscaling. In upscaling, we often encounter such problem that the no flow boundary condition is a bad approximation and to improve the accuracy of the result, we need to consider the existence of boundary effect. In this study, I generalize the DS upscaling algorithm by adding a buffering region around the upscaling coarse cells to reduce the impact of unrealistic boundary condition on the inter-cell effective transmissibility calculation. The buffering region is determined according to the fine cell DTOF in the target coarse cells and by using the exponential function in the diffuse source term, I propose a cut-off criterion to exclude the cells that are not necessary for upscaling.

Based on all the analysis above, I applied an improved upscaling algorithm for the upscaling of the SPE10 model. It turns out that the simulation results from the new upscaled model have a good match with the fine scale results, which gives us the confidence on this improved algorithm.

DEDICATION

To my wife Chen Lin, my son Samuel Zhou and my daughter Elim Zhou

for their endless support, love and encouragement

ACKNOWLEDGEMENTS

I would like to thank my committee chair, Dr. Michael King, who provides me the opportunity, financial support and tremendous guidance so that I can complete my master program. Sincere thanks to my other committee members, Dr. Akhil Datta-Gupta, and Dr. Richard Gibson, for their guidance during the course of this research.

Special thanks to all the members in the Model Calibration and Efficient Reservoir Imaging (MCERI) research group. Every person I met during the course of my masters has had an influence on my work. Especially, I would like to thank my colleague, Krishna Nunna, for his great help.

In the end, I would not finish my master program in two years without the support from my wife, my lovely son and my lovely daughter. Their support and encouragement are always important no matter where I am.

NOMENCLATURE

c_t	Total compressibility; psi^{-1};
h	Formation thickness; ft;
k	Permeability; mD;
$\vec{\vec{k}}$	Permeability tensor; mD;
q	Darcy flux; RB/day;
r	Radius of investigation; ft;
t	Time; hour;
p	Pressure; psi;
A	Cross sectional area; ft^2;
L	Length; ft;
V_p	Drainage volume; ft^3;

Subscripts

avg	Average
eff	Effective
H	Horizontal
i	Index
w	Well

Greek variables and operators

α	Hydraulic diffusivity

τ	Diffusive time of flight
μ	Fluid viscosity
ϕ	Porosity
∇	Gradient

Abbreviations

BRV	Bulk Rock Volume
PV	Pore volume
RB	Reservoir Barrel
SS	Steady State
DS	Diffuse source
PSS	Pseudo steady state
DTOF	Diffusive time of flight

TABLE OF CONTENTS

Page

LIST OF FIGURES

Page

Page

Page

Page

LIST OF TABLES

CHAPTER I

INTRODUCTION

Reservoir simulation is one of the most important tools in the modern petroleum industry as it provides the means for many purposes such as history matching, the prediction of reservoir response and the assessment of uncertainty and risk in reservoir performance. A primary input in reservoir simulation is a reservoir model which is typically in the form of a high resolution 3D geological model that incorporates various scales of data derived from well logs, seismic data, and sedimentology. The progress in computer hardware and software facilitates the performance of flow simulation. Geological models, however, often still contain many more grid cells than reservoir simulators can handle in practical time frames. Thus techniques are required to make realistic flow predictions applicable without performing simulation on very detailed geological models.

Even though we may use parallel computation techniques to save simulation time, the reduction of the number of equations to be solved is another good way to improve the simulation performance. Upscaling is a set of techniques that determine the coarse-scale properties such that important flow characteristics observed in fine-scale models is preserved in the coarse-scale models. Therefore, the use of upscaling procedures also acts to reduce the computational time for direct numerical simulation. In 3D reservoir modeling and simulation, upscaling of the geological models for flow simulation remains part of the subsurface workflows.

1.1 Literature review

In this section, the current existing upscaling algorithms are reviewed. Broadly speaking, upscaling procedures can be classified into traditional upscaling methods and multiscale upscaling methods. In traditional upscaling, the coarse scale parameters (e.g., porosity, absolute permeability or transmissibility) are calculated by using some kind of averaging technique and then the simulation is conducted based on the coarse grid model. In contrast, multiscale upscaling performs an upscaling calculation during a flow simulation and is not available in commercial general purpose simulators. Traditional upscaling methods can be further classified into analytical methods and flow based upscaling methods.

1.1.1 Analytical upscaling methods

The analytical upscaling methods are easy to implement and are suitable for the upscaling of some static petrophysical parameters (e.g., porosity). However, these methods have their limitations when they are used to upscale dynamic petrophysical parameters (e.g., permeability) because the analytical solution can only represent a few simple flow scenarios. Here we will focus on permeability upscaling using analytical methods (Renard and de Marsily, 1997).

The easiest analytical method of permeability upscaling is to calculate the arithmetic average of all the permeabilities. This averaging technique can be applied for a stratified reservoir where the fluid flow is along the layers of the stratified media, as shown by the left picture in **Figure 1**. The average permeability is given by **Eq. (1.1)**.

$$\mathrm{k_{avg}} = \frac{\sum_{\mathrm{i}=1}^{\mathrm{N}} \mathrm{k_i h_i}}{\sum_{\mathrm{i}=1}^{\mathrm{N}} \mathrm{h_i}} \dots\dots\dots\dots\dots\dots\dots\dots\dots\dots\dots\dots\dots\dots\dots\dots\dots\dots\dots\dots\dots\dots\dots\dots\dots\dots \,(1.1)$$

where $\mathrm{k_{avg}}$ is the average permeability, $\mathrm{k_i}$ the permeability of the ith layer, and $\mathrm{h_i}$ the thickness of the ith layer.

In contrast, from the picture on the right side of **Figure 1**, we see the fluid flows across different layers of a stratified media. For this flow pattern, we can use the harmonic averaging method to calculate the effective vertical permeability:

$$\mathrm{k_{avg}} = \frac{\sum_{\mathrm{i}=1}^{\mathrm{N}} \mathrm{h_i}}{\sum_{\mathrm{i}=1}^{\mathrm{N}} \frac{\mathrm{h_i}}{\mathrm{k_i}}} \dots\dots\dots\dots\dots\dots\dots\dots\dots\dots\dots\dots\dots\dots\dots\dots\dots\dots\dots\dots\dots\dots\dots\dots\dots\dots \,(1.2)$$

Figure 1: Arithmetic average (left) and harmonic average (right) (King 2011)

If we have a problem that is not as simple as we see in the first two cases we just discussed, we can use another simple analytical technique to calculate the effective permeability. This method is called geometric averaging and can be applied to two dimensional flow in an isotropic random field. The equation we use in this method is given by as follows:

$$\log\left(\mathrm{k_{avg}}\right) = \frac{\sum_{i=1}^{N} \mathrm{BRV_i} \log(\mathrm{k_i})}{\sum_{i=1}^{N} \mathrm{BRV_i}} \ldots\ldots\ldots\ldots\ldots\ldots\ldots\ldots\ldots\ldots\ldots\ldots\ldots. (1.3)$$

where BRV is the bulk rock volume of the cell.

All of the above permeability averaging techniques are special cases of a simple generalized formula shown in **Eq. (1.4)**.

$$\mathrm{k_{avg}} = \left(\frac{1}{N}\sum_{i=1}^{N} \mathrm{k_i^p}\right)^{\frac{1}{p}} \ldots\ldots\ldots\ldots\ldots\ldots\ldots\ldots\ldots\ldots\ldots\ldots\ldots. (1.4)$$

Harmonic, geometric and arithmetic averages are power averages with exponents of -1, 0, and 1 respectively. Power averages are more general and may be computed for any real valued exponent, but an important result of permeability averaging theory is that all effective permeabilities must correspond to a power average with an exponent in the range of -1 to 1. That is, all effective permeabilities must be between harmonic and arithmetic averages regardless of the spatial geometry.

Harmonic-arithmetic and arithmetic-harmonic averaging are another two simple averaging methods. In **Figure 2** we have a 2D conceptual picture for the harmonic-arithmetic averaging. The effective permeability is the arithmetic average of several core flooding and the cross flow between layers is neglected (Warren, J.E. and Price, H.S., 1961). This provides a rigorous lower bound estimate of the average permeability.

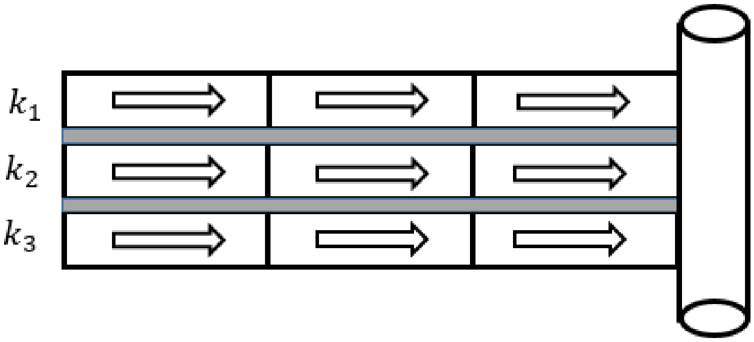

Figure 2: Harmonic-arithmetic average (King 2011)

In contrast, **Figure 3** is a conceptual picture for the arithmetic-harmonic averaging. In this figure, each column of the model is assumed to be subject to a uniform pressure drop along the flow direction. We assume that in the transverse direction the pressure is in the equilibrium state (Warren, J.E. and Price, H.S., 1961). Arithmetic-harmonic averaging provides a rigorous upper bound estimate of the average permeability.

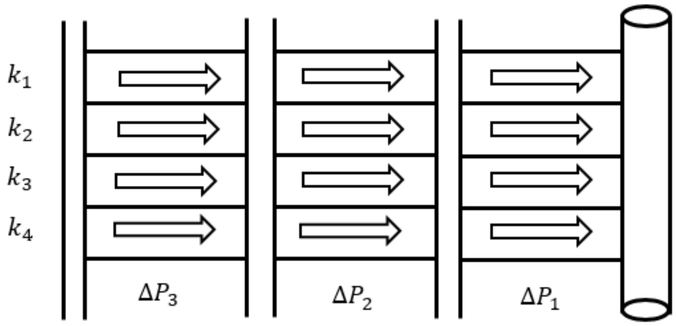

Figure 3: 2D arithmetic-harmonic average (King 2011)

Based on arithmetic-harmonic and harmonic-arithmetic averaging, we can obtain the effective permeability by using **Eq. (1.5)** (**Figure 4**).

$$\mathrm{k_{avg}} = \sqrt{\mathrm{k_{max}k_{min}}} \dots \dots \dots \dots \dots \dots \dots \dots \dots \dots \dots \dots \dots \dots \dots \dots \dots \dots \dots \dots \dots \dots \dots \dots \dots \dots \dots \dots \dots (1.5)$$

where $\mathrm{k_{max}}$ is the averaged permeability from arithmetic-harmonic averaging and $\mathrm{k_{min}}$ the averaged permeability from harmonic-arithmetic averaging.

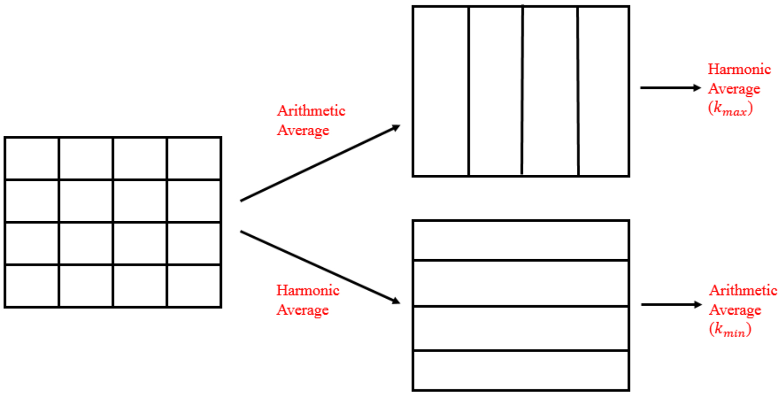

Figure 4: Incomplete layer method (Kelkar and Perez (2002))

In addition to all those simple averaging techniques, there are some relatively complicated methods which are designed to incorporate more realistic flow scenario. Firstly, I will introduce the percolation theory. This is a statistical method that deals with the problem of communication within a complex system. The critical point at which flow happens is called the percolation threshold. In the context of equivalent permeability, percolation theory is applied to materials with two phases, one of which is non permeable. For example, in **Figure 5**, consider all permeability below a threshold to be non-flowing and decrease the threshold until the percolation threshold is reached to give the equivalent permeability of the block. This approach works best for large models with many flow paths (Ambegaokar et al, 1971).

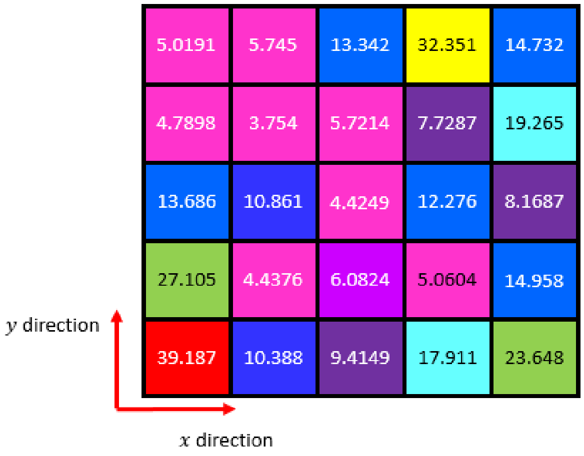

5.0191	5.745	13.342	32.351	14.732
4.7898	3.754	5.7214	7.7287	19.265
13.686	10.861	4.4249	12.276	8.1687
27.105	4.4376	6.0824	5.0604	14.958
39.187	10.388	9.4149	17.911	23.648

Figure 5: Percolation theory (King 2011)

Dagan (1979) proposed an effective medium theory for the calculation of the effective permeability. The heterogeneous medium constituted by homogeneous blocks placed side by side is replaced by a single inclusion of K permeability embedded in a homogeneous matrix with an unknown permeability. The boundary conditions are far enough away from the inclusion for the assumption to be made that the head gradient, and therefore the flow, is uniform on the boundary. If the inclusion has a simple form, there is an analytical solution for the hydraulic head field inside and outside it. Otherwise, the coupled two domain problem needs to be solved numerically and iteratively.

The streamline method is used to calculate the effective vertical permeability of a binary sand-clay system. The clay formations are treated as rectangles (in 2D) or flat parallelepipeds (3D) with zero permeability, while the sand is assumed to have k_{hj} and k_{vj} anisotropic permeabilities. The upscaled permeability is obtained by calculating the head losses along a tortuous tube circulating inside the sand matrix. An improvement on this method is obtained by incorporating statistical parameters on the size and number of clay inclusions and generalizing it to stratified media. The following formula is taken from the review by Fayers and Hewett (1992):

$$\mathrm{K_v} = \frac{(1 - \mathrm{F_s})\mathrm{H}^2}{\mathrm{N_s} \sum_{\mathrm{i}=1}^{\mathrm{N_s}} \frac{1}{\mathrm{S_i S_{ei}}}} \dots \dots \dots \dots \dots \dots \dots \dots \dots \dots \dots \dots \dots \dots \dots \dots \dots \dots \dots \dots \dots \dots \dots \dots \dots \dots \dots \dots \dots \dots \dots \dots (1.6)$$

where $\mathrm{F_s}$ is the fraction of clay inclusions, $\mathrm{N_s}$ the number of selected streamlines, H the formation thickness, $\mathrm{S_i}$ the length of the ith streamline and $\mathrm{S_{ei}}$ the length weighted by the permeability.

King (1989) proposed a recursive algorithm which is called renormalization. In this method effective permeability ($\mathrm{k_{eff}}$) is determined by a series of successive aggregations using an electric network analogy to porous media. It is a fast numerical calculation but less accurate than a non-recursive calculation.

The last analytical upscaling approach I will introduce is well index upscaling. King et al. (1998) proposed a well index upscaling method to preserve the connection between the well blocks and the reservoir. In this approach, the productivity of any physical well would be a weighted average of the productivities of three hypothetical directional wells (x, y and z direction) placed through the coarse cell. The upscaled productivity of each directional well is the weighted average of directional well productivities through each fine cell. **Figure 6** is an example for a vertical well productivity upscaling. The equations for directional well productivities are

$$\left(\sqrt{\mathrm{k_x.k_y}}\right)^{\mathrm{Effective}} = \frac{\sum_{\mathrm{ijk}}\left(\sqrt{\mathrm{k_x k_y}}.\mathrm{NTG.DV}\right)_{\mathrm{ijk}}}{\sum_{\mathrm{ijk}}(\mathrm{NTG.DV})_{\mathrm{ijk}}} \ldots\ldots\ldots\ldots\ldots\ldots\ldots.\ldots\ldots\ldots\ldots\ldots\ldots\ldots\ldots (1.7.1)$$

$$\left(\sqrt{\mathrm{k_y.k_z}}\right)^{\mathrm{Effective}} = \frac{\sum_{\mathrm{ijk}}\left(\sqrt{\mathrm{k_y k_z.NTG}}.\mathrm{DV}\right)_{\mathrm{ijk}}}{\sum_{\mathrm{ijk}}\left(\sqrt{\mathrm{NTG}}.\mathrm{DV}\right)_{\mathrm{ijk}}} \ldots\ldots\ldots\ldots\ldots\ldots\ldots\ldots\ldots\ldots.\ldots\ldots\ldots\ldots\ldots (1.7.2)$$

$$\left(\sqrt{\mathrm{k_x.k_z}}\right)^{\mathrm{Effective}} = \frac{\sum_{\mathrm{ijk}}\left(\sqrt{\mathrm{k_x k_z.NTG}}.\mathrm{DV}\right)_{\mathrm{ijk}}}{\sum_{\mathrm{ijk}}\left(\sqrt{\mathrm{NTG}}.\mathrm{DV}\right)_{\mathrm{ijk}}} \ldots\ldots..\ldots\ldots\ldots\ldots\ldots\ldots\ldots\ldots\ldots\ldots\ldots\ldots.. (1.7.3)$$

where NTG is the net to gross ratio, DV bulk volume of the grid block, $\mathrm{k_x, k_y, k_z}$ are the directional permeability in $\mathrm{x, y, z}$ directions, respectively.

The average cell permeabilities can be obtained from the directional well productivities as shown below.

$$\mathrm{k_x^{Effective}} = \frac{\left(\sqrt{\mathrm{k_x.k_y}}\right)^{\mathrm{Effective}}.\left(\sqrt{\mathrm{k_x.k_z}}\right)^{\mathrm{Effective}}}{\left(\sqrt{\mathrm{k_y.k_z}}\right)^{\mathrm{Effective}}} \ldots\ldots\ldots\ldots\ldots\ldots.\ldots\ldots\ldots\ldots\ldots\ldots\ldots. (1.8.1)$$

$$\mathrm{k_y^{Effective}} = \frac{\left(\sqrt{\mathrm{k_x.k_y}}\right)^{\mathrm{Effective}}.\left(\sqrt{\mathrm{k_y.k_z}}\right)^{\mathrm{Effective}}}{\left(\sqrt{\mathrm{k_x.k_z}}\right)^{\mathrm{Effective}}} \ldots\ldots\ldots\ldots\ldots\ldots\ldots\ldots\ldots\ldots.\ldots\ldots\ldots. (1.8.2)$$

$$k_z^{\text{Effective}} = \frac{\left(\sqrt{k_x . k_z}\right)^{\text{Effective}} . \left(\sqrt{k_y . k_z}\right)^{\text{Effective}}}{\left(\sqrt{k_x . k_y}\right)^{\text{Effective}}} \ldots\ldots\ldots\ldots\ldots\ldots\ldots\ldots\ldots\ldots\ldots\ldots\ldots\ldots (1.8.3)$$

The simulator can use these permeabilities to calculate the productivity of a physical well placed on the coarse cell which is equal to the averaged productivity of a well with the same inclination on the fine scale. This method does not require the knowledge of rates or locations of the physical wells which will eventually be placed in the flow simulator. Therefore, the approach is significantly simple to implement.

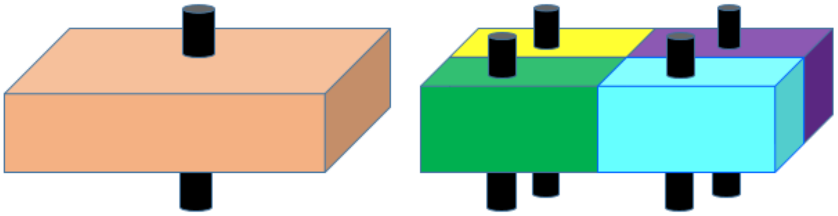

Figure 6: Well index upscaling method (King et al. (1998))

1.1.2 Flow based upscaling methods

Flow based upscaling is another approach that can generate more accurate coarse models compared to the analytical techniques. The basic equation used in flow based upscaling is the steady state diffusivity equation and it can be classified into single phase and two phase upscaling in terms of the flow parameters to be upscaled. In single phase upscaling, the only parameters to be upscaled are porosity and the absolute permeability. In the more general case of two phase upscaling, relative permeability and fluid saturation are also upscaled (Darman et al. 2002). In many cases we may develop reasonably accurate coarse scale models for two phase flow with only single phase upscaling. In addition, relative permeability upscaling is often computationally demanding and its value also depends on the flow rates, well spacing and water saturation. Therefore, two phase upscaling is rarely used (Barker and Thibeau, 1997) and is out of the current scope in this study.

In addition to the classification based on the fluid phase, flow-based upscaling can also be divided into four different types according to a two-stage upscaling procedure (Farmer, 2002). The first stage is related to the flow problem which is solved on the fine scale domain. If the fine scale domain is the entire domain or a substantial part of the whole domain, then it is called global. If only a small portion of the whole domain is used, then we call it local. The second stage is called the coarse grid calibration stage where the fine scale solutions from the first stage are used to determine the coarse scale properties (e.g., permeability, k). When the calibration occurs locally on a coarse cell or a coarse cell plus a small surrounding region, it is described as local, otherwise the calibration is said to be global.

The first type is local-local upscaling. The most popular local-local upscaling in the industry is cell permeability upscaling which has been extensively studied by many researchers (Durlofsky, 2005; Farmer, 2002; Gerritsen and Durlofsky, 2005; Renard and de Marsily, 1997; Wen and Gómez-Hernández, 1996; Christie, 1996). **Figure 7** below is a 2D example of permeability upscaling where an upstream pressure p_{in} is specified on the left face and a downstream pressure p_{out} on the right face of the coarse cell. The side boundary conditions are assumed to be no-flow. We can also assume other boundary conditions (e.g., linear pressure boundary or periodic boundary). The solution of fine cell pressure will be used to calculate the total flux q across the coarse cell face. Then the effective permeability is obtained from Darcy's law **Eq. (1.9)**. The local calculation is implemented in three co-ordinate directions to get the diagonal effective permeability tensor. This method was first introduced by Warren and Price (1961) and extended by Begg et al. (1989).

$$k_{eff} = \frac{q\mu L}{A(p_{out} - p_{in})} \quad \ldots\ldots\ldots\ldots\ldots\ldots\ldots\ldots\ldots\ldots\ldots\ldots\ldots\ldots\ldots\ldots\ldots\ldots\ldots\ldots (1.9)$$

where k_{eff} is the effective permeability of the coarse cell, q flux across the coarse cell, μ fluid viscosity, A cross sectional area of the coarse cell and L length of the coarse cell.

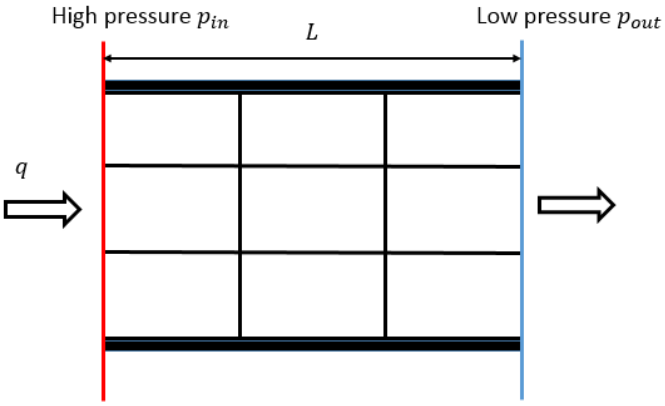

Figure 7: Permeability upscaling

In permeability upscaling, the upscaling result is affected by the choice of the boundary conditions (Holden and Nielsen, 2000). Therefore, some researchers (Gomez-Hernandez and Journel, 1994) try to add a skin region outside the upscaling region in order to remove the ambiguity of the results brought by boundary conditions (**Figure 8**). The average permeability is determined only using the region of interest. The larger the skin is, the higher would be the computational time. Therefore, skin may be introduced only in directions transverse to the flow to optimize the performance. King (2007) suggested the use of extended local or wide boundary conditions as it is less expensive than adding skin to the local region.

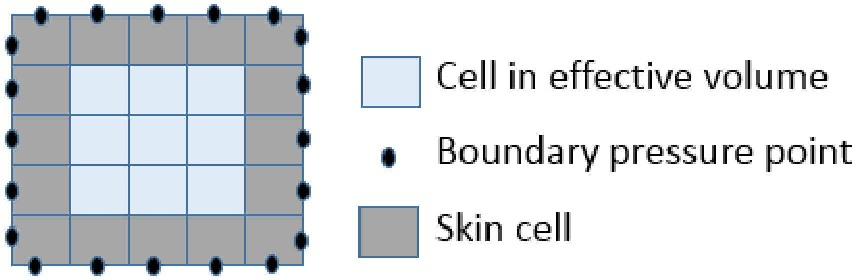

Figure 8: Adding skin region in local-local upscaling

To minimize the non-uniqueness of the results, we can perform an upgridding error analysis (King, 2007) prior to upscaling to minimize the heterogeneity within the upscaling region.

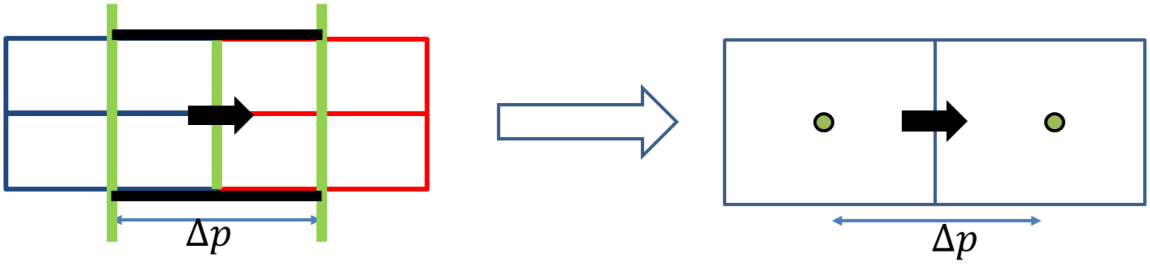

Figure 9: Plane source upscaling

Another local-local upscaling is transmissibility upscaling, which is a variation on cell permeability upscaling. **Figure 9** above is a picture for plane source upscaling, which is also called half-cell transmissibility upscaling. In plane source upscaling, two pressure isobars are placed at the centers of the two coarse cells respectively with the pressure difference be specified as $\Delta \mathrm{p}$. Numerically we solve the incompressible diffusivity equation for the flux q flowing across the coarse cell interface and then the transmissibility between two coarse cells is defined by the expression $\mathrm{q}/\Delta \mathrm{p}$. This provides more accurate coarse scale models in many cases because it does not require the additional approximations which results from the calculation of transmissibility using the harmonic average of the grid block upscaled permeability (King et al., 1998; Chen et al., 2003). This advantage can also be shown by considering the horizontal flow between two adjacent columns of cells. In cell permeability upscaling, the effective permeability of each column is equal to the arithmetic averaging of the permeability of fine cells in the column, and the inter-cell transmissibility is then calculated from the harmonic average of the two effective coarse cell permeability. In contrast, if half-cell transmissibility upscaling is used, then the transmissibility will be calculated on each single layer first and the final effective transmissibility will be the arithmetic averaging of each single layer transmissibility. Therefore, in the case, the cell permeability upscaling will results in an arithmetic-harmonic averaged transmissibility, while the half-cell transmissibility upscaling produces a harmonic-arithmetic averaged transmissibility.

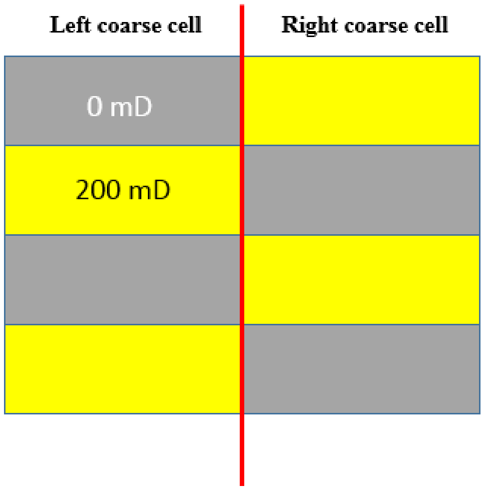

Figure 10: Permeability upscaling vs. transmissibility upscaling

Figure 10 above is a picture that illustrates the discussion we just made. The yellow boxes represent the cells with permeability equal to 200 mD, while the grey boxes represent the cells with zero permeability. If we use cell permeability upscaling technique to calculate the inter-cell transmissibility between these two coarse cells, then we will get a nonzero value of 100 mD. However, from this figure, it is obvious that there is no flow between these two coarse cells. Therefore, from this figure we can see the advantage of half-cell transmissibility upscaling over the cell permeability upscaling. Another advantage is that the half-cell transmissibility improves the spatial resolution of the upscaling calculation compared with the cell permeability upscaling which uses all the fine cells within each coarse cell.

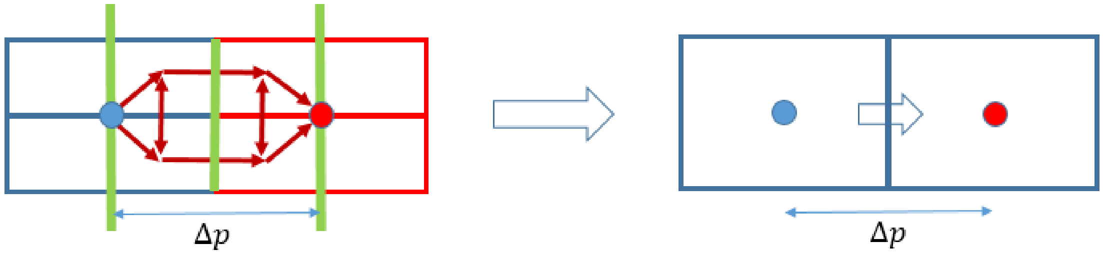

Figure 11: Line source upscaling (Nunna 2014)

In addition to plane source upscaling, there is another type of transmissibility upscaling which is called line source upscaling. In line source upscaling, a source line and a sink line are imposed at the centers of the two coarse cell respectively (**Figure 11**). Similar to plane source upscaling, we also need to solve the incompressible diffusivity equation for the flux flowing across the coarse cell interface.

The second type is global-local upscaling. This method is only applicable when an exact solution, or at least a good approximation, of the fine scale problem is available over most of the fine grid domain. One technique is to use the integrated fine flux over the face of the coarse cell and use this information to calibrate a local solution on the coarse cell.

The third type is global-global upscaling. This type of upscaling procedure minimizes a function measuring the difference between fine and coarse solutions which is computationally very expensive. The procedure is similar to history matching but here, a fine scale solution is used instead of physical measurements (Hales, H.B., 1983; Tan, T.B., 1995).

The last type is local-global upscaling. In the local-global upscaling, the global flow information is used to calibrate the local boundary conditions which are required in the calculation of upscaled properties. With the global flow problem solved, the local flow problems are then solved subject to boundary conditions determined from the global flows and the upscaled permeabilities or transmissibilities are then recomputed. This procedure is iterated until the system has converged to a self-consistent solution, where the global flow and the upscaled properties are consistent. For the first iteration, we can apply an existing standard upscaling approach, e.g., cell permeability upscaling.

As we mentioned above, in the local-global upscaling, we need to specify what global flow problem to be solved. There are a number of different ways to specify the global flow (Durlofsky 2005). Chen et al. (2003) used an approach that specifies large scale flows that are nominally in the coordinate directions respectively. These flows, which are also referred to as “generic global flows”, are obtained by fixing (different) constant pressures on two opposite boundaries and no-flow conditions on the other side boundaries. This kind of global specification provides local flows that have relatively strong components along the coordinate directions, which in turn allows for the accurate calculation of upscaled quantities.

Now we will have a brief introduction about the near-well upscaling. In all of the upscaling procedures considered above, we utilize a basic assumption that the flow is essentially linear within the upscaling region, which indicates that the large scale pressure gradient ∇p is approximately constant over the region of interest. However, this assumption is no longer applicable in the vicinity of well because the pressure solution has a logarithmic behavior around the well.

Let J_i be the well index which represents the physical well in grid block i. This well index provides a relation between the wellbore flow rate q_i^w in block i and the grid block average pressue p_i and the bottomhole pressure p_i^w:

$$q_i^w = J_i(p_i - p_i^w) \ldots\ldots\ldots\ldots\ldots\ldots\ldots\ldots\ldots\ldots\ldots\ldots\ldots\ldots (1.10)$$

For a fully penetrating vertical well in block i, the well index J_i is given by the well-known Peaceman equation:

$$J_i = \left(\frac{2\pi\sqrt{k_x k_y}\Delta z}{\log\frac{r_w}{r_o}} \right) \ldots\ldots\ldots\ldots\ldots\ldots\ldots\ldots\ldots\ldots\ldots\ldots\ldots\ldots (1.11)$$

where

$$r_o = 0.28 \frac{\sqrt{\sqrt{\frac{k_y}{k_x}}\Delta x^2 + \sqrt{\frac{k_x}{k_y}}\Delta y^2}}{\sqrt[4]{\frac{k_y}{k_x}} + \sqrt[4]{\frac{k_x}{k_y}}} \dots\dots\dots\dots\dots\dots\dots\dots\dots\dots\dots\dots\dots\dots\dots\dots\dots\dots\dots\dots\dots (1.12)$$

In **Eq. (1.11)**, we ignore the off-diagonal term in the permeability tensor and the skin factor. For the horizontal or deviated wells, we can derive similar equations as **Eq. (1.11)** and **Eq. (1.12)**.

If we do not introduce any special treatment in the region around well, the well index in the coarse grid block will be calculated with the application of the upscaled permeability. This approach is acceptable provided that the reservoir is not very heterogeneous or the permeability has a high correlation length in the plane perpendicular to the well trajectory in the near-well region. However, this simple treatment can lead to considerable error if the reservoir has high heterogeneity and in this case, it is necessary to improve the well index upscaling algorithm so that the characteristic flow behavior is captured around the well. Durlofsky (2000) describes an approach for the scaleup in the near-well region which can be considered as an extended local technique.

The local problem is defined on the domain as shown in **Figure 12**. The coarse well block at the center is surrounded by eight neighboring coarse cells.

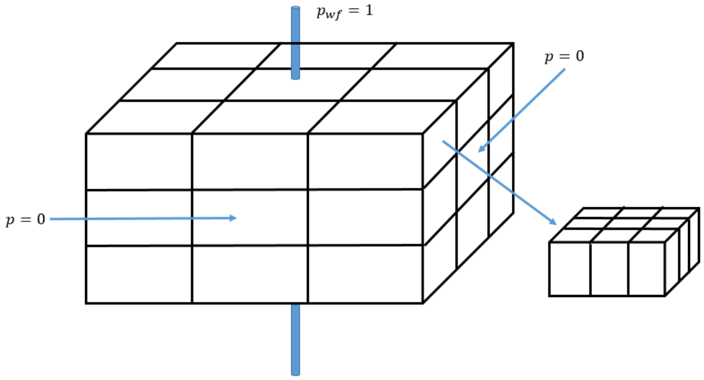

Figure 12: Near well scale up (Durlofsky et al. 2000)

Again, we solve the fine scale steady state pressure equation with a well source term q^w located at the central block:

$$\nabla \cdot (\mathbf{k} \cdot \nabla p) = q^w \ldots\ldots\ldots\ldots\ldots\ldots\ldots\ldots\ldots\ldots\ldots\ldots\ldots\ldots\ldots\ldots\ldots\ldots\ldots\ldots\ldots\ldots\ldots\ldots\ldots\ldots\ldots\ldots (1.13)$$

Eq. (1.10) is used for the flux term q_i^w as we numerically discretize **Eq. (1.13)**. The boundary condition is that the bottomhole pressure is taken as $p_i^w = 1$ and the pressure on the outer boundary is specified as $p = 0$. With the pressure solution of **Eq. (1.13)**, we calculate the velocity across each fine cell face in order to get the total flux across each coarse cell face. Also, we calculate the averaged pressure of each coarse cell by taking pore volume weighted average of the fine cell pressure in a coarse cell. Let $q_1 - q_4$ represent the flow rate through each of the four interfaces linking the well block to adjacent blocks and $< p >_i$ be the averaged pressure in the well block and each of its four neighbors. Then we can calculate the coarse grid well index J_i^* and the transmissibilities T_w^* that link the well block to adjacent blocks:

$$J_i^* = \frac{q^w}{< p >_i - p_i^w} \dots\dots\dots\dots\dots\dots\dots\dots\dots\dots\dots\dots\dots\dots (1.14)$$

and

$$(T_w^*)_{i+1/2} = \frac{q_1}{< p >_i - < p >_{i+1}} \dots\dots\dots\dots\dots\dots\dots\dots\dots\dots . (1.15)$$

where

$$q^w = q_1 + q_2 + q_3 + q_4 \dots\dots\dots\dots\dots\dots\dots\dots\dots\dots\dots\dots\dots . (1.16)$$

In two dimension, we computed four transmissibilities T_w^* and each connects the central well block to an adjacent block. The use of these parameters in many cases provides significantly improved coarse scale representations of well performance.

1.1.3 Multiscale upscaling methods

Another important class of upscaling techniques are multiscale finite element and finite volume approaches, which are designed to incorporate fine-scale information in coarse-scale dynamic simulation. Typically, the computational cost of the pressure equation is generally much higher than those of the transport equations in non-compositional models. Therefore, most of multiscale upscaling methods only treat pressure equations specially, while the transport equations are solved on the fine grid with the application of pressure solution which is used to reconstruct the fine grid velocity field. Thus, these methods require both coarse grid and fine grid, and that fine-scale data should be retained during the upscaling.

Most of the current multiscale methods that have been applied in reservoir simulation are based on finite element method. Actually, in 1980s and early 1990s there has been some pioneering work which is aimed at generalizing the standard finite element method to solve the second-order elliptic problems with rough coefficients (Babuska et al, 1994). Subsequently, Hou & Wu (1997) introduced the multiscale finite element method that constructs the multiscale basis functions based on the local pressure solution. The basis function construction makes use of a small amount of fine-scale information from the neighboring elements and this technique is called “oversampling”, which is similar to the extended permeability upscaling. Efendiev (1999) applied the multiscale finite element method for a unit mobility ratio transport problem and generated a coarse scale model that did not require the global fine-scale solution of the saturation equation. Afterwards, the coarse-grid saturation equation was formed through a volume average of the fine-scale equations and included terms involving both the average component of the velocity field and subgrid effects. A simplified model for the subgrid effects was proposed in terms of the subgrid velocity fluctuations (Efendiev et al. 2000).

In the subsequent work, Chen & Hou (2003) proposed a mixed multiscale method which is designed to generate the global mass conservative velocity field and is therefore better suited for transport phenomena. Aarnes (2004) further consider a variant of the mixed multiscale finite element proposed by Chen & Hou so that it can handle the well effects and be applied to two phase flow problem.

Arbogast (2002) and Arbogast & Bryant (2002) developed variational multiscale finite element methods. They defined a two-scale mixed finite element space and a coarser scale operator is coupled to a subgrid scale operator localized in space to each coarse grid element. The discrete solution is the sum of the results from the coarse grid component and the subgrid component. They have shown numerical results with good accuracy for the highly heterogeneous reservoir. Peszynska et al. (2002) proposed another multiscale finite element technique which is called mortar upscaling method. This method can discretize a reservoir into a series of subdomains in which numerical grids can be constructed independently and possibly different physical models and discretization techniques can be applied in each block. Jenny et al. (2003) introduced a multiscale finite volume procedure which employs ideas from the previous flux-continuous techniques (Lee et al. 2002). Flux-continuous finite volume techniques retain the pressure and flux continuity between cells, and local solution is required to determine the finite volume stencil. Jenny et al. incorporated fine-scale information in these local solutions to provide coarse-scale transmissibilities that takes account of the effects of the underlying fine-scale permeability.

The study of multiscale finite element method is out of the scope of this work.

1.2 Upgridding

In this section, we have a brief review over upgridding that is applied prior to the upscaling with the purpose of understanding the errors introduced by upscaling, or identifying the optimal coarsening resolution for the simulation grid.

There are three important assumptions for upgridding and upscaling and each assumption made on the coarse gird can be correlated with some kind of errors. The first assumption is about the pressure equilibrium state in a coarse cell. This assumption can be invalid in some situations such as the merge of pay and non-pay cells in a coarse cell. This will bring in considerable errors in pressure equilibrium because of the loss of connectivity. The second error is introduced in multiphase flow where regions with high velocity variance will make it difficult to capture the local spread of the head velocity, while regions with minimal variance in local velocity preserve the fluid front in an upscaling calculation. This can be used as an error measure which calculates the variance in local velocity $(\frac{k}{\phi})$ (King et al., 2006). Hosseini & Kelkar (2010) and Du (2012) extended the error measures by including the variance of local slowness $(\frac{\phi}{k})$ and a combined error measure which captures the variance of both $(\frac{k}{\phi})$ and $(\frac{\phi}{k})$ in one estimate. The third error is related to the off diagonal terms in the effective permeability tensor. This leads to the result that flow velocity direction is not aligned with the pressure gradient and that the two-point flux approximation is inapplicable in the simulation.

In conclusion, connectivity, velocity variance, and off diagonal permeability elements may be used as a diagnostic tool in simulation grid design. With a priori upscaling error analysis, the heterogeneity of the fine scale model can be well preserved on the coarse scale.

1.3 Motivation and scope of this work

Recently, a novel diffuse source (DS) upscaling (Nunna et al. 2015) has been developed in order to generate the transport properties for coarse dynamic simulation models. This approach applies the pressure transient concept to the calculation of the effective transmissibility between reservoir simulation coarse cell pairs. Unlike the usual incompressible steady state (SS) upscaling algorithm, DS upscaling solves a local compressible flow problem with a total flux imposed at the coarse cell interface and a source or sink in each fine cell specified with a transient state diffuse source solution. This approach has the advantage of including the internal cross flows in the upscaling calculation and reducing the impact of boundary conditions as well as cells with low but non-zero permeability. This upscaling algorithm has been tested on an onshore US tight gas reservoir model where the adaptive gridding is used to capture the strong heterogeneity.

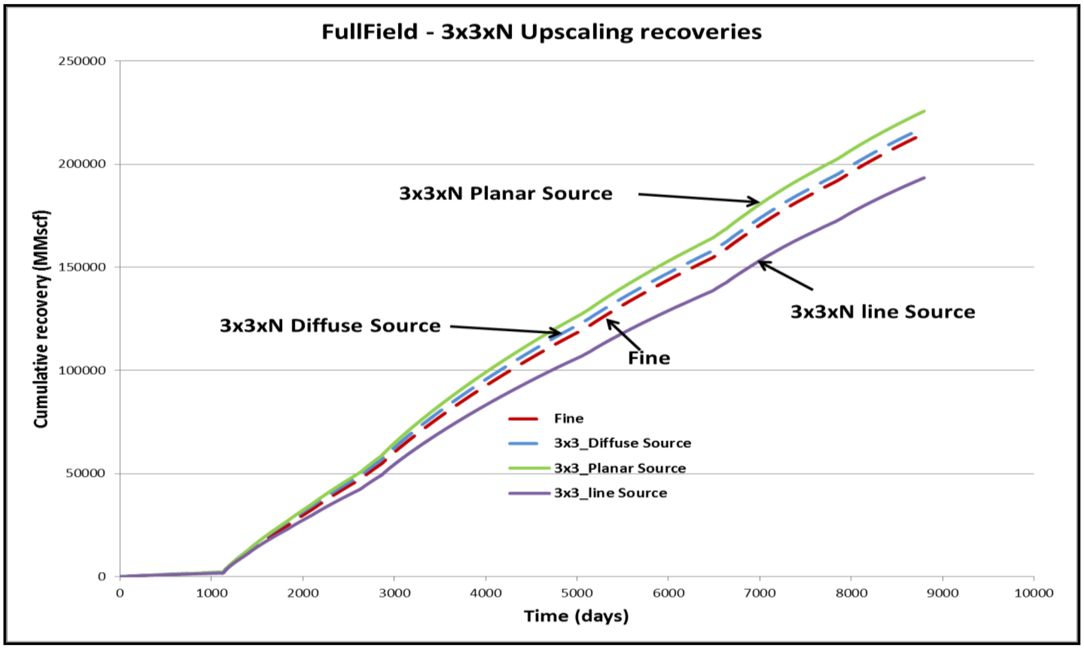

Figure 13: 3x3xN upscaling recoveries on tight gas model (Nunna 2014)

Figure 13 above illustrates 3x3xN upscaling recoveries from three different upscaling algorithms. The vertical axis represents the cumulative gas production, while the horizontal axis represents the production time. Red dash curve represents the result from fine scale simulation. Green solid curve and purple solid curve represent the results from the plane source upscaling and line source upscaling, respectively. These two transmissibility upscaling approach have been discussed in Section 1.1.2. We can see that the planar source boundary condition over-estimates the cumulative gas recovery and the line source provides an under-estimate result. Blue dash curve is the result from DS upscaling. The diffuse source upscaling provides the best estimate among these three algorithm.

However, there are some issues related to the DS upscaling algorithm. The first issue is the time which is required to define the transient state diffuse source in fine cell. In the previous work, the time selection rule is not clearly stated. Too small time value leads to an overestimated upscaling result, while too large time value makes the result underestimated. The second issue is related to the calculation of the effective transmissibility. The previous proposed method for the effective transmissibility calculation fails to reproduce the correct answer even for a homogeneous model, and the reason is that the pressure solution of the local DS upscaling problem is not a steady state pressure profile. Therefore, we need a new method to determine the effective transmissibility using the diffuse source pressure solution. The third issue of the DS upscaling algorithm has to do with the no flow boundary condition. No flow boundary conditions are considered to be too strict if the upscaling region has good connectivity with the surrounding domain, which is the situation that occurs in the SPE10 model. To generalize our DS upscaling algorithm, we need to know how to determine the computational region in the DS upscaling calculation so that we can reduce the impact of boundary conditions on the local flow problem.

The objective of this work is to improve the DS upscaling.

CHAPTER II

DIFFUSE SOURCE UPSCALING THEORY

In this chapter, we start with the introduction of the diffusive time of flight (DTOF) and drainage volume concepts. This will be followed by a detailed description of the diffuse source (DS) upscaling algorithm which applies the DTOF and drainage volume concepts. Finally, we will have a discussion on the specification of time and upscaling buffer region which is required for DS upscaling.

2.1 Diffusive time of flight and drainage volume

In this section, I will give a derivation for the diffusive time of flight $\tau(\mathbf{x})$, which is different from the previous work that applies the asymptotic expansion for the pressure solution in Fourier transform domain (Vasco et al. 2000). It will be shown that the eikonal equation for the diffusive time of flight can be obtained automatically without any approximation. Based on the diffusive time of flight concept, we will introduce the drainage volume concept and the effective drainage cross section.

2.1.1 The derivation of the diffusive time of flight

Let us start from 3D diffusivity equation that is used to describe the heterogeneous reservoir pressure for a fixed rate draw-down.

$$\phi(\mathbf{x})\mu c_t \frac{\partial p(\mathbf{x},t)}{\partial t} = \nabla \cdot \left(\vec{\vec{k}}(\mathbf{x}) \cdot \nabla p(\mathbf{x},t)\right) \dots\dots\dots\dots\dots\dots\dots\dots\dots\dots\dots\dots\dots\dots\dots\dots\dots\dots\dots\dots (2.1)$$

The boundary condition and initial condition are

$$q(|\mathbf{x}|=0,t)=q_w;\, p(|\mathbf{x}|\to\infty,t)=p_{init} \quad \ldots\ldots\ldots\ldots\ldots\ldots\ldots\ldots\ldots\ldots\ldots\ldots\ldots\ldots\ldots\ldots \quad (2.2.1)$$

$$p(\mathbf{x},t=0)=p_{init} \quad \ldots\ldots\ldots\ldots\ldots\ldots\ldots\ldots\ldots\ldots\ldots\ldots\ldots\ldots\ldots\ldots\ldots\ldots\ldots\ldots\ldots\ldots\ldots\ldots\ldots\ldots \quad (2.2.2)$$

Here we use the line source approximation for the inner boundary condition at $\mathbf{x}=0$ and the flow rate at the well is equal to q_w; the outer boundary condition is the pressure boundary condition which is equal to the initial reservoir pressure p_{init}. In **Eq. (2.1)**, $p(\mathbf{x},t)$ represents the reservoir pressure as a function of space coordinate **x** and time *t*; $\phi(\mathbf{x})$, μ and c_t represent porosity, fluid viscosity and total compressibility, respectively; $\vec{\vec{k}}(\mathbf{x})$ represents permeability tensor which can be expressed in the matrix form as follows:

$$\vec{\vec{k}}(\mathbf{x})=\begin{bmatrix} k_{11}(\mathbf{x}) & k_{12}(\mathbf{x}) & k_{13}(\mathbf{x}) \\ k_{21}(\mathbf{x}) & k_{22}(\mathbf{x}) & k_{23}(\mathbf{x}) \\ k_{31}(\mathbf{x}) & k_{32}(\mathbf{x}) & k_{33}(\mathbf{x}) \end{bmatrix} \quad \ldots\ldots\ldots\ldots\ldots\ldots\ldots\ldots\ldots\ldots\ldots\ldots\ldots\ldots\ldots\ldots\ldots\ldots\ldots. \quad (2.3)$$

where $k_{ij}(\mathbf{x})=k_{ji}(\mathbf{x})$ and $i,j=1,2,3$.

Now we apply Laplace transform to the function $p(\mathbf{x},t)$

$$\bar{p}(\mathbf{x},s)=\int_0^\infty p(\mathbf{x},t)e^{-st}dt \quad \ldots\ldots\ldots\ldots\ldots\ldots\ldots\ldots\ldots\ldots\ldots\ldots\ldots\ldots\ldots\ldots\ldots\ldots\ldots\ldots\ldots\ldots. \quad (2.4)$$

where $\bar{p}(\mathbf{x},s)$ represents the pressure in the Laplace domain. The transform of **Eq. (2.1)** yields the diffusivity equation in the Laplace domain

$$\phi(\mathbf{x})\mu c_t[s\bar{p}(\mathbf{x},s) - p_{init}] = \sum_{i,j=1}^{3} \partial_i \left(k_{ij}\, \partial_j \bar{p}(\mathbf{x},s)\right) \ldots\ldots\ldots\ldots\ldots\ldots\ldots\ldots\ldots\ldots\ldots\ldots\ldots\ldots\ldots. (2.5)$$

Now we write $\bar{p}(\mathbf{x},s)$ in another form as follows:

$$\bar{p}(\mathbf{x},s) = \frac{p_{init}}{s} + f(\mathbf{x},s)e^{-\sqrt{s}\tau(\mathbf{x})} \ldots\ldots\ldots\ldots\ldots\ldots\ldots\ldots\ldots\ldots\ldots\ldots\ldots\ldots\ldots\ldots\ldots\ldots\ldots\ldots\ldots\ldots\ldots\ldots. (2.6)$$

where $f(\mathbf{x},s)$ and $\tau(\mathbf{x})$ are interpreted as the amplitude and the phase of $\bar{p}(\mathbf{x},s)$, respectively. $\frac{p_{init}}{s}$ is the term that comes from the nonzero initial reservoir pressure p_{init}. This point can be illustrated from the inverse Laplace transform of the function $\frac{p_{init}}{s}$ which is equal to p_{init}. Next we will show how to get the eikonal equation for $\tau(\mathbf{x})$. The substitution of **Eq. (2.6)** into **Eq. (2.5)** yields the following equation

$$s\phi(\mathbf{x})\mu c_t f(\mathbf{x},s)e^{-\sqrt{s}\tau(\mathbf{x})} = I_1 + I_2 + I_3 \ldots\ldots\ldots\ldots\ldots\ldots\ldots\ldots\ldots\ldots\ldots\ldots\ldots\ldots\ldots\ldots\ldots\ldots\ldots\ldots. (2.7)$$

where I_1, I_2 and I_3 are given by the three equations below

$$I_1 = s\left[\nabla\tau(\mathbf{x}) \cdot \vec{\vec{k}}(\mathbf{x}) \cdot \nabla\tau(\mathbf{x})\right] f(\mathbf{x},s)e^{-\sqrt{s}\tau(\mathbf{x})} \ldots\ldots\ldots\ldots\ldots\ldots\ldots\ldots\ldots\ldots\ldots\ldots\ldots\ldots\ldots\ldots. (2.8.1)$$

$$I_2 = -\sqrt{s}\left[\nabla \cdot \left(\vec{\vec{k}}(\mathbf{x}) \cdot \nabla\tau(\mathbf{x})\right) f(\mathbf{x},s) + 2\nabla\tau(\mathbf{x}) \cdot \vec{\vec{k}}(\mathbf{x}) \cdot \nabla f(\mathbf{x},s)\right] e^{-\sqrt{s}\tau(\mathbf{x})} \ldots\ldots\ldots.. (2.8.2)$$

$$I_3 = \nabla \cdot \left(\vec{\vec{k}}(\mathbf{x}) \cdot \nabla f(\mathbf{x},s)\right) e^{-\sqrt{s}\tau(\mathbf{x})} \ldots\ldots\ldots\ldots\ldots\ldots\ldots\ldots\ldots\ldots\ldots\ldots\ldots\ldots\ldots\ldots\ldots\ldots\ldots\ldots. (2.8.3)$$

Equating powers of s, we let the left term of **Eq. (2.7)** be equal to the first term I_1 on the right hand side and thus, we can get the following equation:

$$\nabla\tau(\mathbf{x}) \cdot \vec{\vec{k}}(\mathbf{x}) \cdot \nabla\tau(\mathbf{x}) = \phi(\mathbf{x})\mu c_t \ldots\ldots\ldots\ldots\ldots\ldots\ldots\ldots\ldots\ldots\ldots\ldots\ldots\ldots\ldots\ldots\ldots\ldots\ldots\ldots\ldots\ldots\ldots (2.9)$$

Eq. (2.9) is the famous eikonal equation. To illustrate the physical meaning of the diffusive time of flight, we consider a 2D homogeneous isotropic reservoir. In this case, we can directly find the analytical solution for $\tau(\mathbf{x})$:

$$\tau(\mathbf{x}) = \sqrt{\frac{\phi\mu c_t}{k}}\, r \ldots\ldots\ldots\ldots\ldots\ldots\ldots\ldots\ldots\ldots\ldots\ldots\ldots\ldots\ldots\ldots\ldots\ldots\ldots\ldots\ldots\ldots\ldots\ldots\ldots\ldots\ldots. (2.10)$$

where the well is located at the origin and r represents the distance from the point **x** to the well. If we relate **Eq. (2.10)** with the radius of investigation concept (Lee, 1982), we can see that **Eq. (2.10)** can be used to characterize the slowness of the pressure wave front from an impulse source in the homogenous isotropic reservoir. In heterogeneous reservoir, similarly we claim that we can still use $\tau(\mathbf{x})$ to describe the pressure wave front propagation, but the solution of $\tau(\mathbf{x})$ is complicated and does not have the simple geometry as in the homogeneous isotropic case.

After getting the eikonal equation for the phase term in $\bar{p}(\mathbf{x}, s)$, we still need another equation for the amplitude term $f(\mathbf{x}, s)$. The second equation can be derived from **Eq. (2.7)** and **Eq. (2.9)** and the result is as follows:

$$\nabla\cdot\left(\vec{\vec{k}}(\mathbf{x})\cdot\nabla f(\mathbf{x},s)\right)=\sqrt{s}\left[\nabla\cdot\left(f(\mathbf{x},s)\vec{\vec{k}}(\mathbf{x})\cdot\nabla\tau(\mathbf{x})\right)+\nabla\tau(\mathbf{x})\cdot\vec{\vec{k}}(\mathbf{x})\cdot\nabla f(\mathbf{x},s)\right]\ldots.(2.11)$$

Therefore, from this derivation, we can see that we split the objective equation **Eq. (2.5)** into two equations **Eq. (2.9)** and **Eq. (2.11)**. **Eq. (2.9)** describes the pressure phase, while **Eq. (2.11)** provides the information related to the pressure amplitude. We first solve the eikonal equation **Eq. (2.9)**, and then we solve **Eq. (2.11)** using the solution of **Eq. (2.9)**. If we assume that $f(\mathbf{x},s)$ is a function depending on $\tau(\mathbf{x})$ only, then we can reduce **Eq. (2.11)** to be a one dimensional equation:

$$\frac{\partial}{\partial\tau}\left(w(\tau)\frac{\partial f}{\partial\tau}\right)=\sqrt{s}\left[\frac{\partial}{\partial\tau}(w(\tau)f)+w(\tau)\frac{\partial f}{\partial\tau}\right]\ldots\ldots\ldots\ldots\ldots\ldots\ldots\ldots\ldots\ldots\ldots\ldots\ldots\ldots\ldots\ldots.(2.12)$$

where $w(\tau)$ is the total cross section area of the τ contour surface. The derivation for **Eq. (2.12)** is in Appendix A.

Once we find the solution for $f(\mathbf{x},s)$ and $\tau(\mathbf{x})$, then we can use the convolution theorem to get the pressure solution in the physical time domain. However, since the main purpose of this section is to show where the diffusive time of flight comes from and its governing equation, it is out of the scope to discuss the methodology about how to solve the pressure amplitude equation **Eq. (2.12)**, which is very complicated and still needs further investigation. Instead, next we will focus on some simple approximate equations which are used in the diffuse source upscaling.

2.1.2 $\mathbf{w(\tau)}$ formulation and drainage volume

We have introduced the diffusive time of flight and the eikonal equation of $\tau(\mathbf{x})$. Given the initial starting point, we can solve this eikonal equation by using a class of front tracking methods called Fast Marching Method (FMM) (Sethian, 1999). Fast Marching Method can be viewed as a continuous version of Dijkstra's algorithm (1959) which is an algorithm that can find the shortest path between two given nodes. In this work, we can use Dijkstra's algorithm to find the path of minimum diffusive time of flight between the starting source point and the center of a fine cell. The center finite difference (FD) scheme can be applied to calculate the total $\delta\tau$ for flow between two adjacent cells using the length from cell center to cell face, and the porosity and permeability of each of the two cells. Using the notations from **Figure 14**, we can write the equation for $\delta\tau$ as follows:

$$\delta\tau = \sqrt{\mu c_t}\left(\frac{L_1}{2}\sqrt{\frac{\phi_1}{k_1}} + \frac{L_2}{2}\sqrt{\frac{\phi_2}{k_2}}\right) \quad (2.13)$$

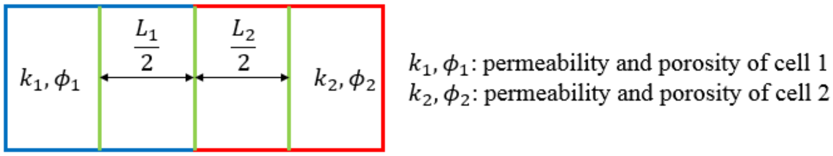

Figure 14: $\delta\tau$ between two adjacent cells

After solving the eikonal equation, we can calculate the total pore volume enclosed by a τ-contour surface $V_p(\tau)$ and $w(\tau)$ is the derivation of $V_p(\tau)$ with respect to τ:

$$w(\tau) = \frac{dV_p(\tau)}{d\tau} \dots\dots\dots\dots\dots\dots\dots\dots\dots\dots\dots\dots\dots\dots\dots\dots\dots\dots\dots\dots\dots\dots\dots\dots\dots\dots\dots\dots\dots\dots. (2.14)$$

Assuming that the pressure depends only on $\tau(\mathbf{x})$ and t, Zhang et al. (2014) and Fujita et al. (2015) derived an equivalent 1D diffusivity equation by using the coordinate transformation technique which maps the three dimensional solutions as a function of (x, y, z) into a single spatial coordinate τ. The resulting 1D diffusivity equation for pressure is given by the following equation:

$$\frac{\partial p(\tau,t)}{\partial t} - \frac{1}{w(\tau)}\frac{\partial}{\partial \tau}\left(w(\tau)\frac{\partial p(\tau,t)}{\partial \tau}\right) = 0 \text{ a.e.} \dots\dots\dots\dots\dots\dots\dots\dots\dots\dots\dots\dots\dots\dots\dots\dots (2.15)$$

For comparison, the diffusivity equation for 2D infinite acting radial flow is:

$$\frac{\partial p(r,t)}{\partial t} - \frac{1}{2\pi rh}\frac{\partial}{\partial r}\left(2\pi rh\frac{\partial p(r,t)}{\partial r}\right) = 0 \text{ a.e.} \dots\dots\dots\dots\dots\dots\dots\dots\dots\dots\dots\dots\dots\dots\dots\dots (2.16)$$

This comparison between $w(\tau)$ and $2\pi rh$ implies that we can interpret $w(\tau)$ to be proportional to the effective drainage cross section of a τ-contour.

Alternatively, we can also write the diffusivity equation using a mixed form of the pressure and the flux. Let $q(\tau, t)$ be the total flux flowing across a τ-contour surface and $q(\tau, t)$ is given by the following equation:

$$q(\tau, t) = c_t w(\tau) \frac{\partial p(\tau, t)}{\partial \tau} \quad \dots\dots\dots\dots\dots\dots\dots\dots\dots\dots\dots\dots\dots\dots\dots\dots\dots\dots\dots\dots\dots\dots\dots\dots \quad (2.17)$$

Therefore, for a fixed rate draw-down in an infinite domain, using **Eq. (2.17)** we can write **Eq. (2.15)** as:

$$c_t \frac{\partial p(\tau, t)}{\partial t} = \frac{1}{w(\tau)} \frac{\partial q(\tau, t)}{\partial \tau} \approx \frac{q_w}{V_p(t)} e^{-\frac{\tau^2}{4t}} \quad \dots\dots\dots\dots\dots\dots\dots\dots\dots\dots\dots\dots\dots\dots\dots\dots\dots\dots \quad (2.18)$$

In **Eq. (2.18)**, q_w is the flux right at the well or the fluid flow surface. In general, **Eq. (2.18)** is only an approximate solution, but it serves as our starting point in DS upscaling. This approximation is exact if the porous medium is homogeneous isotropic. $V_p(t)$ in **Eq. (2.18)** is the drainage volume that depends on the time if the pressure solution is in the pressure transient state. The discrete form of $V_p(t)$ is given by the equation below:

$$V_p(t) = \int_0^\infty dV_p(\tau) \cdot e^{-\frac{\tau^2}{4t}} \approx \sum_{\text{Cell},j} PV_j \cdot e^{-\frac{\tau_j^2}{4t}} \quad \dots\dots\dots\dots\dots\dots\dots\dots\dots\dots\dots\dots\dots\dots\dots\dots\dots\dots. \quad (2.19)$$

In **Eq. (2.19)** we see that there is an exponential weight factor that distinguishes the different contribution of different fine cells to the total drainage volume $V_p(t)$. Based on **Eq. (2.18)** and **Eq. (2.19)**, here we have the following comments:

At a fixed time, the exponential term will reduce to zero at a location with sufficiently large diffusive time of flight τ, which implies in the far region the pressure and the flux will stay in the initial condition.

As $\tau^2/4t \sim O(1)$, the exponential term varies from 1 to 0, and we have a moving interface transient solution.

At a fixed time t, the exponential term is approximately unity in the region where the condition $\tau^2 \ll 4t$ is satisfied. In that case, $\frac{\partial p}{\partial t}$ will be independent of location and therefore, the pressure profile is in a pseudo-steady state (PSS) in the region where τ^2 is much less than $4t$. Therefore, as the time increases from zero, the first locations where the pressure profile is in the PSS should be in the vicinity around a source or sink.

2.2 SPE10 model description

In this section, for the convenience of the latter discussion on the diffuse source upscaling algorithm, I will give a brief introduction about the SPE10 geological model. The geological information of the SPE10 model will be used later as we focus on the improvement of the diffuse source upscaling algorithm.

The SPE10 model has been designed to be a challenge for upscaling algorithms. It is a 60x220x85 cell model (1,122,000 cells in total) and all the cells have regular rectangular shape with the same size 20 ft x 10 ft x 2 ft. The top 35 layers represent the Tarbert formation (sheet sand) and the bottom 50 layers represent Upper Ness (tortuous narrow channels). **Figure 15**(a) shows us the permeability distribution of a representative layer from the top zone and **Figure 15**(b) shows us the permeability distribution of a representative layer from the bottom zone.

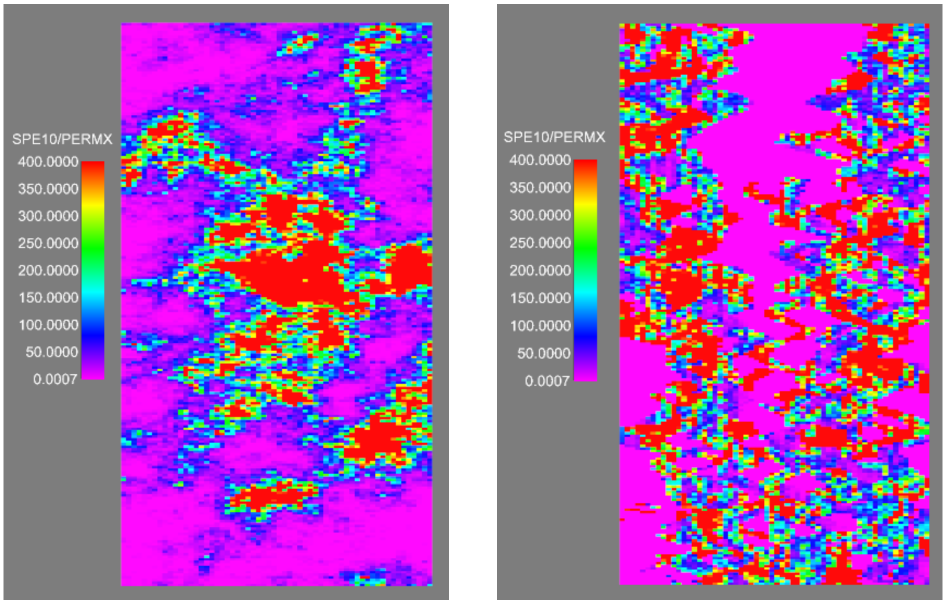

(a) (b)

Figure 15: PERMX in different layers of SPE10 model. (a) layer from the upper zone. (b) layer from the lower zone.

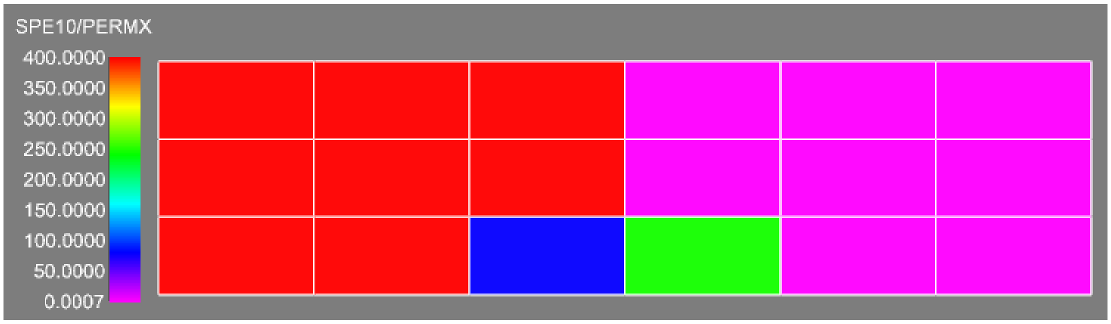

Figure 16: Example of the local high contrast coarse cell

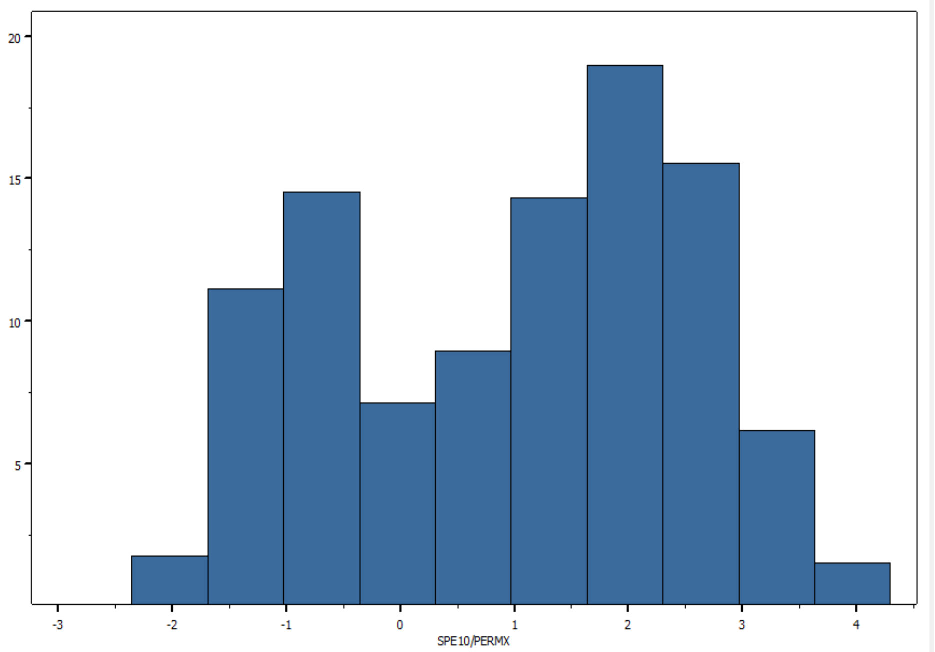

Figure 17: The histogram of $\log k_x$

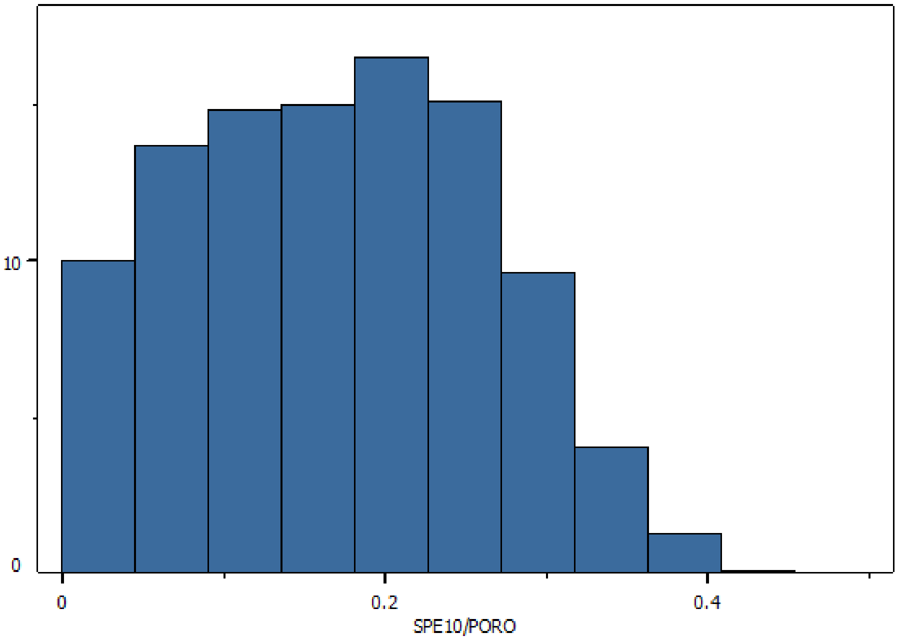

Figure 18: The histogram of reservoir porosity

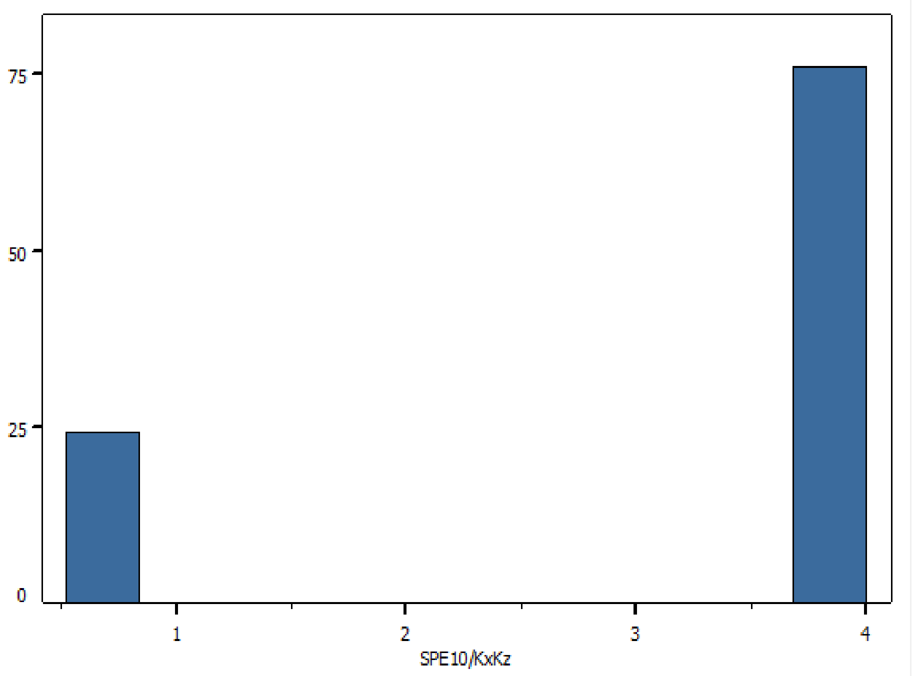

Figure 19: The histogram of $\log k_x/k_z$

Because of the tortuous narrow channels in the bottom zone, we need to deal with many high contrast coarse cells, especially in the region near the channel barrier. **Figure 16** above is an example of a small region with high contrast permeability. The upscaling of this region is really challenging.

In addition, **Figure 17** is the histogram of $\log k_x$ which satisfies the bimodal distribution. The permeability in x direction varies approximately from 0.01 md to 10000 md. **Figure 18** is the histogram of porosity in SPE10 model which approximately satisfies the normal distribution. The maximum porosity is about 0.5 and the minimum porosity is 0. **Figure**

19 is the histogram of $\log(k_x/k_z)$ and it has only two values. The big value accounts for 75 percent and the small value accounts for 25 percent.

In conclusion, the reservoir properties are extremely heterogeneous with strong contrast between the porosity and permeability trends, **Figure 20**.

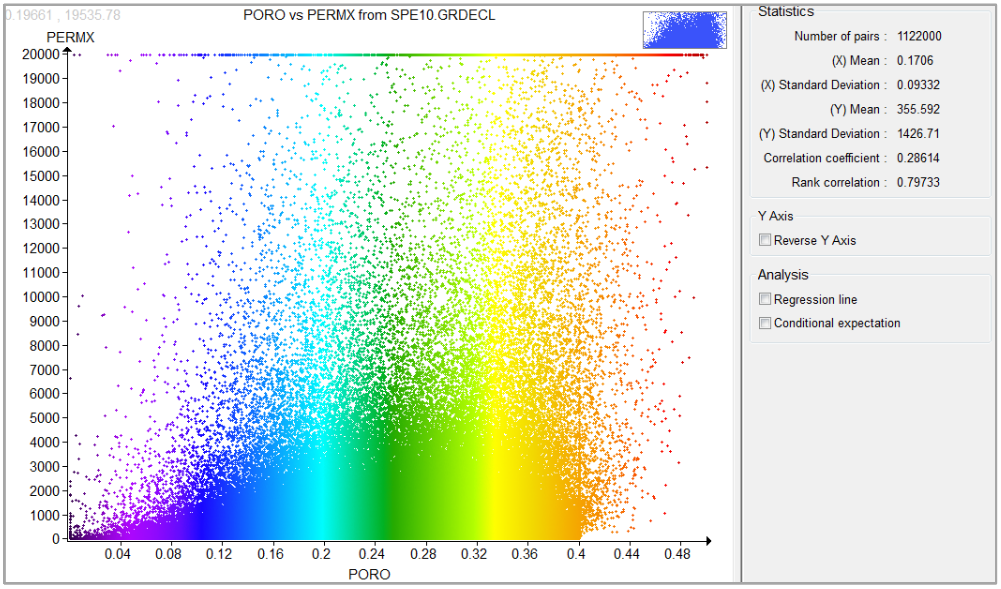

Statistics

Number of pairs : 1122000
(X) Mean : 0.1706
(X) Standard Deviation : 0.09332
(Y) Mean : 355.592
(Y) Standard Deviation : 1426.71
Correlation coefficient : 0.28614
Rank correlation : 0.79733

☐ Reverse Y Axis
☐ Regression line
☐ Conditional expectation

Figure 20: Permeability-porosity cross-plot for the SPE10 test model (Nunna et al. 2015)

2.3 Diffuse source upscaling algorithm

In this section, I will first describe the diffuse source upscaling algorithm in detail. Then I will discuss three issues that need to be resolved for the diffuse source upscaling. Specifically, the first one is related to the pressure averaging. Diffuse source upscaling algorithm is a non-steady state upscaling algorithm and the pressure in the local upscaling region follows a quadratic trend. We cannot use a linear pore volume weighted average method to calculate the average pressure in a coarse cell. We will discuss this problem further with a simple homogeneous example at a long time limit.

In addition, the second issue is about the specification of the time parameter in the definition of diffuse source. Further investigation is needed on the specification of the time parameter in the definition of diffuse source so that the algorithm can be applied to other systems. Along with the second issue, we will also have a detailed discussion on the specification of the local computational region. We will consider the effect to extend the computational region beyond the local coarse cell.

Each of these problems will be covered in the following subsections where most of the content is drawn from the paper (Nunna et al. 2015) published in SPE Reservoir Simulation Symposium (RSS) in 2015.

2.3.1 Algorithm

In this section, we will describe the diffuse source upscaling algorithm. As is shown in **Figure 21**, we consider a local numerical flow problem, but unlike the plane source upscaling discussed in Section 1.1.2, here we assume that the sources or sinks are located within the fine cells.

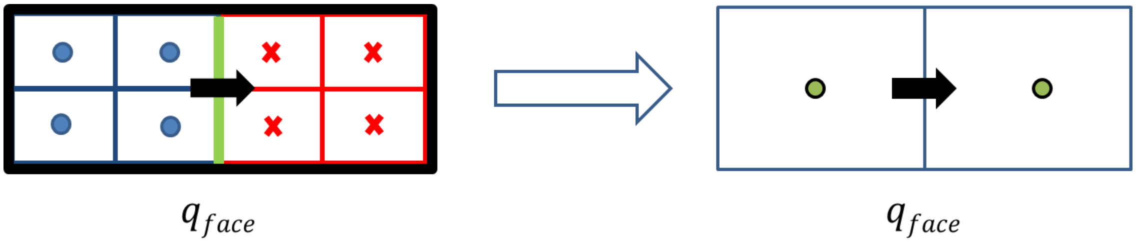

Figure 21: 2x2 diffuse source upscaling (Nunna et al. 2015)

Specifically, we impose a total flux at the coarse cell face and calculate the pressure drop between two coarse cells. The compressible flow equations and the approximate solution to the diffusivity equation are used to define sources and sinks in each of the fine cells, consistent with the total imposed flux.

$$\nabla.\vec{u} = -\phi c_t \frac{\partial p}{\partial t} \approx \pm \frac{q_{face}}{V_p(t)} \phi e^{-\frac{\tau^2}{4t}} \sim \pm q_{face}\phi_{eff} \dots\dots\dots\dots\dots\dots\dots\dots\dots\dots\dots\dots\dots\dots\dots (2.20)$$

where

$$\phi_{eff} = \phi e^{-\tau^2/4t} \dots\dots\dots\dots\dots\dots\dots\dots\dots\dots\dots\dots\dots\dots\dots\dots\dots\dots\dots\dots\dots\dots\dots\dots\dots\dots\dots. (2.21)$$

As we see from **Eq. (2.20)**, the strength of the local source and sink terms are proportional to the effective porosity ϕ_{eff}. The variable τ represents DTOF value at the center of each fine cell, and it is calculated by solving the DTOF eikonal equation with the coarse cell interface treated as the starting face ($\tau = 0$). At present we are using Dijkstra’s algorithm (Nunna 2014) to solve this eikonal equation. The boundary conditions on this local problem must be specified in order for the coarse scale equivalent permeability or transmissibility to be computed. The simplest choice is to use no flow boundary conditions around the coarse cell external faces, which makes the local flow problem completely decoupled from the domain around the upscaling region. We will first utilize this choice of boundary condition, but later we will show that it is too restrictive and underestimates the effective permeability. In addition, we will not actually solve the time dependent diffusivity equation, but will instead select a time at which we calculate the effective porosity and allocate the face flux to the fine cells as source or sink terms. If the time is chosen to be infinity, then the upscaling is so called pseudo steady state (PSS) diffuse source upscaling.

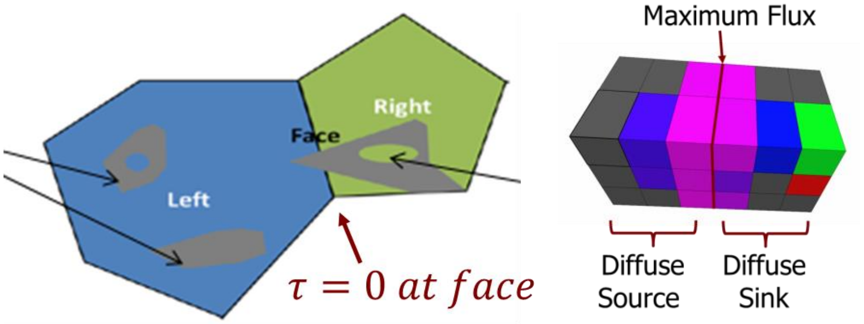

Figure 22: Diffuse source cell face drainage volume (Nunna et al. 2015)

The diffuse source upscaling algorithm has some important features that can be illustrated by **Figure 22**. In **Figure 22**, the left picture has two coarse cells where the grey part represents the impermeable cells. If we consider a pressure wave moving away from the coarse cell interface, only the cells with finite diffusive time of flight τ are connected with the coarse cell interface and the cells with infinite diffusive time of flight τ are disconnected from the coarse cell interface. Therefore, the disconnected cells will not have any contribution to the flux at the coarse cell interface. For the cells with finite τ, depending upon the time threshold chosen, we may reduce the impact of the cells with low permeability, making the results less sensitive to the choice of a net-pay cut-off. The right picture of **Figure 22** is a sample of 3x3x3 cells from the tight gas field. This is a low net to gross system which need not have horizontal flow connectivity across the entire coarse cell. The maximum flux is located at the coarse cell interface where the DTOF value is zero. The grey part is the disconnected cell with infinite τ, but the remaining cells have finite τ and contribute to the upscaling calculation. At early time only the cells right beside the face of maximum flux are in the drainage volume region. As time goes on, more and more cells with finite τ are included and finally, with the assumption that the outer boundary is no flow boundary condition, the flow enters pseudo steady state.

In addition, we have another figure which shows the variation of flux with time in a homogeneous cell (the left coarse cell in **Figure 23**).

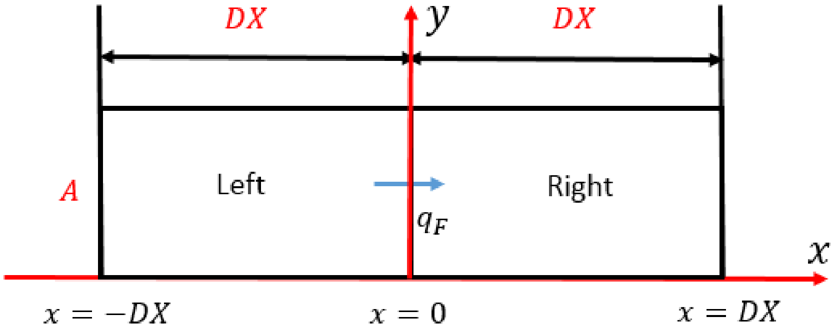

Figure 23: Two homogeneous cells

Let us focus on the left coarse cell. We assume that the flow starts from the right face due to a source or a sink on the right side of the left coarse cell. In diffuse source upscaling, this source or sink refers to the adjacent right coarse cell. The left side of the left coarse cell is sealed. For this simple example, at the early time the flux function can be expressed in terms of the complementary error function. In the late time when the pseudo steady state limit is reached, the flux function is a simple linear function. Specifically, the flux function is determined by the following equations:

At early time,

$$q(x,t) = q_F \mathrm{erfc}\left(\sqrt{\frac{\phi\mu c_t}{4kt}}|x|\right); -DX \le x \le 0 \ldots\ldots\ldots\ldots\ldots\ldots\ldots\ldots\ldots\ldots\ldots\ldots\ldots\ldots. (2.22)$$

where the complementary error function erfc(x) is defined as:

$$\mathrm{erfc}(x) = \frac{2}{\sqrt{\pi}}\int_{x}^{\infty} e^{-\xi^2} d\xi \ldots\ldots\ldots\ldots\ldots\ldots\ldots\ldots\ldots\ldots\ldots\ldots\ldots (2.23)$$

At late time,

$$q(x,t) = \frac{q_F}{DX}x + q_F;\ -DX \leq x \leq 0 \ldots\ldots\ldots\ldots\ldots\ldots\ldots\ldots\ldots\ldots\ldots\ldots (2.24)$$

Figure 24 below illustrates the flux function at the early time and late time determined by **Eq. (2.22)** and **(2.24)**. From **Figure 24**, we see that at early time the flux is zero except near the coarse cell face, and an upscaling calculation should be focused only on those cells near the face. For 3D heterogeneous flow problem, the flux function is more complicated and will need to be determined numerically.

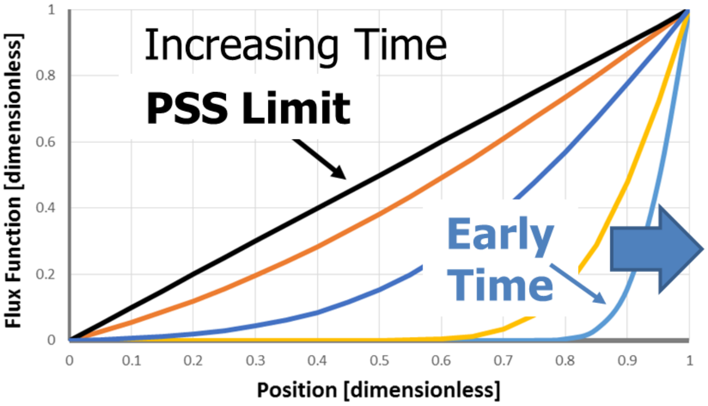

Figure 24: 1D homogeneous diffuse source flux functions (Nunna et al. 2015)

2.3.2 Pseudo steady state flow and steady state flow

In this section, I will show the pressure averaging problem which exists in the old diffuse source transmissibility upscaling algorithm using two adjacent homogeneous coarse cells. In diffuse source transmissibility upscaling, given that the flux across the coarse cell interface is known, we need to calculate the pressure difference between two coarse cells. If we use a linear pore volume weighted average to calculate the average pressure in a coarse cell and then calculate the pressure difference between two adjacent coarse cells, we will get the erroneous answer even in the transmissibility upscaling for homogeneous coarse cells. To show this point, we can take a look at the picture in **Figure 25** which shows the velocity profile of two homogeneous cells with a cross sectional area A, length DX of each cell and flux, q_F between the cells.

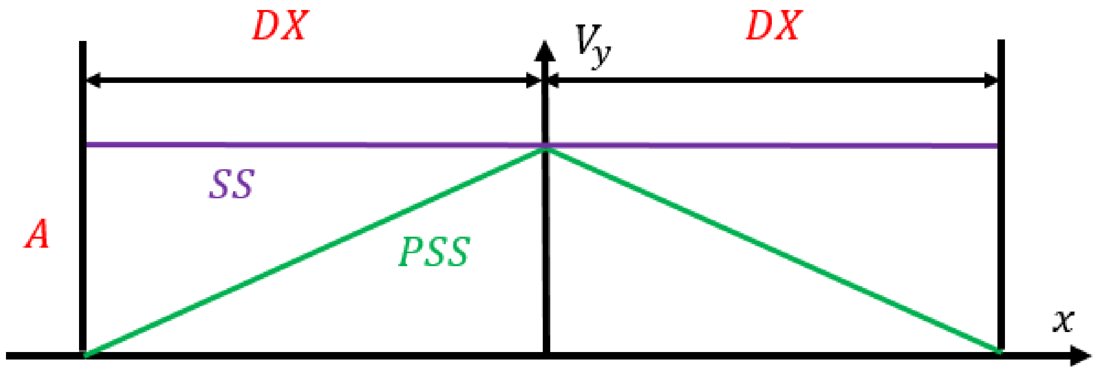

Figure 25: Velocity profile of steady state flow and pseudo steady state flow

The outer boundary condition is the no-flow boundary condition. We compare the velocity profile in pseudo steady state (PSS) with that in steady state (SS). For the PSS flow, the left coarse cell velocity gradient and the right coarse cell velocity gradient are given by **Eq. (2.25)** and **Eq. (2.26)**:

$$\frac{\partial \mathrm{u}_{\mathrm{l}}^{\mathrm{pss}}}{\partial \mathrm{x}} = \frac{\mathrm{q_F}}{\mathrm{A} \cdot \mathrm{DX}} \quad (2.25)$$

$$\frac{\partial \mathrm{u}_{\mathrm{r}}^{\mathrm{pss}}}{\partial \mathrm{x}} = -\frac{\mathrm{q_F}}{\mathrm{A} \cdot \mathrm{DX}} \quad (2.26)$$

In **Eq. (2.25) and (2.26)**, $\mathrm{u}_{\mathrm{l}}^{\mathrm{pss}}$ and $\mathrm{u}_{\mathrm{r}}^{\mathrm{pss}}$ represent the PSS velocity of the left coarse cell and the right coarse cell, respectively. Since the outer boundary condition is taken as the no-flow boundary condition, the velocity is zero at the edges $\mathrm{x} = -\mathrm{DX}$ and $\mathrm{x} = \mathrm{DX}$. Using these boundary conditions, we solve for the velocity in each cell which is given by the following two equations:

$$\mathrm{u}_{\mathrm{l}}^{\mathrm{pss}} = \frac{\mathrm{q_F}}{\mathrm{A}} \frac{\mathrm{DX} + \mathrm{x}}{\mathrm{DX}}; -\mathrm{DX} \le \mathrm{x} \le 0 \quad (2.27)$$

$$\mathrm{u}_{\mathrm{r}}^{\mathrm{pss}} = \frac{\mathrm{q_F}}{\mathrm{A}} \frac{\mathrm{DX} - \mathrm{x}}{\mathrm{DX}}; 0 \le \mathrm{x} \le \mathrm{DX} \quad (2.28)$$

In contrast, for the SS flow, the velocity is a constant value in the entire upscaling region and is given by the following equation:

$$u_l^{ss} = u_r^{ss} = \frac{q_F}{A} \dots \dots \dots \dots \dots \dots \dots \dots \dots \dots \dots \dots \dots \dots \dots \dots \dots \dots \dots \dots \dots \dots \dots \dots \dots \dots \dots \dots \dots \dots .. (2.29)$$

For the cell pressure profile, we use the 1D Darcy equation:

$$u = -\frac{k}{\mu}\frac{\partial p}{\partial x} \dots \dots \dots \dots \dots \dots \dots \dots \dots \dots \dots \dots \dots \dots \dots \dots \dots \dots \dots \dots \dots \dots \dots \dots \dots \dots \dots \dots \dots . (2.30)$$

where k is the cell permeability and μ is the fluid viscosity. Based on the velocity equation for the PSS flow and the SS flow, we can get the corresponding pressure in the upscaling region as follows:

$$p_l^{pss} = p_F - \frac{\mu q_F DX}{2kA}\left(\left(\frac{DX + x}{DX}\right)^2 - 1\right); -DX \leq x \leq 0 \dots \dots \dots \dots \dots \dots \dots \dots \dots \dots \dots \dots (2.31)$$

$$p_r^{pss} = p_F + \frac{\mu q_F DX}{2kA}\left(\left(\frac{DX - x}{DX}\right)^2 - 1\right); 0 \leq x \leq DX \dots \dots \dots \dots \dots \dots \dots \dots \dots \dots \dots \dots .. (2.32)$$

$$p_l^{ss} = p_F - \frac{\mu q_F}{kA}x; -DX \leq x \leq 0 \dots \dots \dots \dots \dots \dots \dots \dots \dots \dots \dots \dots \dots \dots \dots \dots \dots \dots \dots \dots . (2.33)$$

$$p_r^{ss} = p_F - \frac{\mu q_F}{kA}x; 0 \leq x \leq DX \dots \dots \dots \dots \dots \dots \dots \dots \dots \dots \dots \dots \dots \dots \dots \dots \dots \dots \dots \dots \dots (2.34)$$

where p_F in **Eq. (2.31 − 2.34)** represents the pressure at cell interface. The above equations show a quadratic relationship of pressure in terms of the x coordinate in the PSS flow, while the pressure varies linearly with the variable x in the SS flow. For the average cell pressure in the PSS flow, it is given by the following equations:

$$\bar{p}_l = \frac{1}{DX}\int_{-DX}^{0}\left\{p_F - \frac{\mu q_F DX}{2kA}\left(\left(\frac{DX + x}{DX}\right)^2 - 1\right)\right\}dx \ldots\ldots\ldots\ldots\ldots\ldots\ldots\ldots\ldots\ldots\ldots\ldots\ldots (2.35)$$

$$\bar{p}_r = \frac{1}{DX}\int_{0}^{DX}\left\{p_F + \frac{\mu q_F DX}{2kA}\left(\left(\frac{DX - x}{DX}\right)^2 - 1\right)\right\}dx \ldots\ldots\ldots\ldots\ldots\ldots\ldots\ldots\ldots\ldots\ldots\ldots\ldots . (2.36)$$

The result of the above two integrals is

$$\bar{p}_l = p_F + \frac{\mu q_F DX}{3kA} \ldots\ldots\ldots\ldots\ldots\ldots\ldots\ldots\ldots\ldots\ldots\ldots\ldots\ldots\ldots\ldots\ldots\ldots\ldots\ldots\ldots\ldots\ldots\ldots\ldots\ldots .. (2.37)$$

$$\bar{p}_r = p_F - \frac{\mu q_F DX}{3kA} \ldots\ldots\ldots\ldots\ldots\ldots\ldots\ldots\ldots\ldots\ldots\ldots\ldots\ldots\ldots\ldots\ldots\ldots\ldots\ldots\ldots\ldots\ldots\ldots\ldots\ldots .. (2.38)$$

With the average cell pressure, the old diffuse source transmissibility upscaling uses the following equation to determine the inter-cell transmissibility:

$$T = \frac{q_F}{\bar{p}_l - \bar{p}_r} \ldots\ldots\ldots\ldots\ldots\ldots\ldots\ldots\ldots\ldots\ldots\ldots\ldots\ldots\ldots\ldots\ldots\ldots\ldots\ldots\ldots\ldots\ldots\ldots\ldots\ldots\ldots\ldots\ldots . (2.39)$$

If we use **Eq. (2.39)** for the inter-cell transmissibility in PSS flow, we will obtain the following result:

$$T_{pss} = \frac{3}{2}\frac{kA}{\mu DX} \ldots\ldots\ldots\ldots\ldots\ldots\ldots\ldots\ldots\ldots\ldots\ldots\ldots\ldots\ldots\ldots\ldots\ldots\ldots\ldots\ldots\ldots\ldots\ldots\ldots\ldots\ldots\ldots\ldots (2.40)$$

However, we know the solution of transmissibility between two homogeneous cells which is given by the equation:

$$T_{SS} = \frac{kA}{\mu DX} \quad \text{(2.41)}$$

Therefore, we see that there is an extra pre-factor $\frac{3}{2}$ from the PSS solution. This result indicates that it is incorrect to use **Eq. (2.39)** to calculate the inter-cell transmissibility in diffuse source upscaling. This is the reason why we need to consider the pressure averaging problem in diffuse source upscaling.

2.3.3 Pressure averaging

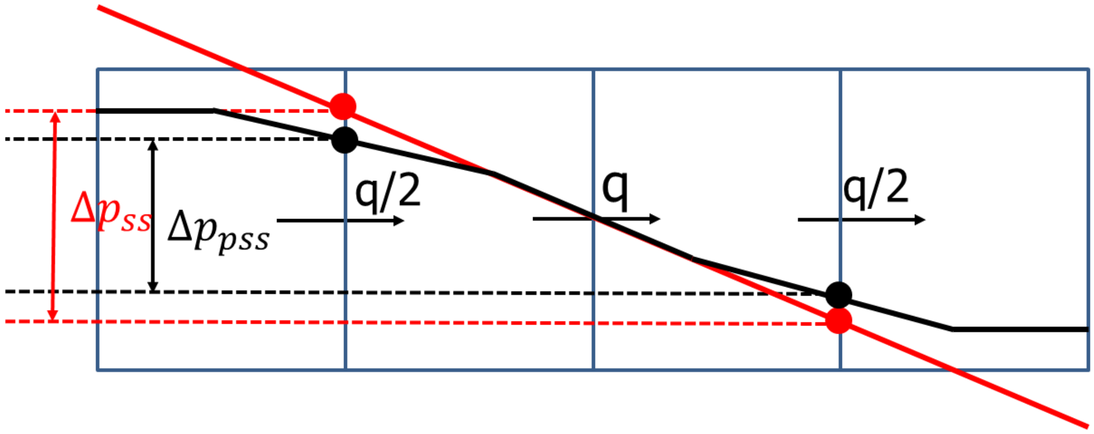

Figure 26: 1D Homogeneous discrete 4 cell pressure solution (Nunna et al. 2015)

In the last section, we have seen that the PSS pressure solution is a quadratic function and the SS pressure solution is a linear function. The discretized form of these two different pressure profiles is shown in **Figure 26** where four identical fine cells are aligned in a line. The black curve represents the pressure solution of DS upscaling where each cell has a source or sink strength of $q/2$ in the PSS limit. The red straight line is the pressure solution from steady state upscaling. Since the linear pore volume weighted average cell pressure will yield the overestimated inter-cell transmissibility for two adjacent homogeneous coarse cells, we need to find another method on how to use the pressure solution from the local DS upscaling to make sure that the DS upscaling algorithm can generate the correct inter-cell transmissibility for the simplest upscaling example-the upscaling of two adjacent homogeneous coarse cells. If we focus on the fine cells immediately adjacent to the coarse cell interface, we recognize that the two pressure profiles are identical. For a finite difference calculation, these half cells have locally reached a steady state limit. Hence we may use the fine cell pressures immediately adjacent to the coarse cell face to define an effective face permeability. Then the effective face permeability determined from the diffuse source calculation is applied to the calculation of steady state transmissibility in the simulator. Therefore, the equation for the effective steady state transmissibility is given as follows:

$$\mathrm{T_{eff}} = \frac{\mathrm{L_1}}{\mathrm{L_2}} \frac{\mathrm{q_{face}}}{< \mathrm{p} >_{\mathrm{L}} - < \mathrm{p} >_{\mathrm{R}}} \ldots\ldots\ldots\ldots\ldots\ldots\ldots\ldots\ldots\ldots\ldots\ldots\ldots\ldots\ldots\ldots\ldots\ldots\ldots\ldots\ldots\ldots\ldots\ldots\ldots\ldots \quad (2.42)$$

In **Eq. (2.42)**, $\mathrm{L_1}$ is the length of the line that connects the center of the two pressure averaging regions; $\mathrm{L_2}$ is the length of the line that connects the center of the two coarse cells. $< \mathrm{p} >_{\mathrm{L/R}}$ represents the effective pore volume weighted average pressure which makes use of the fine cells right beside the coarse cell interface. They are given by the following two equations:

$$<p>_L = \frac{\sum_{i=1}^{N_L} p_i \times PV_i \times e^{-\frac{\tau_i^2}{4t}}}{\sum_{i=1}^{N_L} PV_i \times e^{-\frac{\tau_i^2}{4t}}} \quad \ldots \ldots \ldots \ldots \ldots \ldots \ldots \ldots \ldots \ldots \ldots \ldots \ldots \ldots \ldots \ldots \ldots \ldots \ldots \ldots \ldots \ldots \ldots \ (2.43)$$

$$<p>_R = \frac{\sum_{i=1}^{N_R} p_i \times PV_i \times e^{-\frac{\tau_i^2}{4t}}}{\sum_{i=1}^{N_R} PV_i \times e^{-\frac{\tau_i^2}{4t}}} \quad \ldots \ldots \ldots \ldots \ldots \ldots \ldots \ldots \ldots \ldots \ldots \ldots \ldots \ldots \ldots \ldots \ldots \ldots \ldots \ldots \ldots \ldots \ldots \ (2.44)$$

In **Eq. (2.43)** and **(2.44)**, $N_{L/R}$ represents the number of fine cells right beside the two sides of the coarse cell interface. The DTOF τ is calculated with the starting point located at the coarse cell face.

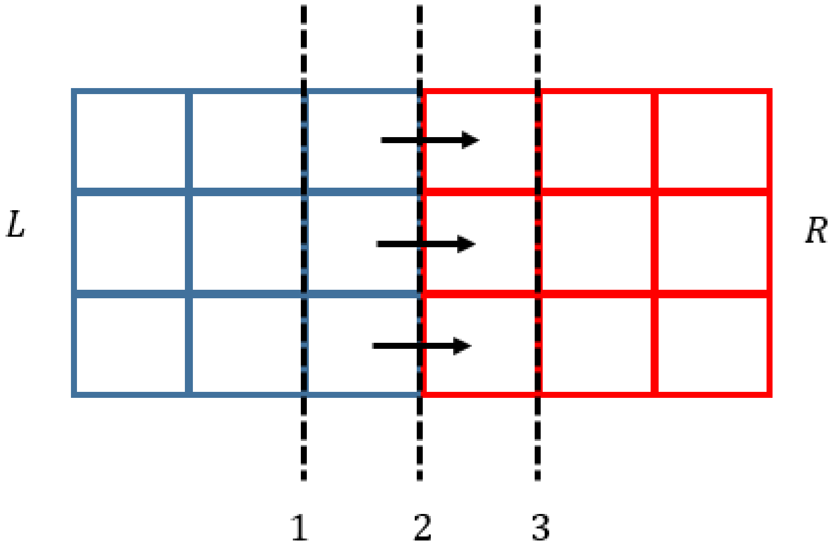

Figure 27: Pressure averaging

To clearly illustrate the pressure averaging region, **Figure 27** above is a pair of 3x3 cells. For the left coarse cell, the pressure averaging region is the region between line 1 and line 2. For the right coarse cell, the pressure averaging region is the region between line 2 and line 3. Each fine cell has its own pore volume and the DTOF which are used in **Eq. (2.43)** and **(2.44)**.

2.3.4 Pseudo-steady state results

Some PSS results will be shown in this section. From the PSS results, we will see that the local PSS diffuse source upscaling is not good enough to capture the local flow behavior precisely.

The first example is the result of effective permeability from the local PSS diffuse source upscaling. **Figure 28** below shows an example of the local DS PSS upscaling which yields an extremely abnormal low effective permeability. Flow is from left to right and the two cells with very low permeability are highlighted. In **Figure 28**(a) we see that almost all of the cell permeabilities are in the range of $10-20$ D, with the exception of two cells less than one mD. However, despite the reduction in permeability, these cells still have significant porosity, **Figure 28**(b), and therefore, these low permeability cells have diffuse source strengths that are comparable to any other cell. As a result, the pressure gradient between the two face cells will be very high, **Figure 28**(c), and therefore, we get an extremely low effective permeability result. Obviously, this extremely low effective permeability result does not reflect the true permeability distribution within the local coarse cells and the true cell connectivity. If we make use of the transient diffuse source concept, the time parameter in the transient diffuse source can help reduce the source weight in those low permeable cells, leading to the increased effective permeability result. For example, in **Figure 28**, with the use of the diffuse source time we expect to see that the low permeable cells will have negligible impact on the effective permeability result and the final inter-cell effective permeability will be large enough.

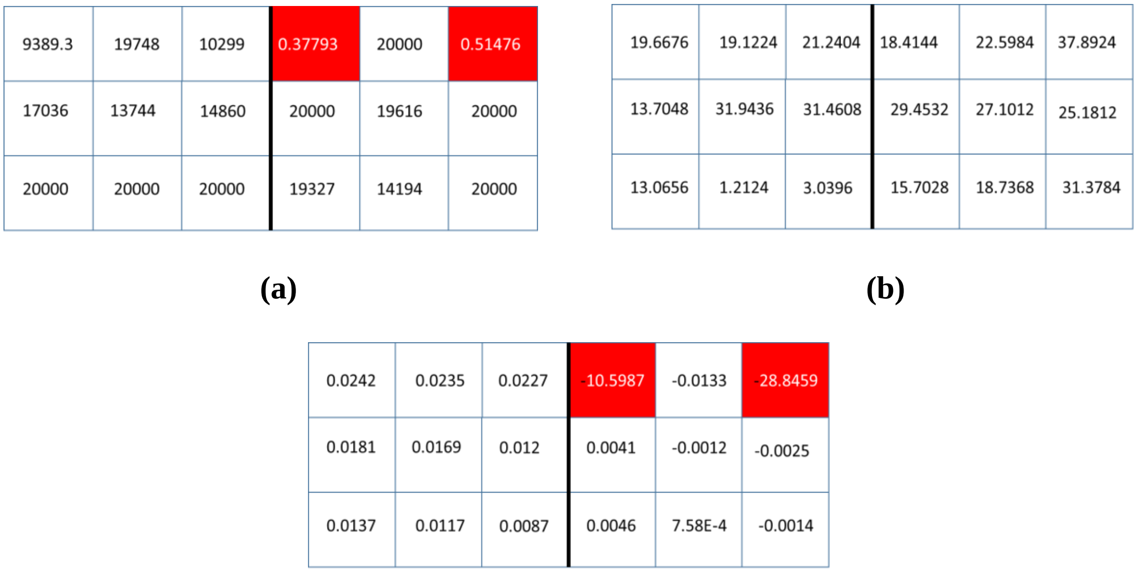

9389.3	19748	10299	0.37793	20000	0.51476
17036	13744	14860	20000	19616	20000
20000	20000	20000	19327	14194	20000

(a)

19.6676	19.1224	21.2404	18.4144	22.5984	37.8924
13.7048	31.9436	31.4608	29.4532	27.1012	25.1812
13.0656	1.2124	3.0396	15.7028	18.7368	31.3784

(b)

0.0242	0.0235	0.0227	-10.5987	-0.0133	-28.8459
0.0181	0.0169	0.012	0.0041	-0.0012	-0.0025
0.0137	0.0117	0.0087	0.0046	7.58E-4	-0.0014

(c)

Figure 28: Performance of the PSS diffuse source algorithm (3x3x1). (a) permeability. (b) pore volume. (c) DS PSS pressure (Nunna et al. 2015)

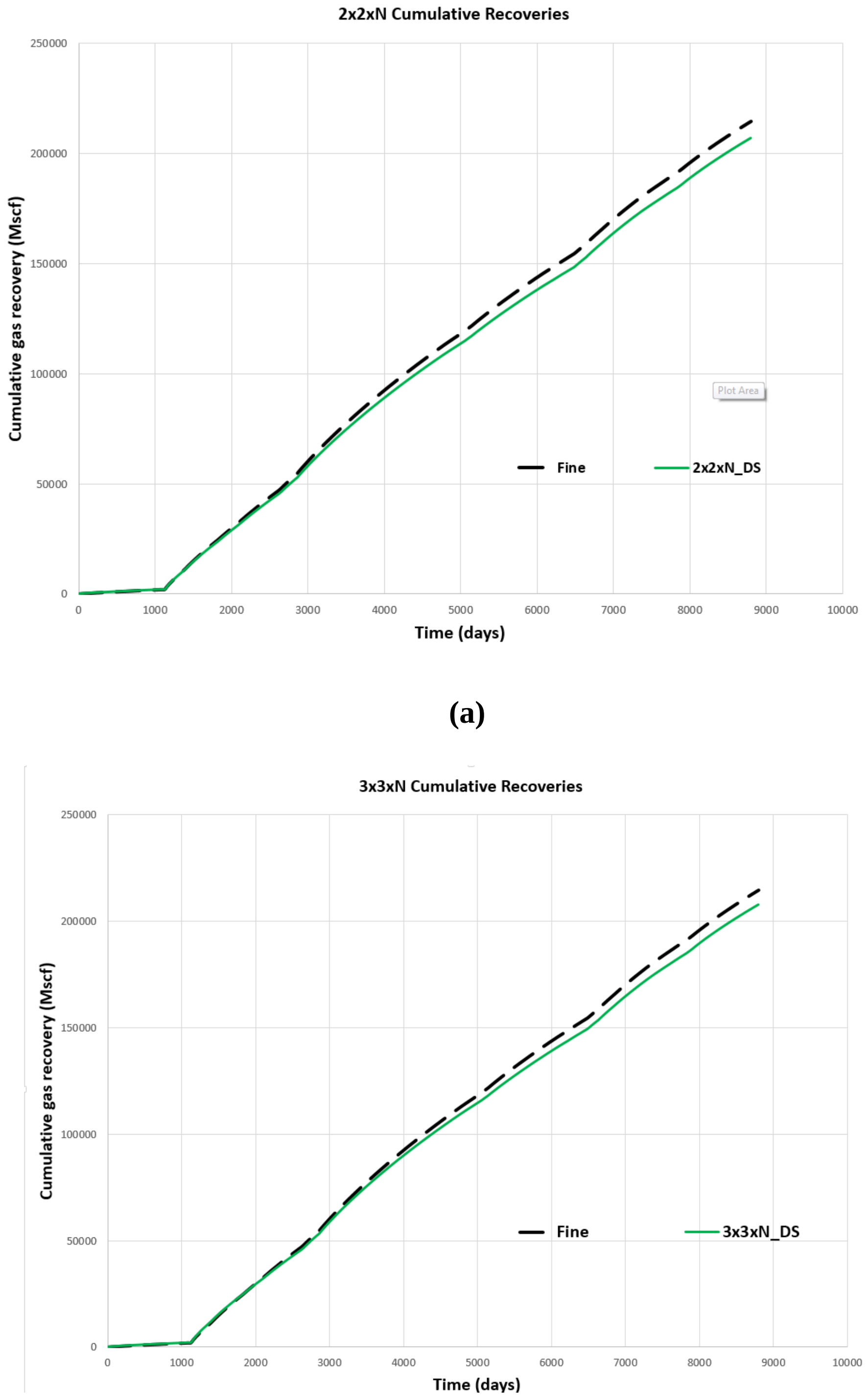

(a)

(b)

Figure 29: Tight gas pseudo steady state upscaling result. (a) 2x2xN. (b) 3x3xN.

The second example is the cumulative gas recovery result from upscaled tight gas model. The upscaled model is generated by PSS diffuse source upscaling with the local effective face permeability calculated according to the pressure averaging approach proposed in the last section. The adaptive upgridding approach (Zhou and King, 2011) is used to reduce the number of simulation grid cells and also preserve the vertical flow communication. $2 \times 2 \times \mathrm{N}$ and $3 \times 3 \times \mathrm{N}$ upscaling results are shown in **Figure 29**. These results are generated by Nunna et al. (2015). In **Figure 29** (a) and (b), the horizontal axis represents the production time and the vertical axis is the cumulative gas recovery. The black dash line represents the fine scale tight gas result and the light green solid line is the PSS diffuse source upscaling result. We can see that the PSS diffuse source upscaling result is lower than the fine scale result.

The third example is the cumulative oil production result from the $3 \times 3 \times 1$ upscaled SPE10 model. The $3 \times 3 \times 1$ upscaled model is generated by PSS diffuse source upscaling. Here I will show the comparison between the fine scale result and the PSS diffuse source upscaling result. In **Figure 30**, the vertical axis represents the cumulative oil production and the horizontal axis represents the oil production time. The black dash line represents the fine scale oil production result and the red solid line represents the PSS diffuse source upscaling result. Obviously, the cumulative oil production result obtained from the upscaled model is much lower than the fine scale result.

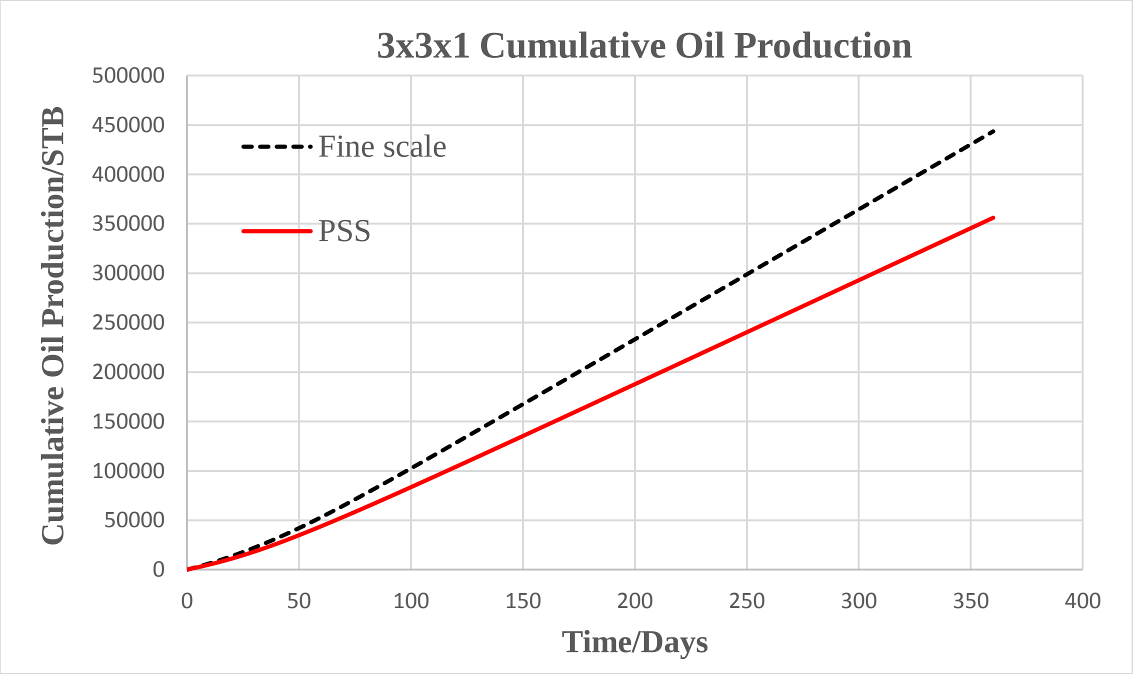

Figure 30: SPE10 3x3x1 pseudo steady state upscaling result

One reason for this large discrepancy is the use of the PSS diffuse source. In SPE10, especially in the bottom zone of this model, similar to the example shown in **Figure 28**, we will encounter many local coarse cells that are a mixture of very high permeable cells and very low permeable cells. The use of the PSS diffuse source will always lead to an erroneous result of the inter-cell effective permeability. Another reason for this underestimation is the strict no flow boundary condition. Here I will show two examples to illustrate the need to include the neighboring cells in the local upscaling. The first example is from the top zone and the second example is from the bottom zone.

The first example is from Layer 1.

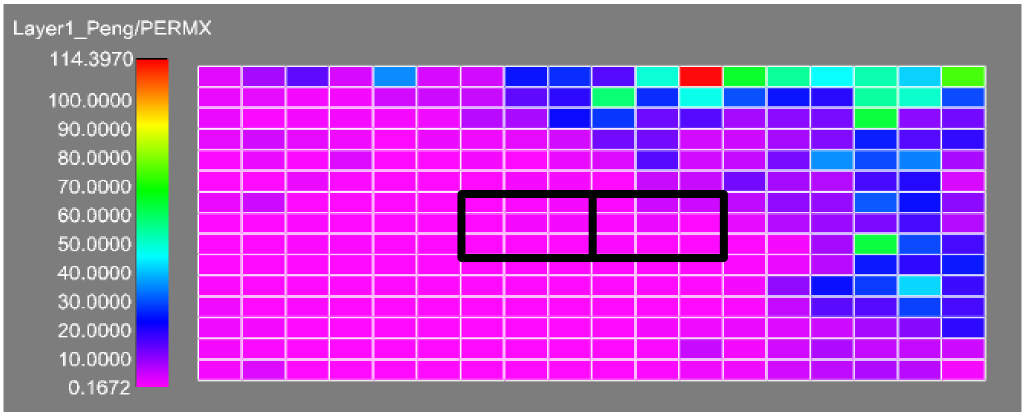

(a)

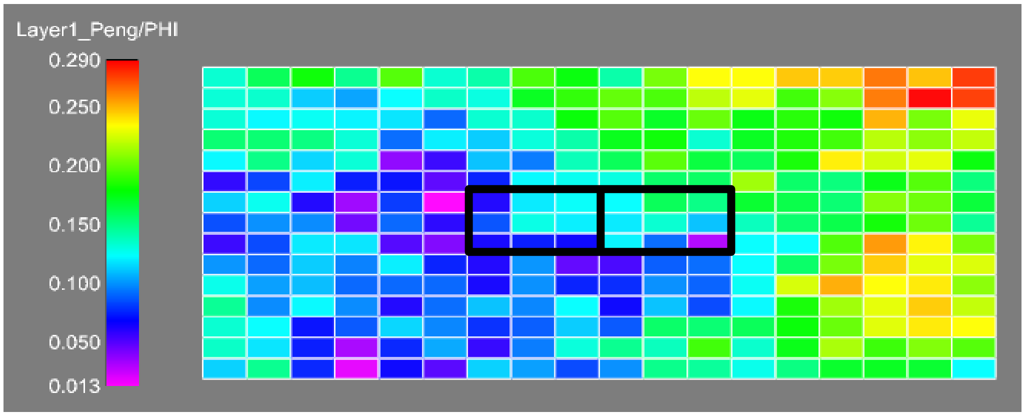

(b)

Figure 31: Permeability and porosity distribution (layer 1). (a) permeability. (b) porosity.

In **Figure 31**, the two black boxes denote the two upscaling coarse cells. The cells outside the boxes represent the buffering region. From **Figure 31**(a), the neighboring cells right outside the boxes have comparable permeability as the cells inside the boxes do. If we treat the common face of two coarse cells (the vertical bar in the middle) as the face with the DTOF τ equal to 0, we can calculate each fine cell DTOF with respect to that vertical bar.

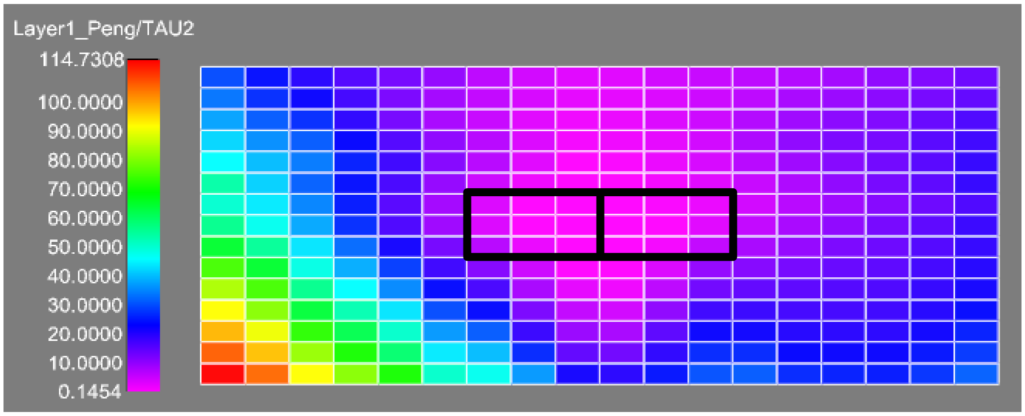

Figure 32**: The fine cell DTOF (layer 1)**

Figure 32 is the fine cell DTOF result with respect to the flux face in the middle. As we can see from this figure, in the region near to the flux face (the vertical bar in the middle), the cells have small DTOF value which is denoted by the purple color; in the region far from the flux face, the cells have relatively large DTOF. Since the local flow is driven by the diffuse source allocated in the fine cells and the diffuse source in each fine cell is proportional to its effective porosity defined by **Eq. (2.19.2)**, to show the need for the cells outside the local upscaling region, I also calculate the effective porosity of each fine cell related to the flux face and the result is in **Figure 33** below. From **Figure 33**, we see that outside the local upscaling region, there are still many cells having comparable diffuse source as the cells in the local upscaling region. These neighboring cells affect the internal flow in the upscaling region. It is necessary to add those neighboring cells into the local upscaling calculation.

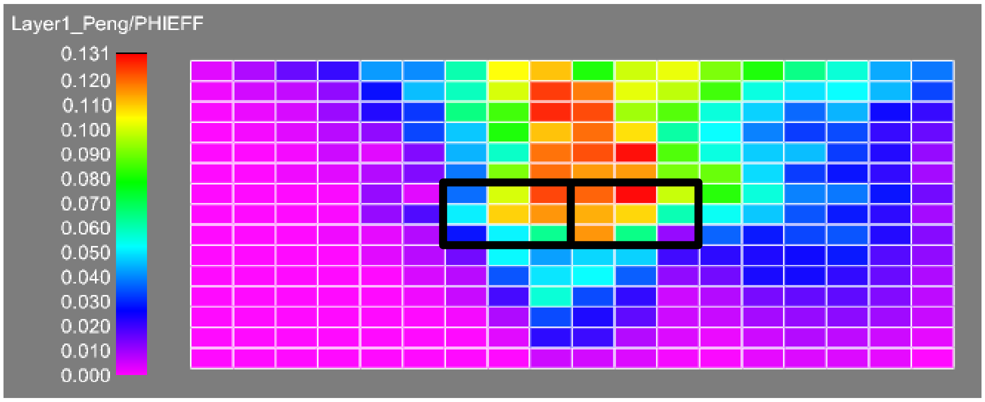

Figure 33: The fine cell effective porosity (layer 1)

The second example is from Layer 51. Similar to the first example, in **Figure 34**(a) we see in the region outside the black boxes the cells have comparable permeability as the cells inside the boxes. Also, in **Figure 36** the neighboring cells outside the boxes have comparable diffuse source as those cells in the upscaling region.

All the examples shown in this section lead us to make use of transient diffuse source which can reduce the impact of the low permeable cells. Also, the last two examples show that we need to consider adding more cells into the upscaling calculation. In next section, we will be focused on the discussion on the specification of the diffuse source time and the upscaling computational region.

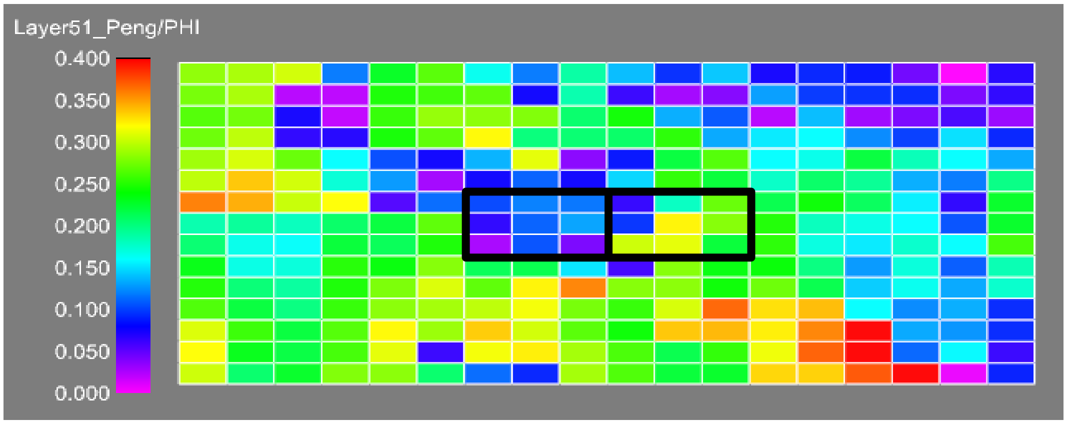

(a)

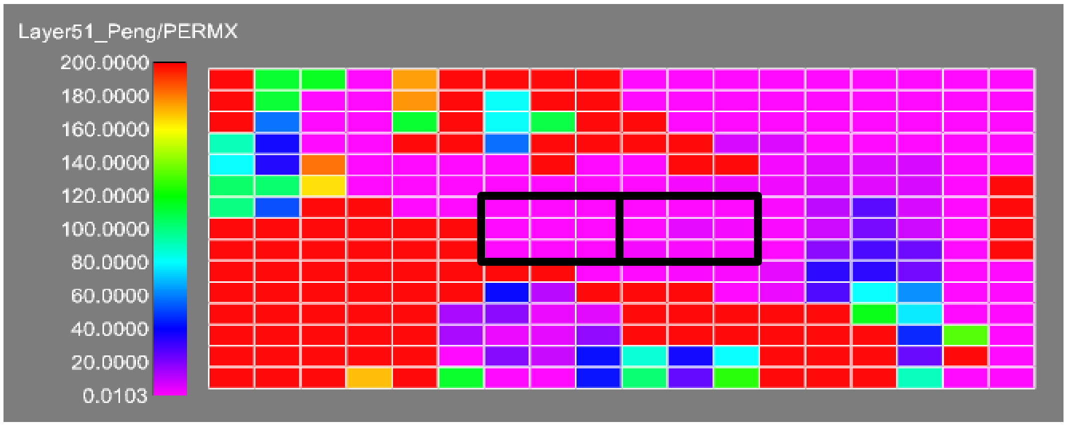

(b)

Figure 34: Permeability and porosity distribution (layer 51). (a) permeability. (b) porosity.

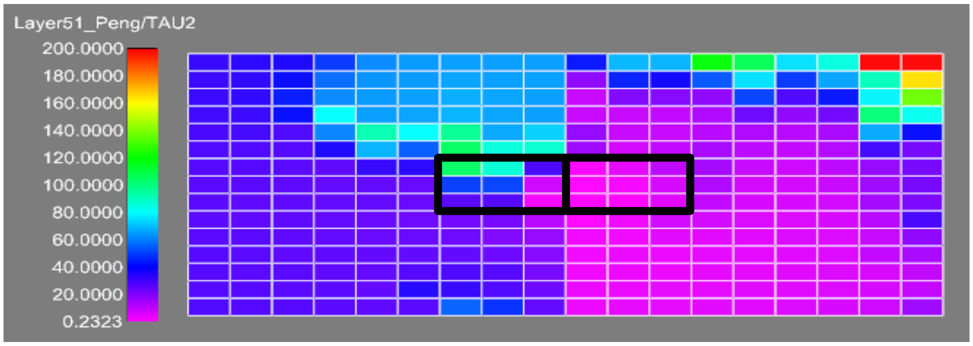

Figure 35: The fine cell DTOF (layer 51)

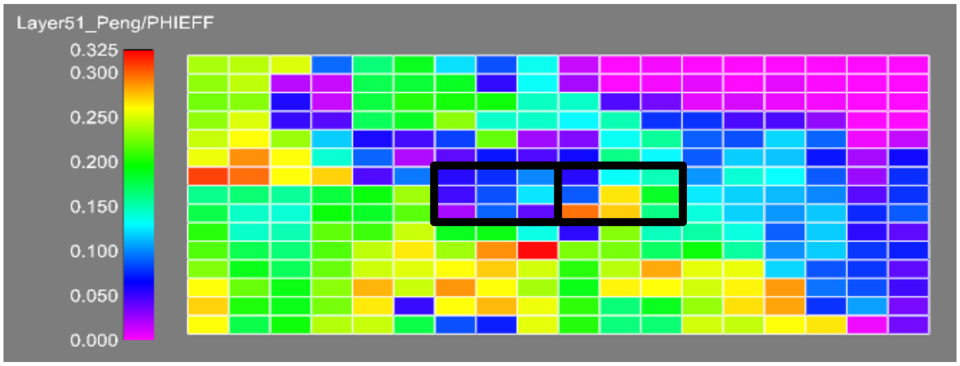

Figure 36: The fine cell effective porosity (layer 51)

2.3.5 Specification of diffuse source time and upscaling computational region

In this section, we will discuss how to determine the diffuse source time which is needed in the transient diffuse source upscaling. Also, we will discuss the effect of extending the upscaling computational region from the local coarse cell to a larger domain. The diffuse source time is fixed as we study how the effective permeability is sensitive to the computational domain.

2.3.5.1 Diffuse source time equation

First, let us focus on the specification of diffuse source time. Since the diffuse source time is used to convey the information about the radius of investigation from the impulse, it is correlated with the internal fine cell DTOF because the DTOF can be used to characterize the slowness of the pressure wave front propagation from the impulse source/sink. In addition, as mentioned in Section 2.3.1, in DS upscaling, locally the impulse source and sink are imposed at common interface of adjacent two coarse cells and the source and sink are triggered at the same time. Therefore, the diffuse source time in the source coarse cell should be the same as the diffuse source time in the sink coarse cell. In this way, we can capture the difference of the pressure wave front propagation in the two coarse cells which arises from the heterogeneity of the petrophysical properties (permeability and porosity). Also, the diffuse source time of a coarse cell should distinguish the extremely low permeable cells from the high permeable cells and reduce the impact of those extremely low permeable cells on the effective permeability results. Last but not the least, the diffuse source time should make sure that most of relatively high permeable fine cells within the two connected half coarse cells are well connected to the coarse cell flux face.

Now we come to the question what equation we should use to calculate the diffuse source time. To answer this question, we will ask another question: when will the entire coarse cell begin to reach pseudo steady state in the local DS upscaling? According to **Eq. (2.21)**, we know that the fine cell diffuse source is proportional to the exponential term $\mathrm{e}^{-\tau^2/4\mathrm{t}}$ where τ denotes the fine cell DTOF and t is the diffuse source time. Therefore, if the diffuse source exponential term of most of the fine cells is smaller than $1/\mathrm{e}$, we can say that the coarse cell begins to reach pseudo steady state. This implies the following equation for the diffuse source time:

$$\mathrm{t} = \frac{(\tau_c)^2}{4} \ldots\ldots\ldots\ldots\ldots\ldots\ldots\ldots\ldots\ldots\ldots\ldots\ldots\ldots\ldots\ldots\ldots\ldots\ldots\ldots. (2.45)$$

where τ_c denotes the characteristic DTOF for the coarse cells in the local DS upscaling. Here we take this characteristic DTOF τ_c as $2\tau_{avg}$ where τ_{avg} is an average DTOF of the fine cells in upscaling. The reason why we choose $2\tau_{avg}$ is that in the limit of the homogeneous situation $2\tau_{avg}$ is the DTOF at the coarse cell boundary. Therefore, in the following discussion, we will use the following equation to determine the diffuse source time:

$$t = \frac{\left(2\tau_{avg}\right)^2}{4} = \tau_{avg}^2 \ldots\ldots\ldots\ldots\ldots\ldots\ldots\ldots\ldots\ldots\ldots\ldots\ldots\ldots\ldots\ldots\ldots\ldots\ldots\ldots. (2.46)$$

Now we will discuss how to calculate the average DTOF τ_{avg}. Here we propose four methods that may be used to determine the average DTOF. The first method is described by the following equation:

$$\tau_{avg} = \frac{\sum_{i=1}^{N} \tau_i PV_i e^{-\frac{\tau_i^2}{4t}}}{\sum_{i=1}^{N} PV_i e^{-\frac{\tau_i^2}{4t}}} \ldots\ldots\ldots\ldots\ldots\ldots\ldots\ldots\ldots\ldots\ldots\ldots\ldots\ldots\ldots\ldots\ldots\ldots\ldots\ldots (2.47)$$

This equation indicates that the coarse cell average DTOF is equal to the effective pore volume weighted average of τ and the diffuse source time t can be solved iteratively by substituting **Eq. (2.47)** into **Eq. (2.46)**. This method is called “L1-iteration”. In **Eq. (2.32)**, if we replace the effective pore volume by the fine cell pore volume, we have the second method:

$$\tau_{avg} = \frac{\sum_{i=1}^{N} PV_i \tau_i}{\sum_{i=1}^{N} PV_i} \dots \dots (2.48)$$

This method is called "L1-noniteration". In the third method, the square of the coarse cell average DTOF is equal to the effective pore volume weighted average of τ^2 and it is also solved iteratively.

$$\tau_{avg}^2 = \frac{\sum_{i=1}^{N} \tau_i^2 PV_i e^{-\frac{\tau_i^2}{4t}}}{\sum_{i=1}^{N} PV_i e^{-\frac{\tau_i^2}{4t}}} \dots \dots (2.49)$$

This method is called "L2-iteration". In the last method, the square of the coarse cell average DTOF is determined by the pore volume weighted average of τ^2:

$$\tau_{avg}^2 = \frac{\sum_{i=1}^{N} PV_i \tau_i^2}{\sum_{i=1}^{N} PV_i} \dots \dots (2.50)$$

This method is called "L2-noniteration". In **Eq. (2.47-2.50)**, "PV" stands for the fine cell pore volume; N represents the number of fine cells in some specific coarse cell. In every local upscaling, we have four different choices for the value of diffuse source time. To find out which method we may use in the upscaling, I select several different examples from the SPE10 model and the time sensitivity test is conducted based on these selected examples. The time sensitivity test is designed in the way that each diffuse source time determined by one of the four methods is multiplied by a time coefficient factor which varies from 0.01 to 10000 and then we see how the effective face permeability between the two coarse cells varies with this coefficient factor. In each example I will show four sensitivity results each of which corresponds to one of the four methods. The final decision on which method we may use is made based on the following two conditions:

The first condition is how stable the effective permeability is at the diffuse source determined by each method. The second condition is whether the effective permeability can capture the main feature of the fine cell permeability in the local coarse cell. In other words, if the upscaling region is in the high permeable area, then we expect the resulting effective permeability should have a high value; if the upscaling region is in the very low permeable area, then we expect the resulting effective permeability should have a very low value.

Since the upscaling computational region also affects the effective permeability result, the spatial sensitivity test is carried out along with the time sensitivity test. In the spatial sensitivity test, the coarse cell diffuse source time is fixed and we increase the size of the computational domain. When the computational domain is large enough, the boundary condition of the local upscaling based on the extended computational region can be approximated by the no flow boundary condition. Similarly, this is because the diffuse source in every fine cell has an exponential term $e^{-\frac{\tau^2}{4t}}$. When the size of the computational domain is increased, the DTOF τ of the cells on the boundaries also increases. With the diffuse source time fixed and when the size of the computational region is large enough, the diffuse source of the cells on the boundaries will be approximately zero and therefore, the corresponding boundary condition of the extended computational region can be thought as no flow boundary condition. In addition, at the time when the computational region is large enough, the local coarse cell is approximately in the pseudo-steady state and the resulting effective permeability will be stabilized with respect to the upscaling computational domain.

2.3.5.2 Time sensitivity test and spatial sensitivity test

Now we will see several examples for the sensitivity test. The first example is from the bottom zone of the SPE10 model. **Figure 37** below shows the permeability and porosity distribution in the local coarse cells. From **Figure 37** we see that the fine cells in the upscaling coarse cells have very low permeability, but the porosity is not very low. Because in the upscaling here we emphasized the interaction between the local coarse cells and the cells outside the coarse cells, the permeability and porosity of the cells outside the local coarse cells is also shown in **Figure 38**. In **Figure 38**, the region within the black boxes in the middle layer is the upscaling region. The cells on the top layer and the bottom layer are treated as the buffering region. From **Figure 38**, we can see that the coarse cells are in the low permeable region. Not very far from the coarse cells, there is a patch of high permeable area.

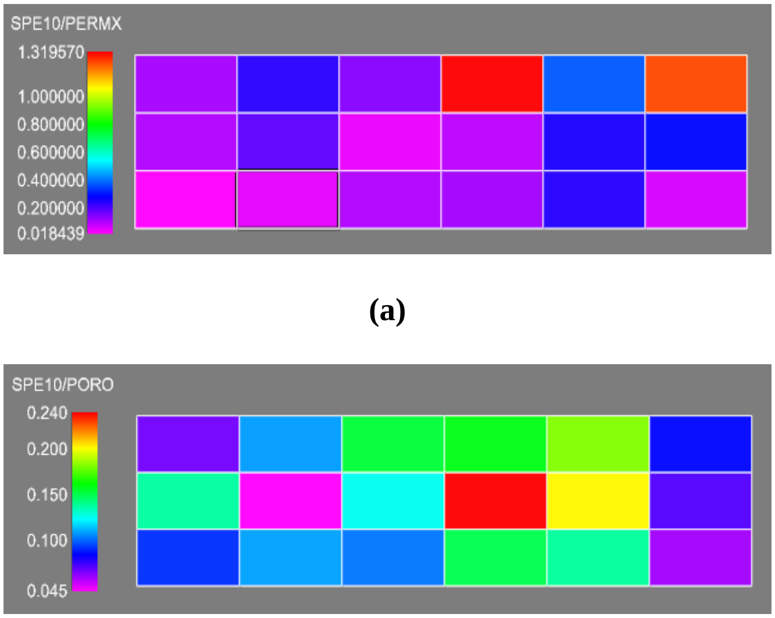

(a)

(b)

Figure 37: Coarse cell permeability and porosity distribution (example 1). (a) permeability. (b) porosity.

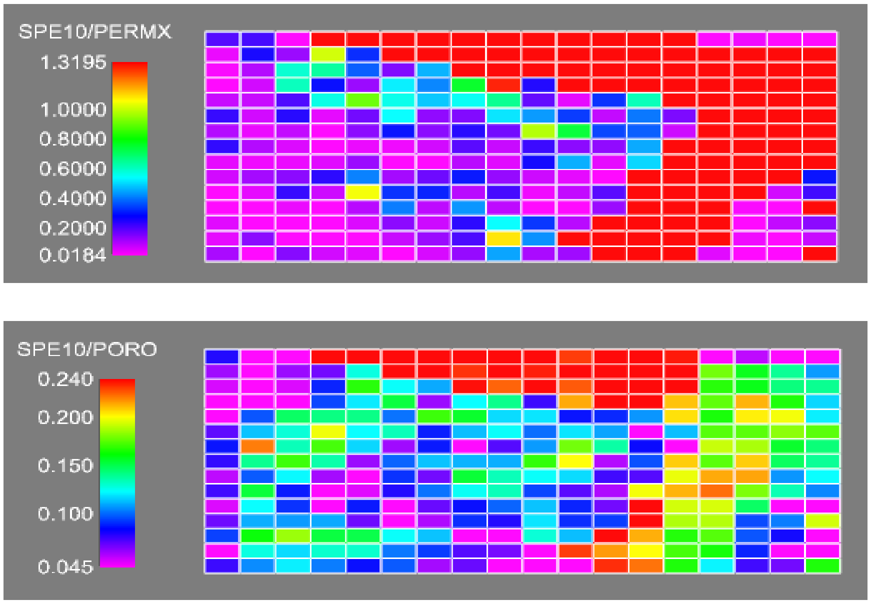

(a)

Figure 38: Permeability and porosity distribution (example 1). (a) top layer. (b) middle layer. (c) bottom layer.

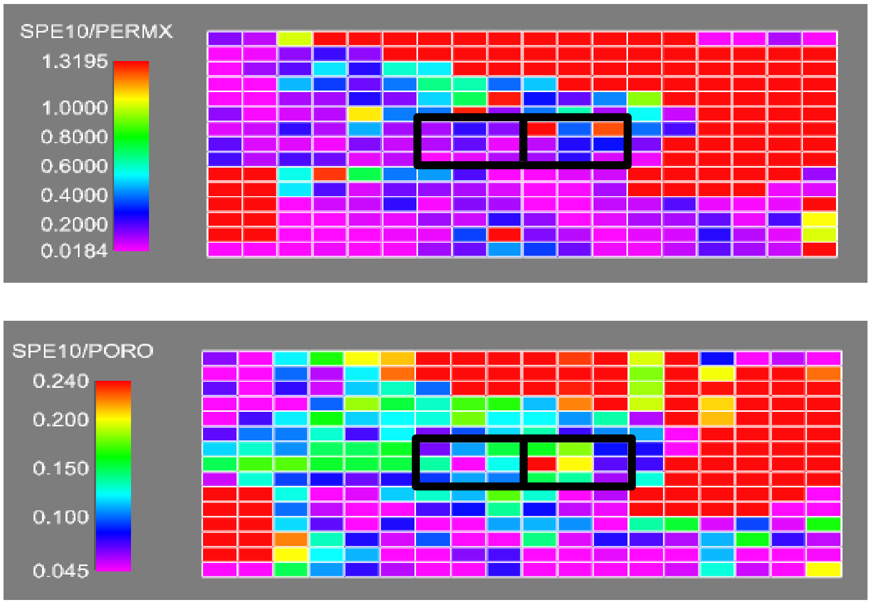

(b)

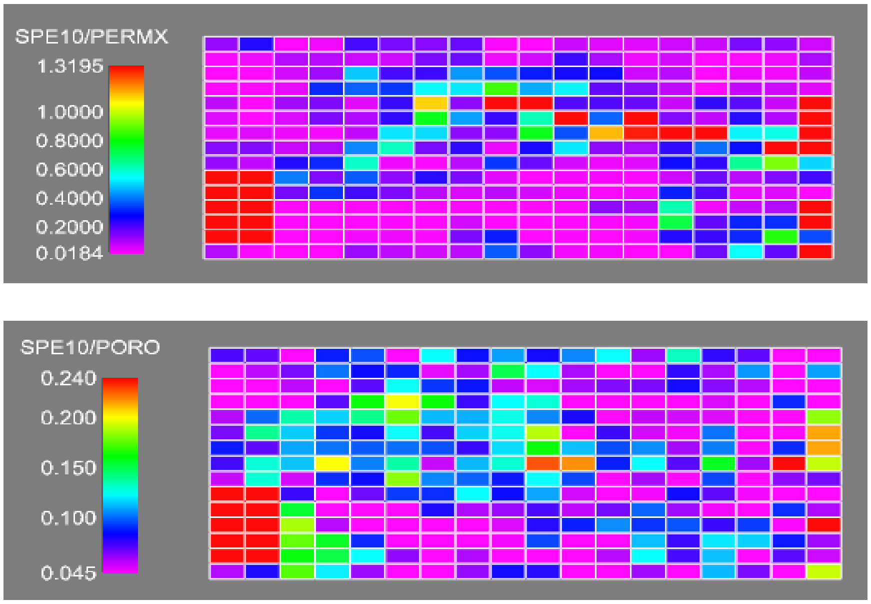

(c)

Figure 38 Continued

For the convenience of the latter discussion, first I will explain how I name different buffering regions. Horizontally, I use the word “ring” to define the buffering regions. **Figure 39** below shows us a 1 ring buffering region. The cells denoted by the grey shaded boxes form a ring around the coarse cells and therefore, the buffering region is named as “1 ring”. The name of the buffering region depends on how many rings are formed by the cells in the buffering region. For example, 6 ring buffering region means that the cells in the buffering region used for the upscaling form 6 rings.

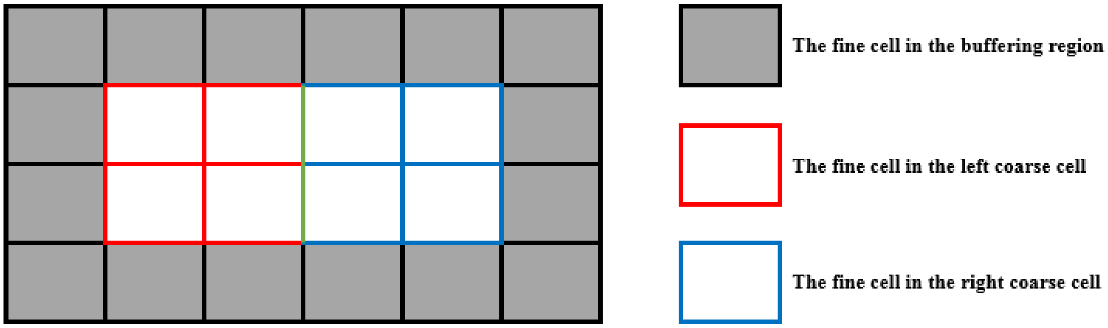

Figure 39: 1 ring buffering region

Vertically, I use the word “2D” or “3D” to distinguish whether the layers above and below the coarse cells are added into the computational region. If the buffering region is three dimensional (3D), above and below the target coarse cells we have the same number of layers added into the computational region. For example, the name “6 ring-3D-1 layer” means horizontally the buffering region is 6 ring and vertically there is one layer above and one layer below the upscaling coarse cells. The result of time sensitivity test and spatial sensitivity test is as follows:

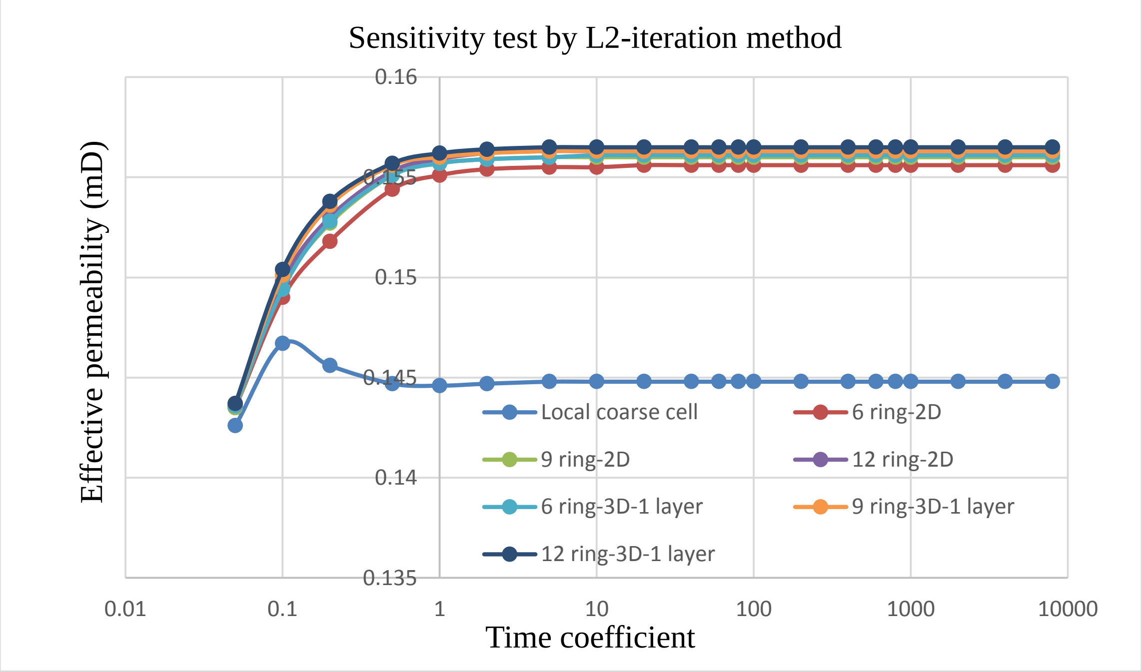

(a)

Figure 40: Sensitivity test result of the first example (a) L2-iteration method. (b) L1-iteration method. (c) L2-noniteration method. (d) L1-noniteration method.

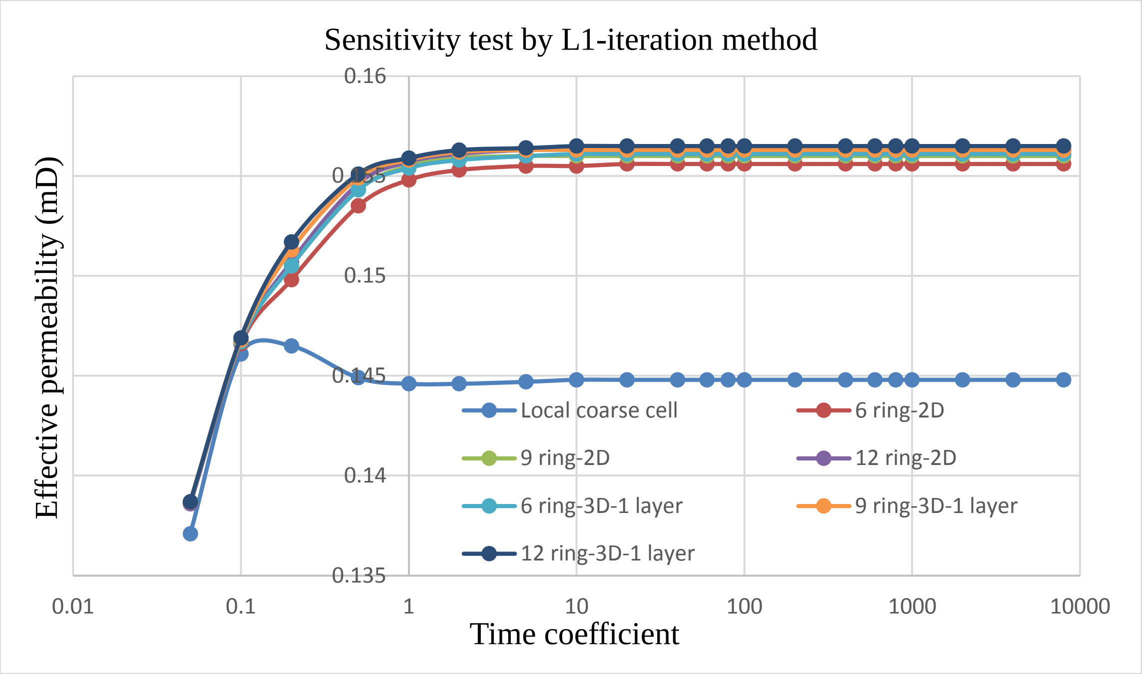

(b)

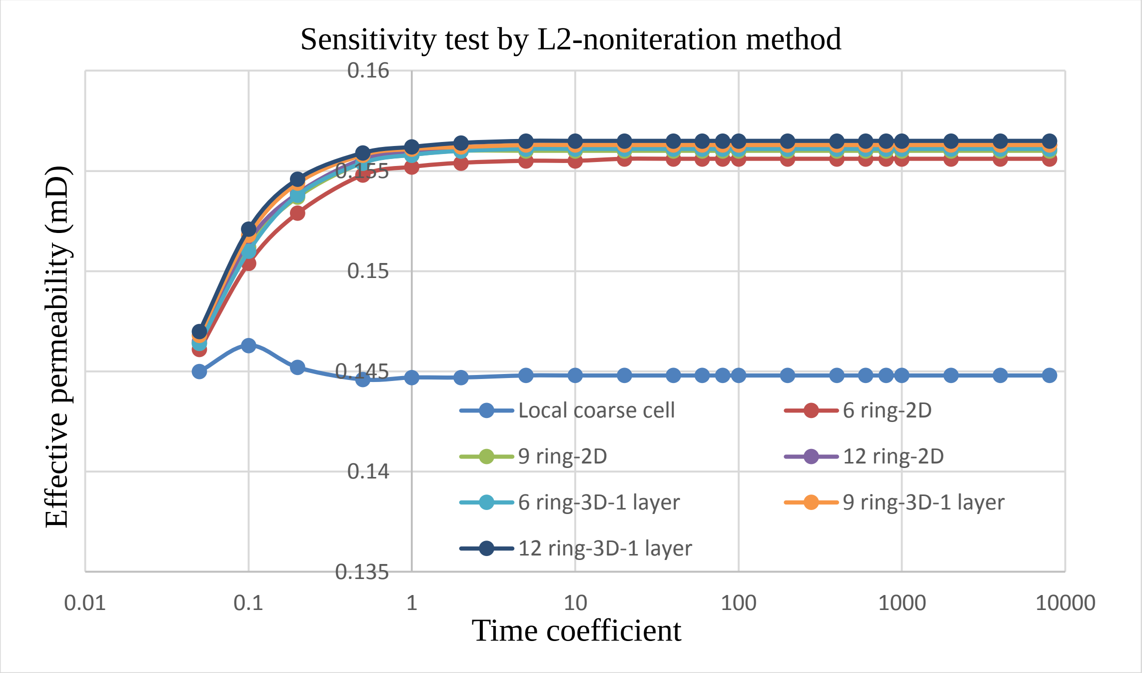

(c)

Figure 40 Continued

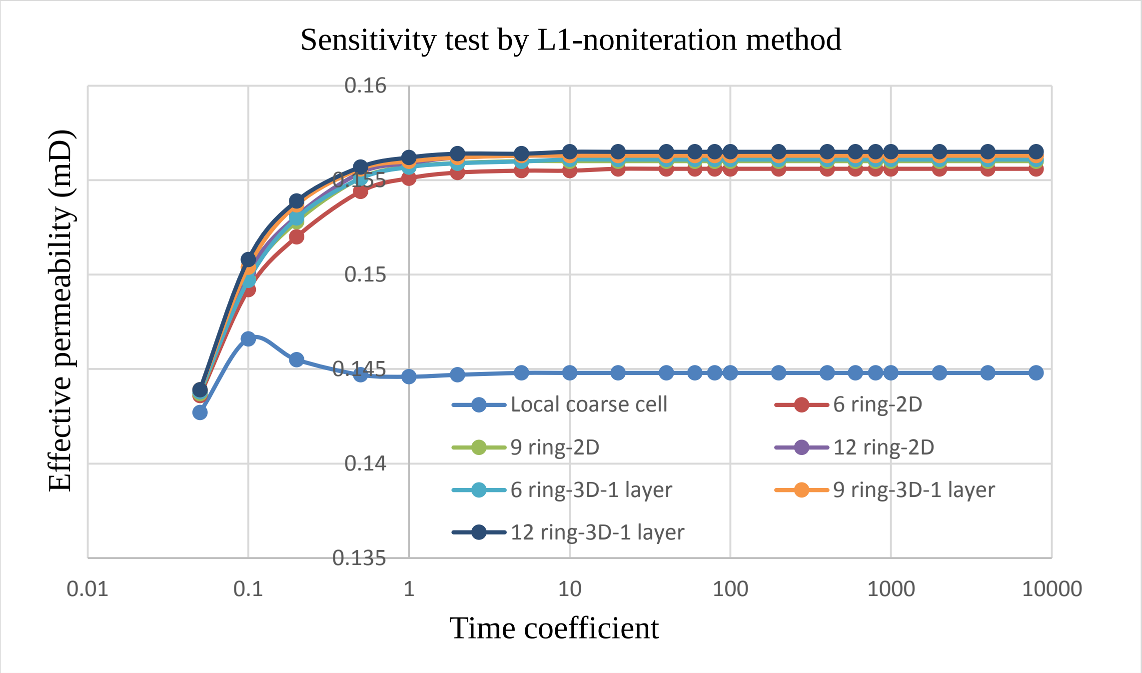

(d)

Figure 40 Continued

The four values of the averaged DTOF are shown in **Table 1**:

	L2-iteration	L1-iteration	L2-noniteration	L1-noniteration
averaged DTOF square (hour)	5.31	3.79	7.58	6.27

Table 1: Diffuse source time (example 1)

From this example, we can see that the coarse cell diffuse source time calculated by the four methods is not very different. The sensitivity results based on the four different methods are similar. In each plot, horizontally we can know how the effective permeability is sensitive to the coarse cell diffuse source time; vertically we can know how the effective permeability is sensitive to the computational domain used for the local upscaling. From **Figure 40**, we see that the effective permeability at the time coefficient equal to 1 is located in the stable region. Also, the size of the computational domain does not need to be very large before the effective permeability result get stable with respect to the variation of the upscaling computational domain. Horizontally, 6 ring buffering region is already large enough for a stable effective permeability. Vertically, we see that the 2D result is very close to the 3D result in the first example.

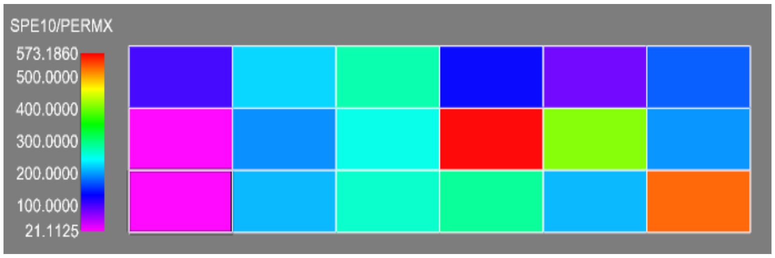

(a)

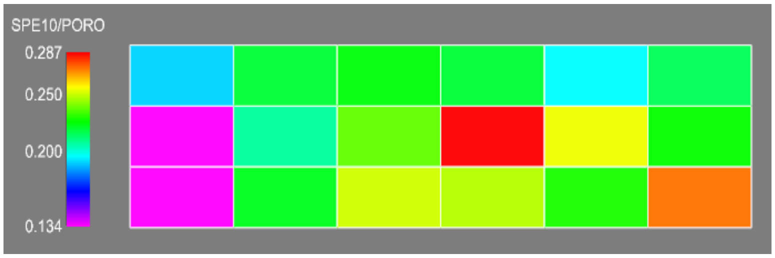

(b)

Figure 41: Coarse cell permeability and porosity distribution (example 2). (a) permeability. (b) porosity.

The second example is from the top zone of SPE10 model and most of the fine cells in the coarse cells have high permeability and porosity. **Figure 41** above shows the fine cell permeability and porosity in the coarse cells. The permeability and porosity of the cells outside the coarse cells is shown in **Figure 42**. From **Figure 42**(b), we see that the upscaling coarse cells are located within the high permeable area.

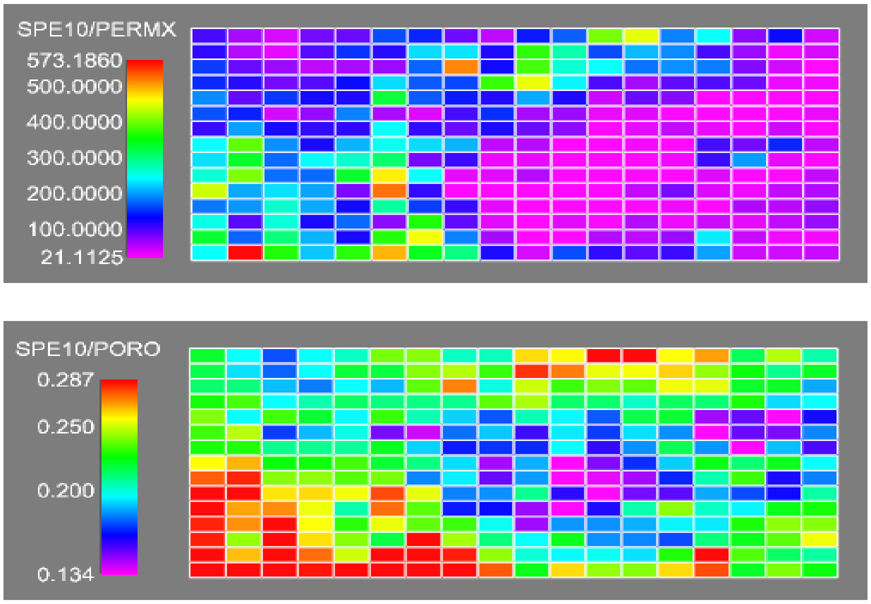

(a)

Figure 42: Permeability and porosity distribution (example 2). (a) top layer. (b) middle layer. (c) bottom layer.

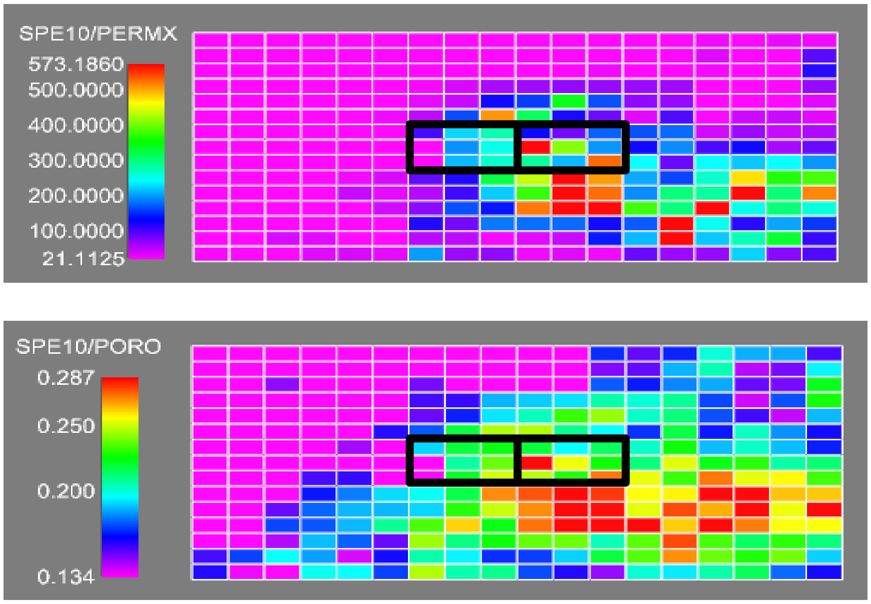

(b)

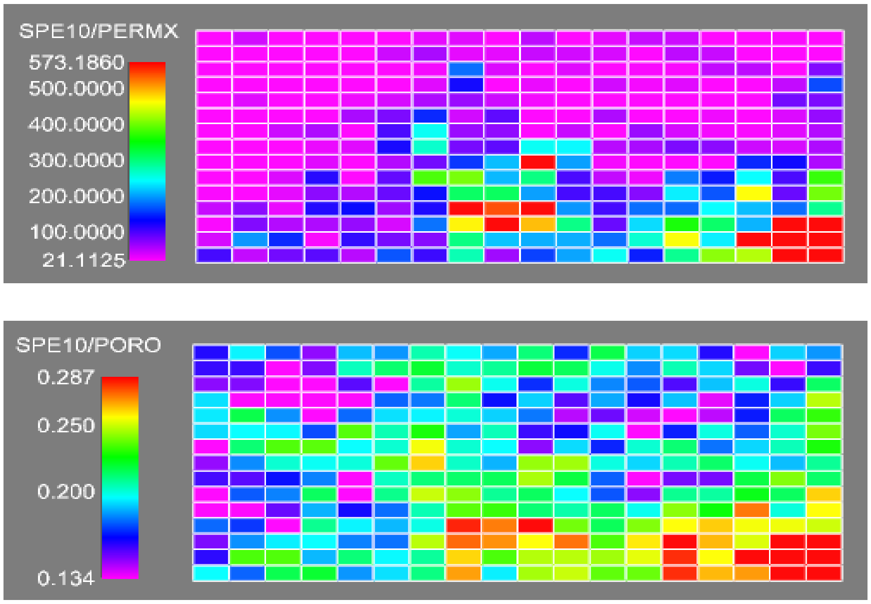

(c)

Figure 42 Continued

The result of time sensitivity test and spatial sensitivity test is as follows:

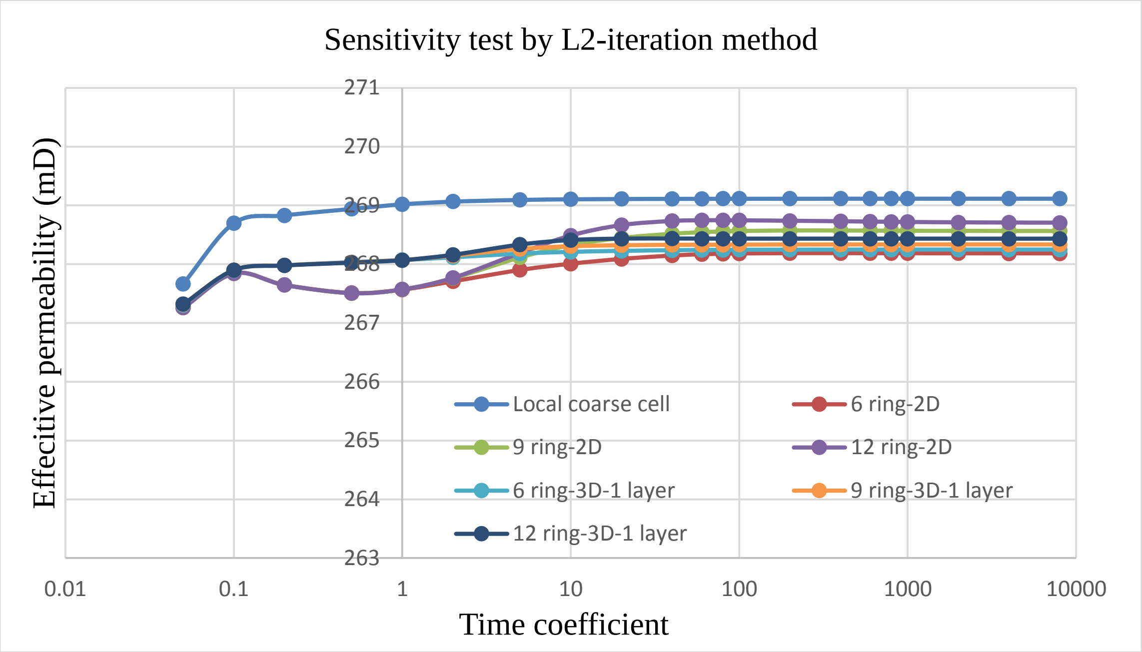

(a)

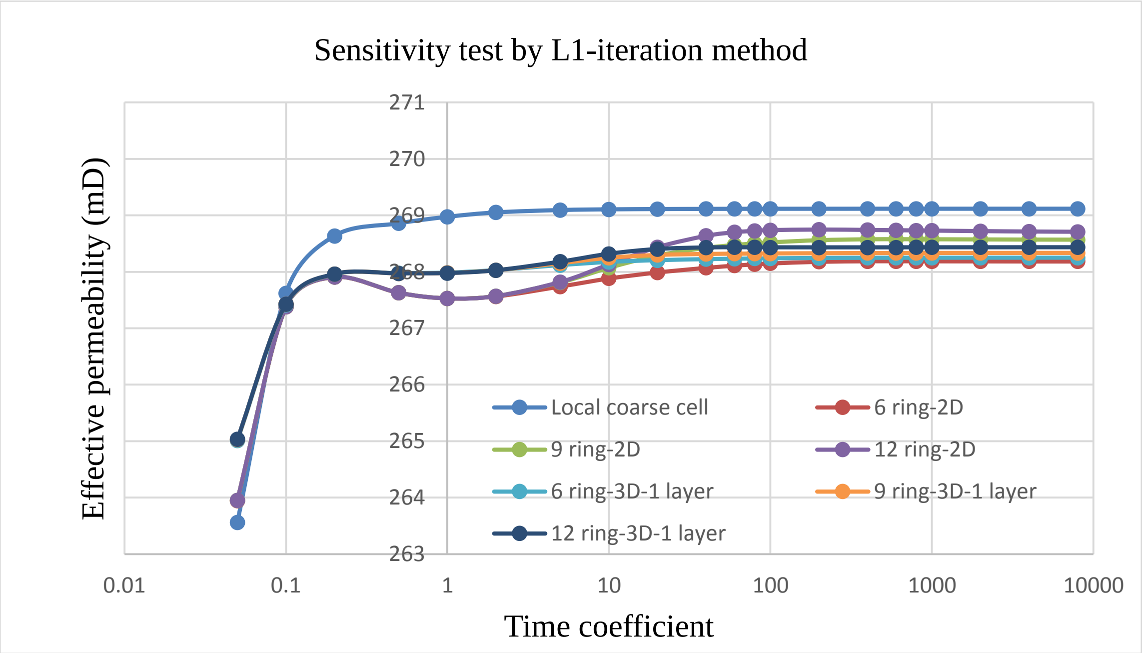

(b)

Figure 43: Sensitivity test result of the second example (a) L2-iteration method. (b) L1-iteration method. (c) L2-noniteration method. (d) L1-noniteration method.

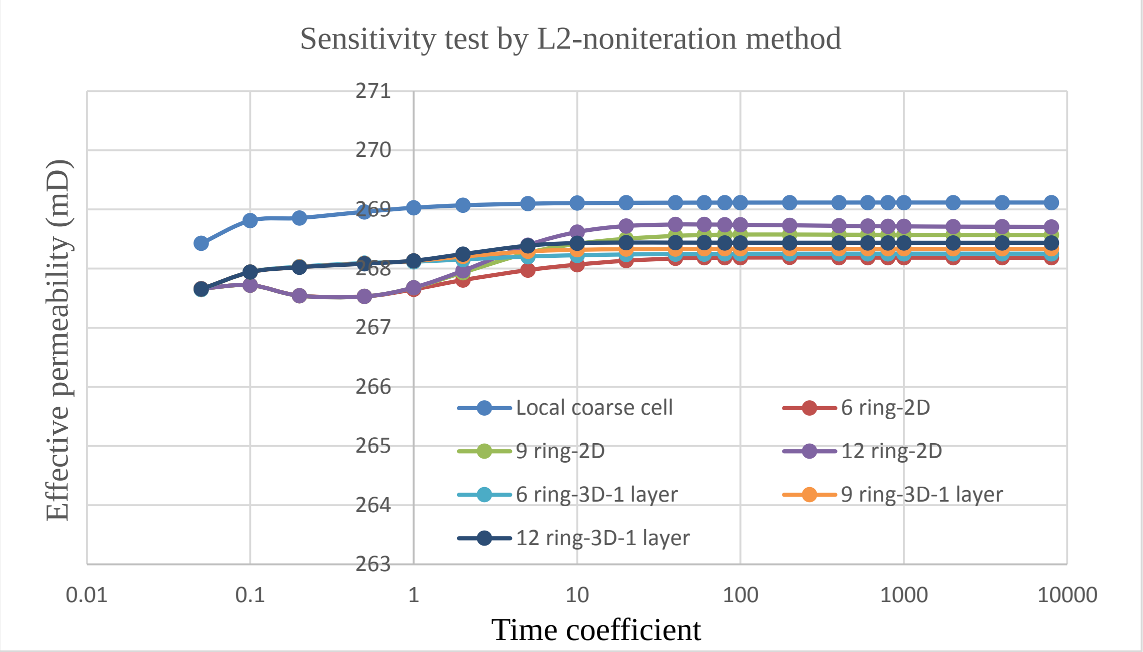

(c)

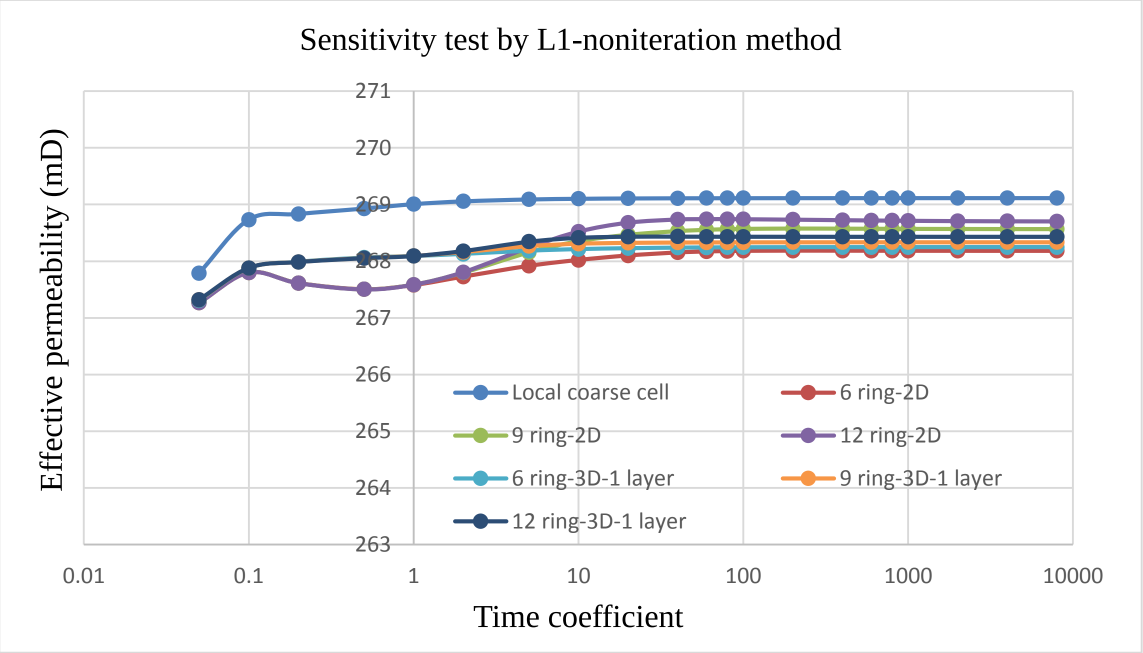

(d)

Figure 43 Continued

The four values of the averaged DTOF are shown in **Table 2**:

	L2-iteration	L1-iteration	L2-noniteration	L1-noniteration
averaged DTOF square (hour)	5.41E-3	3.37E-3	8.69E-3	6.43E-3

Table 2: Diffuse source time (example 2)

In this example, L1-iteration method yields the smallest diffuse source time, while all the other methods yield the comparable diffuse source time. All the four plots are similar. In time sensitivity test, as the time coefficient changes, we see that the change of the effective permeability result is very small. In addition, we can see from the plots that the 2D upscaled effective permeability is very close to the 3D upscaled effective permeability. Horizontally, the effective permeability gets stable very fast before we need more rings for upscaling. 6 ring buffering region is large enough. Also, the value of the effective permeability is in an acceptable range according to the permeability distribution in the local coarse cell.

According to these two examples, we cannot distinguish which method we may use because the results given by these four methods are very close, but we see that we do not need very large computational region to make sure the effective permeability result gets stable. In addition, the local coarse cells in these two examples do not have the cells that are highly contrasted in permeability. However, in SPE10 model, as is introduced in

Section 2.2, there are many coarse cells which are mixture of very high permeable cells and very low permeable cells. The real challenging in upscaling is the upscaling of those high contrast coarse cells. Therefore, next I will show several high contrast examples and the discussion will be made based on the effective permeability sensitivity result.

Next we have the third example. The two coarse cells in the black boxes are the cells for upscaling. From **Figure 44**(b) we can see that the coarse cells are located at the interface of the channel barrier. Most part of the coarse cells is in the very low permeable region while a small part is in the high permeable channel region. In **Figure 44**, only part of the buffering region is shown.

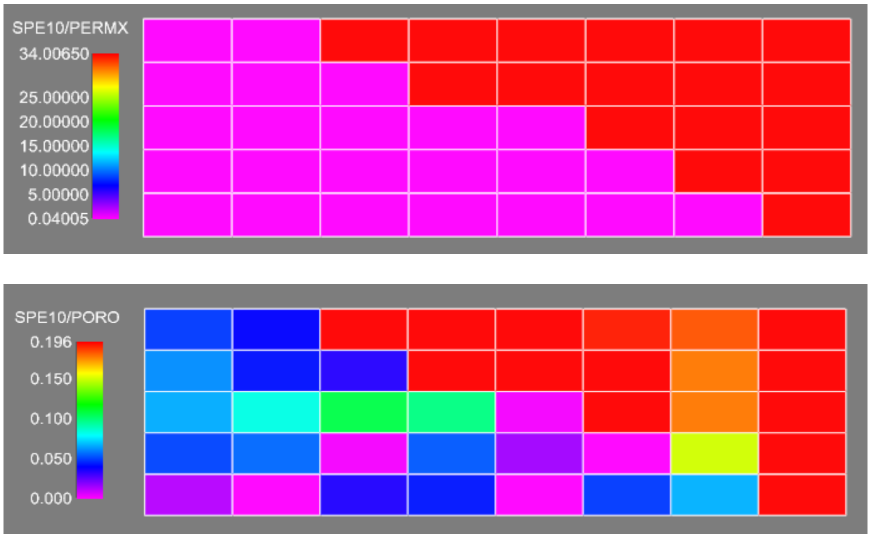

(a)

Figure 44: Permeability and porosity distribution (example 3). (a) top layer. (b) middle layer. (c) bottom layer.

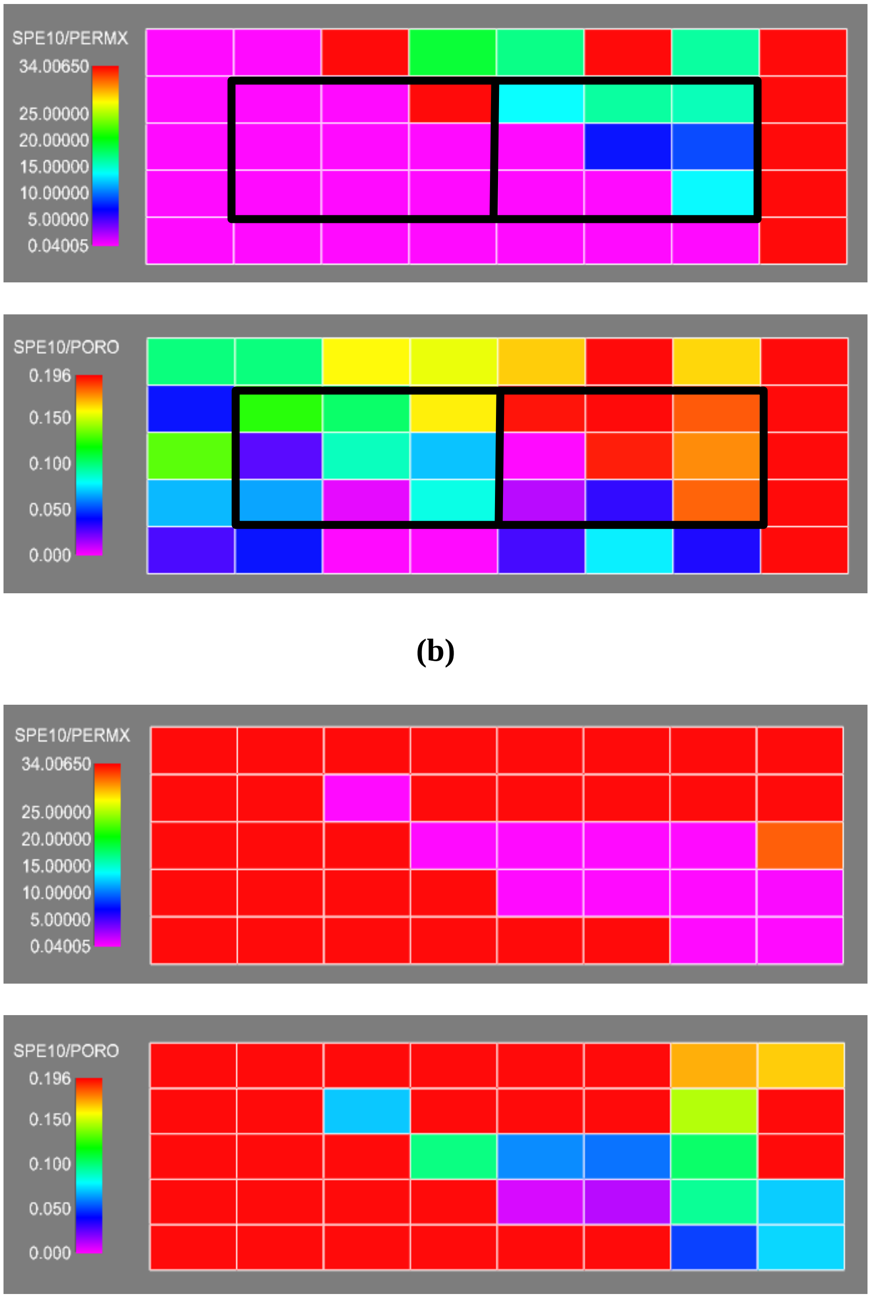

(b)

(c)

Figure 44 Continued

Here is the time sensitivity and spatial sensitivity result for the third example:

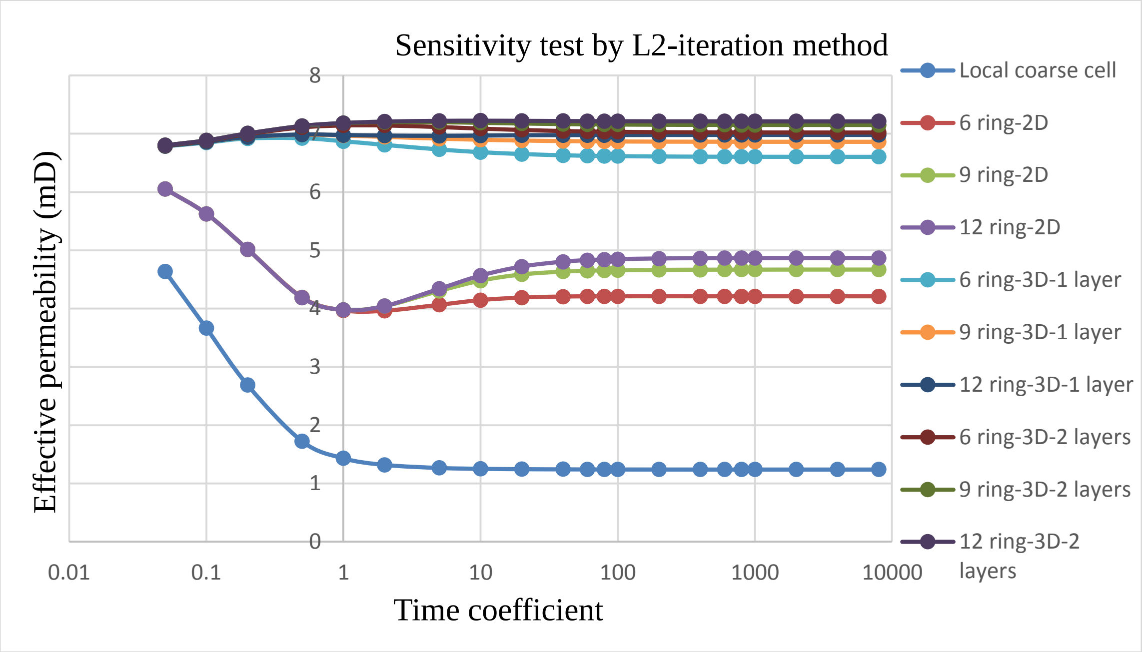

(a)

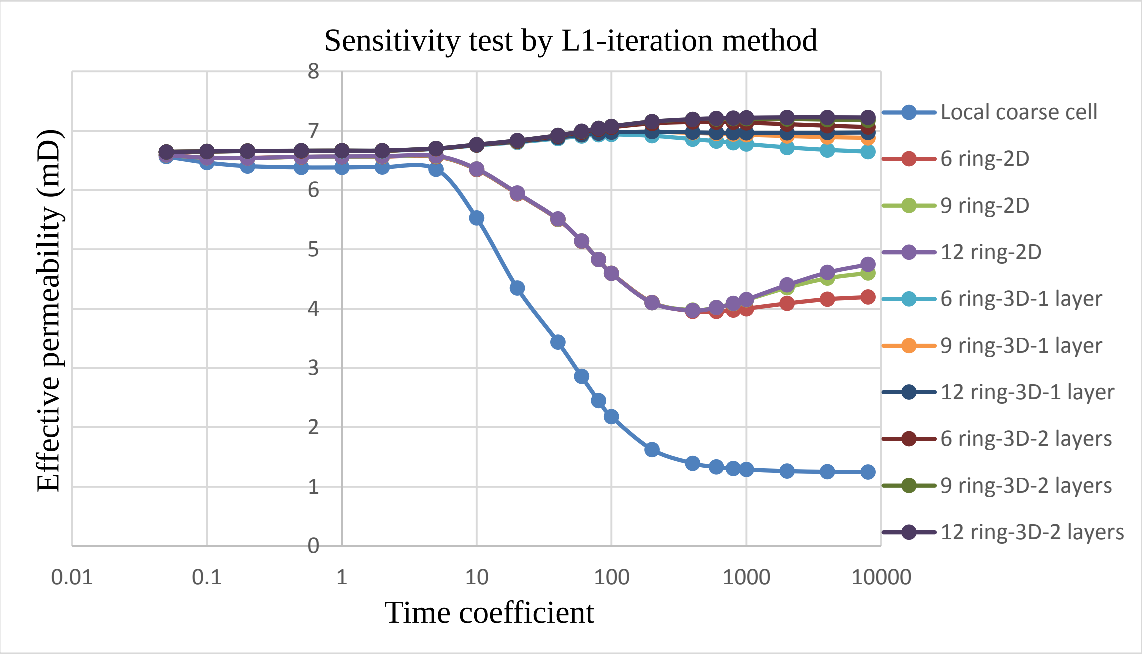

(b)

Figure 45: Sensitivity test result of the third example (a) L2-iteration method. (b) L1-iteration method. (c) L2-noniteration method. (d) L1-noniteration method.

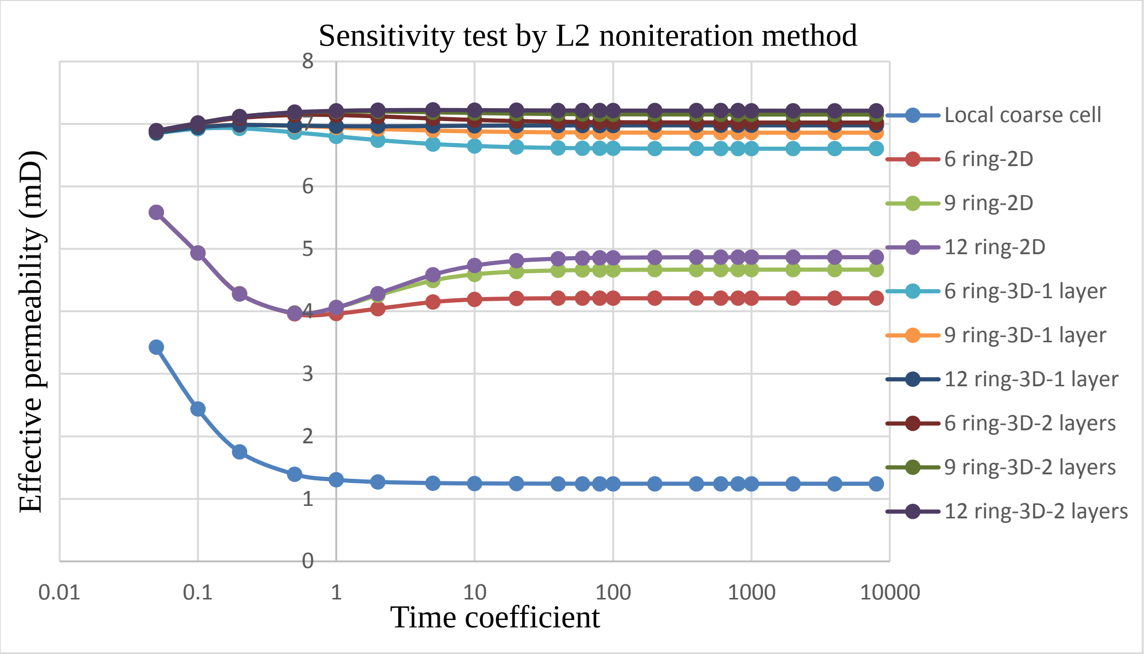

(c)

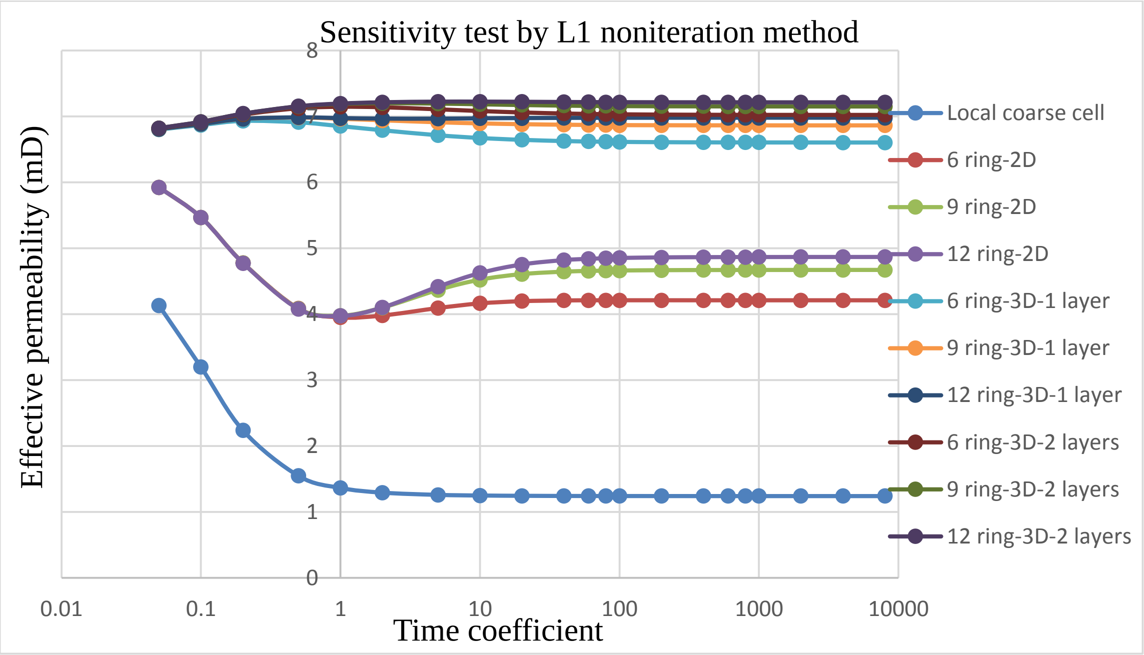

(d)

Figure 45 Continued

The four values of the averaged DTOF are shown in **Table 3**:

	L2-iteration	L1-iteration	L2-noniteration	L1-noniteration
averaged DTOF square (hour)	0.105	0.0398	1.20	0.544

Table 3: Diffuse source time (example 3)

In the sensitivity test result, each plot has ten curves. Each curve represents a different buffering region. Horizontally, we have three choices: 6 ring, 9 ring and 12 ring. Vertically, we also have three choices: no layer on the top and no layer at the bottom (2D), one layer on the top and one layer at the bottom (3D-1 layers) and two layers on the top and two layers at the bottom (3D-2 layers).

As we can see, when the diffuse source time is very small, the effective permeability given by L1-iteration method is stable with respect to the time coefficient. This is because the flow is concentrated in the high permeable cells at small diffuse source time. When the diffuse source time is large enough, from the sensitivity plots, we can see that the effective permeability starts to decline and the reason is due to the low permeable cells. The diffuse source in the low permeable cells becomes non-negligible and pulls down the effective permeability. In addition, we see that the effective permeability obtained from the local coarse cell is obviously smaller than the result obtained from the larger computational region. We see that the 3D result is different from the 2D result. The 3D result is the highest. According to the cell permeability and porosity in this example, the effective permeability obtained from the local coarse cell is too small. When the time coefficient is greater than 1, the 3D result is stable with respect to the time coefficient. As for the computational region sensitivity test, from this example, we see that we do not need a very large buffering region before the resulting effective permeability gets stable. Horizontally the buffering region needs only 6 extra rings and vertically it only needs one more layer on the top and one more layer at the bottom. In this example, the stable effective permeabilities given by the four methods are very close and it is hard to make decision on which method we may use.

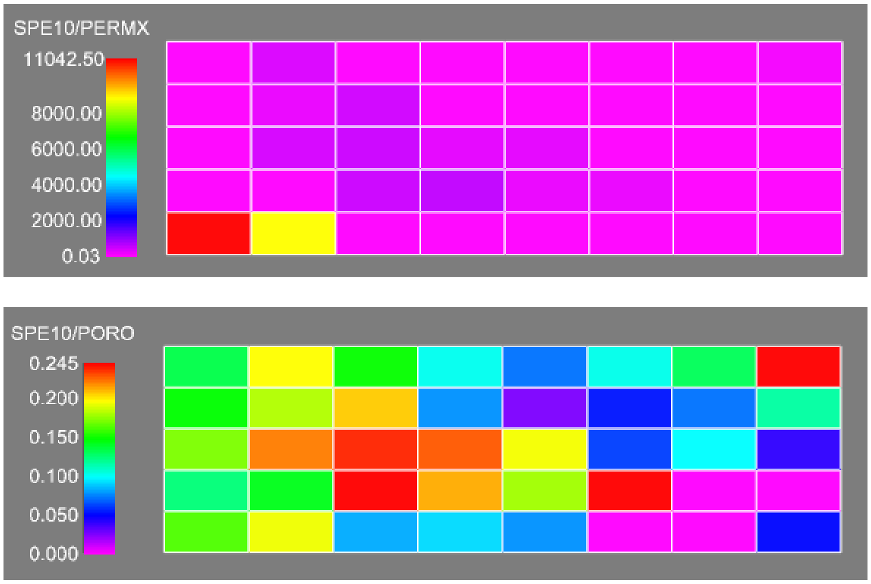

(a)

Figure 46: Permeability and porosity distribution (example 4). (a) top layer. (b) middle layer. (c) bottom layer.

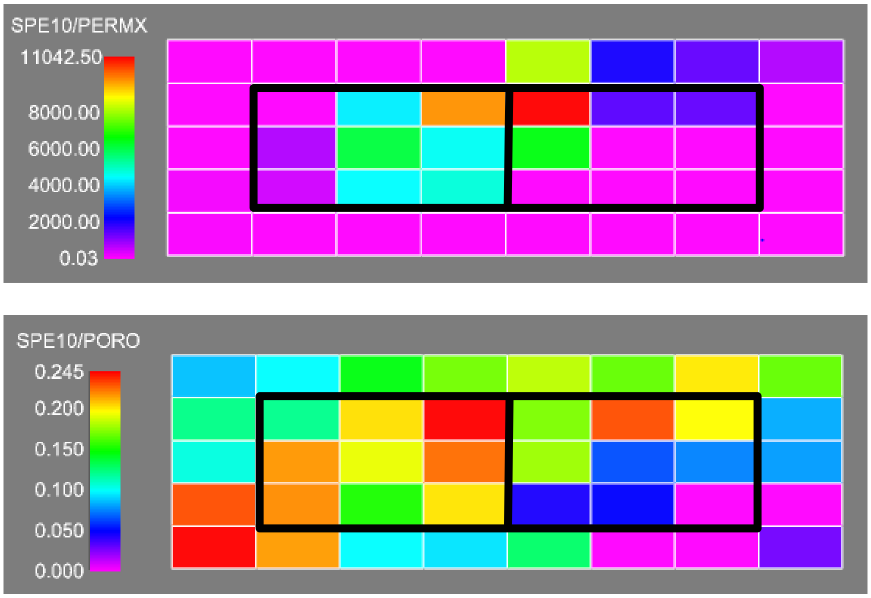

(b)

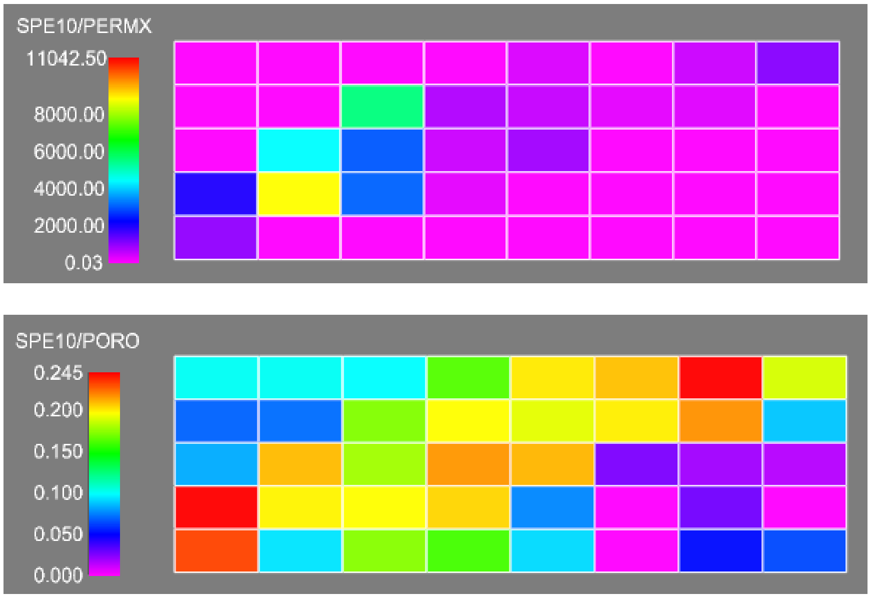

(c)

Figure 46 Continued

The fourth example has the permeability and porosity distribution as above. From **Figure 46**(b), we see that the two coarse cells cover the high permeable channel with some low permeable cells on two sides. Part of the buffering region is shown in the figures. Here is the time sensitivity and spatial sensitivity result for the fourth example:

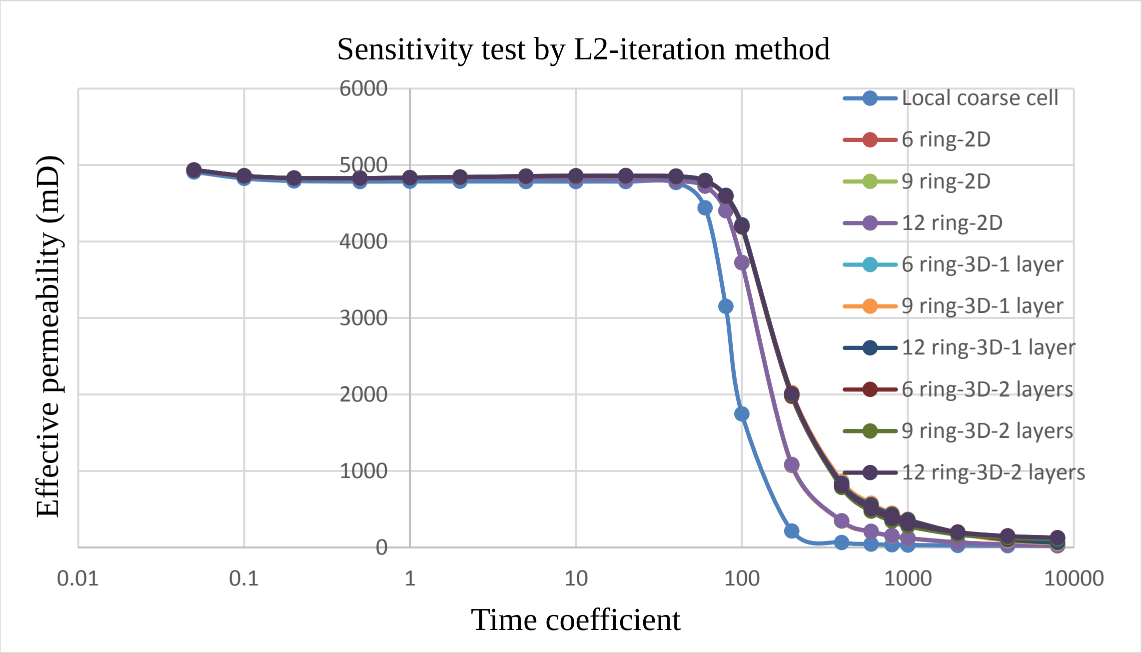

(a)

Figure 47: Sensitivity test result of the fourth example (a) L2-iteration method. (b) L1-iteration method. (c) L2-noniteration method. (d) L1-noniteration method.

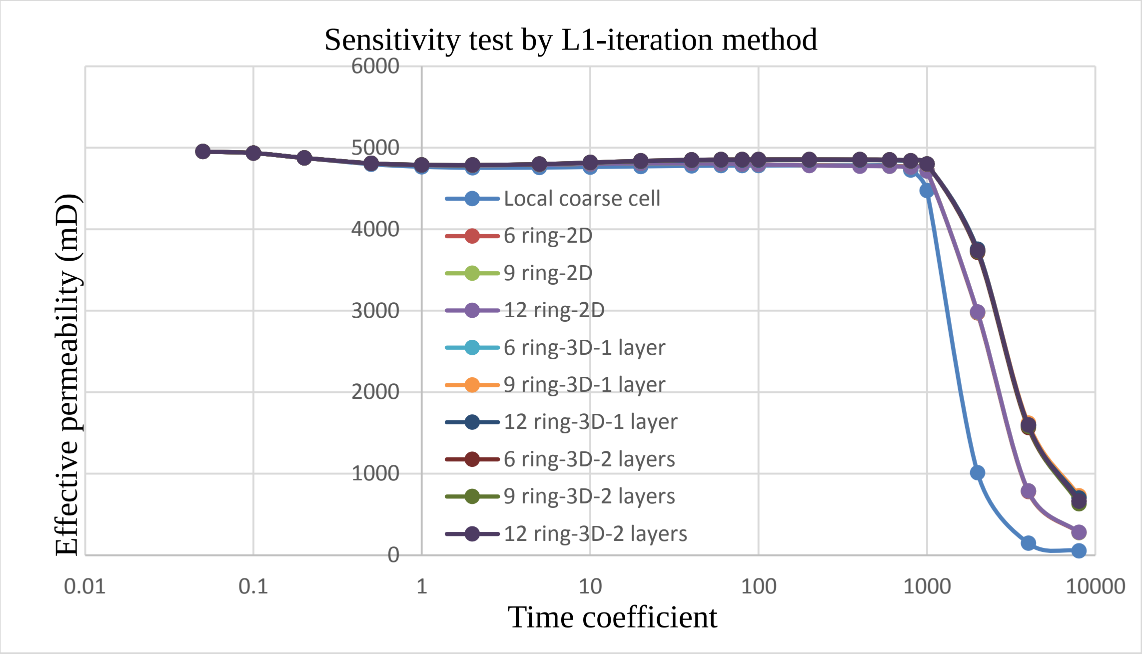

(b)

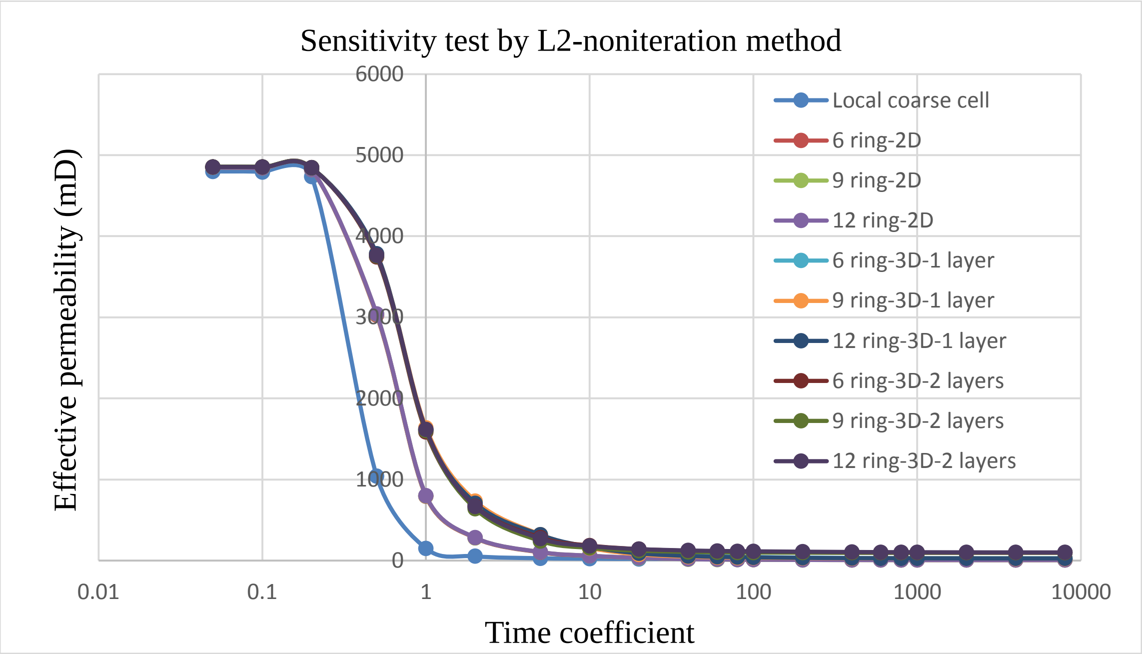

(c)

Figure 47 Continued

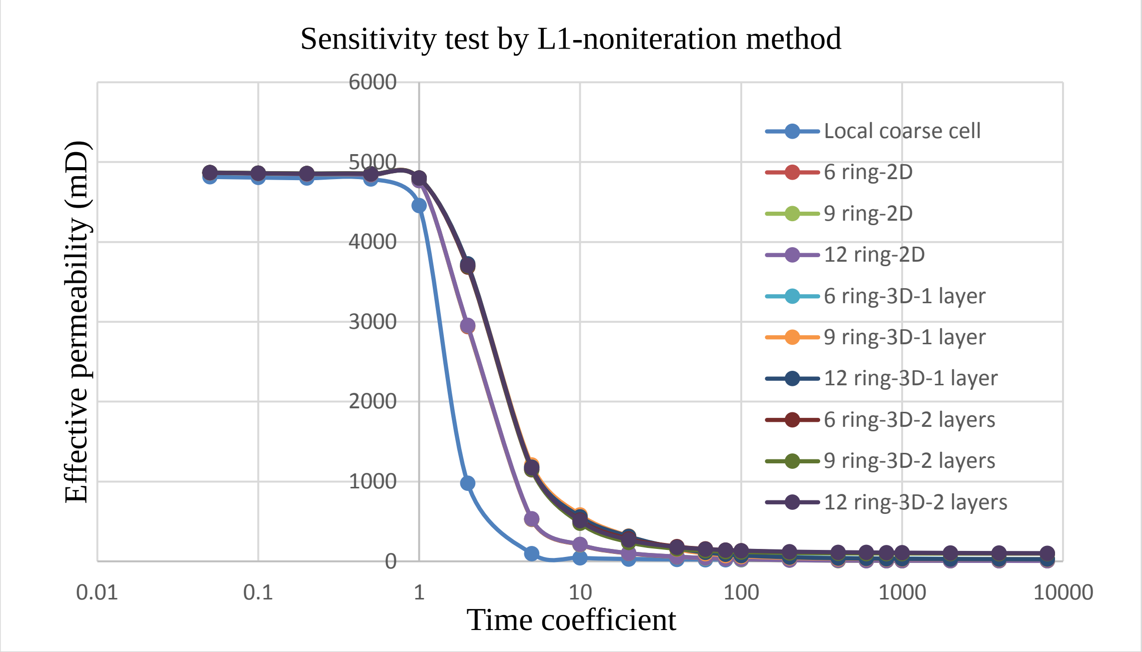

(d)

Figure 47 Continued

The coarse cell averaged DTOF calculated by the four methods is shown in **Table 4**:

	L2-iteration	L1-iteration	L2-noniteration	L1-noniteration
averaged DTOF square (hour)	2.80E-4	9.90E-5	6.86E-2	6.06E-3

Table 4: Diffuse source time (example 4)

In addition, we have three tables of the effective permeability result obtained using different buffering regions (**Table 5**).

	Effective permeability (mD)
L2 iteration	4786.205
L1 iteration	4765.2
L2 non-iteration	151.4532
L1 non-iteration	4455.8

(a)

	Effective permeability (mD)
L2 iteration	4834.8
L1 iteration	4789.5
L2 non-iteration	1618.4
L1 non-iteration	4800.1

(b)

	Effective permeability (mD)
L2 iteration	4834.8
L1 iteration	4789.5
L2 non-iteration	1618.4
L1 non-iteration	4800.1

(c)

Table 5: The effective permeability result (example 4). (a) local coarse cell only. (b) 6 ring-3D buffering region. (c) 9 ring-3D buffering region.

Similar to the third example, each sensitivity plot in this example has ten curves each of which stands for a different buffering region. From this example, we see that L2 non-iteration method gives the smallest effective permeability. L2 non-iteration method yields very small effective permeability when we use only the local coarse cell as the upscaling computational region. Therefore, this is another example which shows the upscaling based on the local coarse cell underestimates the inter-cell effective permeability.

In the spatial sensitivity test, according to the result, we see that the effective permeability gets stable when the buffering region horizontally has 6 extra rings and vertically has one more layer on the top and one more layer at the bottom.

Next, we discuss the time sensitivity result. In both L1 and L2 iteration method, we see a flat line at early time and the effective permeability at the time coefficient equal to 1 lies in this flat interval. As the time coefficient increases, we see that the effective permeability declines very fast. This decline is due to the low permeable cells. The weight of the diffuse source in the low permeable cells increases as the time coefficient increases. Therefore, when the time coefficient is big enough, the diffuse source allocated in the low permeable cells is non-negligible and those low permeable cells make contribution to the flux across the coarse cell interface. In L1 and L2 non-iteration method, we see that at the time coefficient equal to 1, the estimated effective permeability is located in the transition interval (L2 non-iteration) or at the starting point of the transition interval (L1 non-iteration). Therefore, the effective permeability calculated by the L1 and L2-noniteration methods is not very stable in the vicinity of the time coefficient 1.

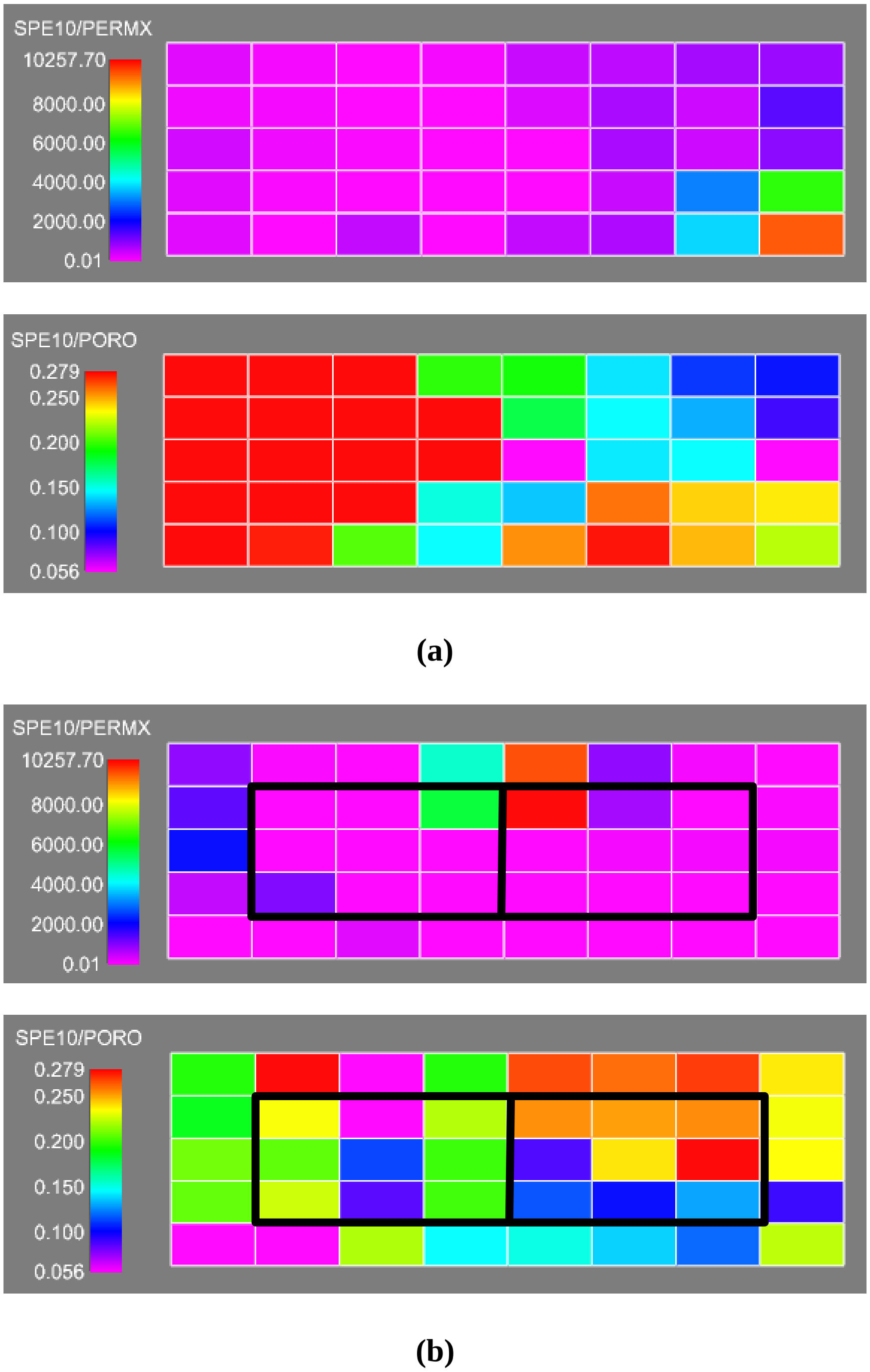

Figure 48: Permeability and porosity distribution (example 5). (a) top layer. (b) bottom layer.

The fifth example has the permeability and porosity distribution as above. The two coarse cells are in the bottom layer of the SPE10 model, so in this example there are only two layers shown in **Figure 48**. The two coarse cells only have a few cells that have very high permeability. The rest of the cells all have very low permeability compared to the high permeable cells. Here only part of the buffering region is shown in the figures. This is an example of upscaling for the high contrast cells. Here is the time sensitivity result and spatial sensitivity result for the fifth example:

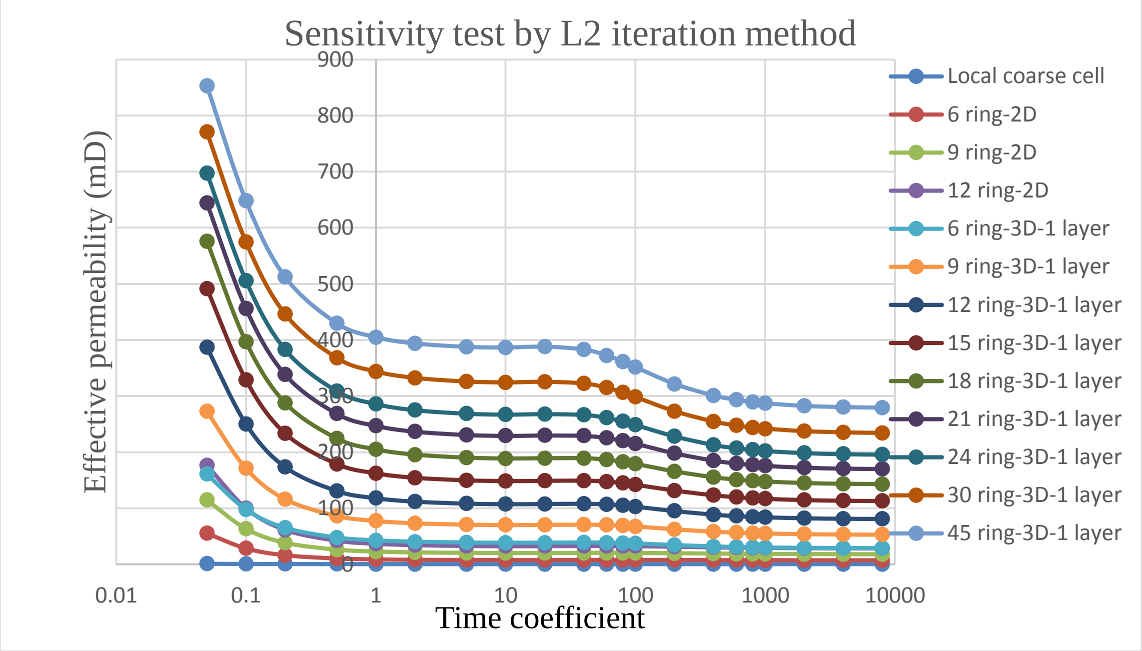

(a)

Figure 49: Sensitivity test result of the fifth example (a) L2-iteration method. (b) L1-iteration method. (c) L2-noniteration method. (d) L1-noniteration method

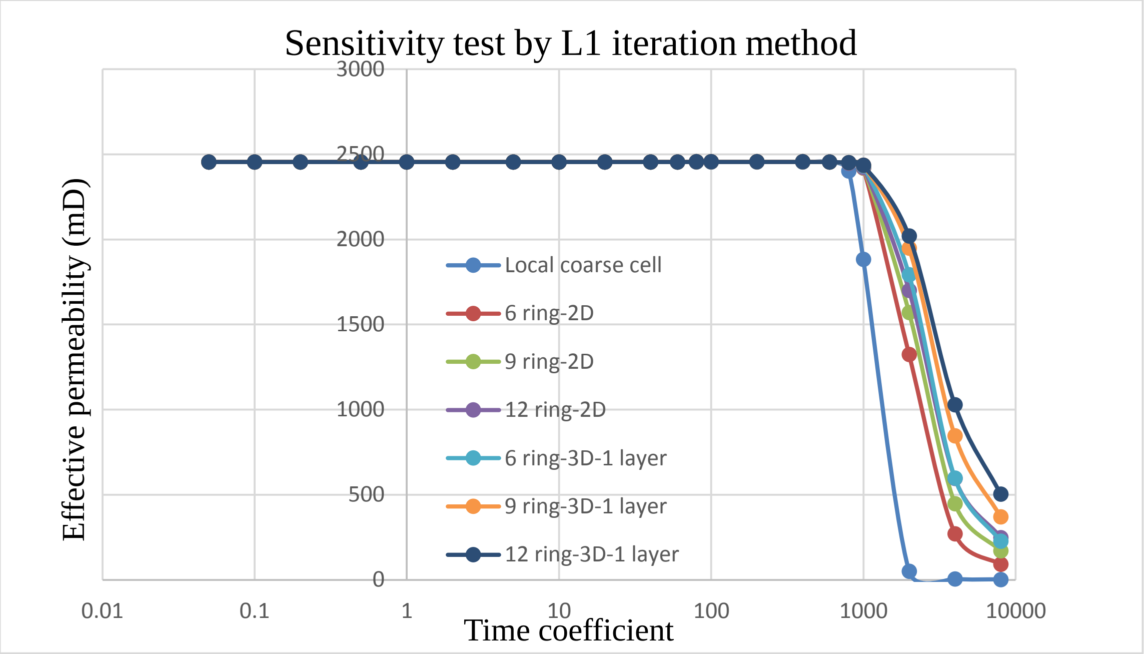

(b)

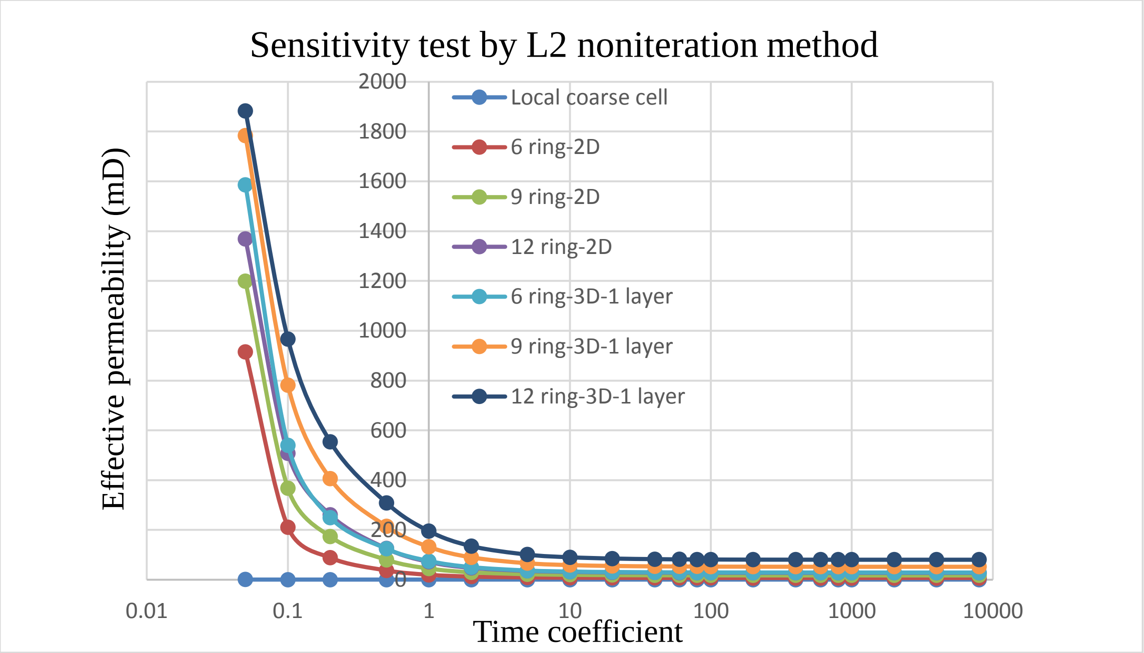

(c)

Figure 49 Continued

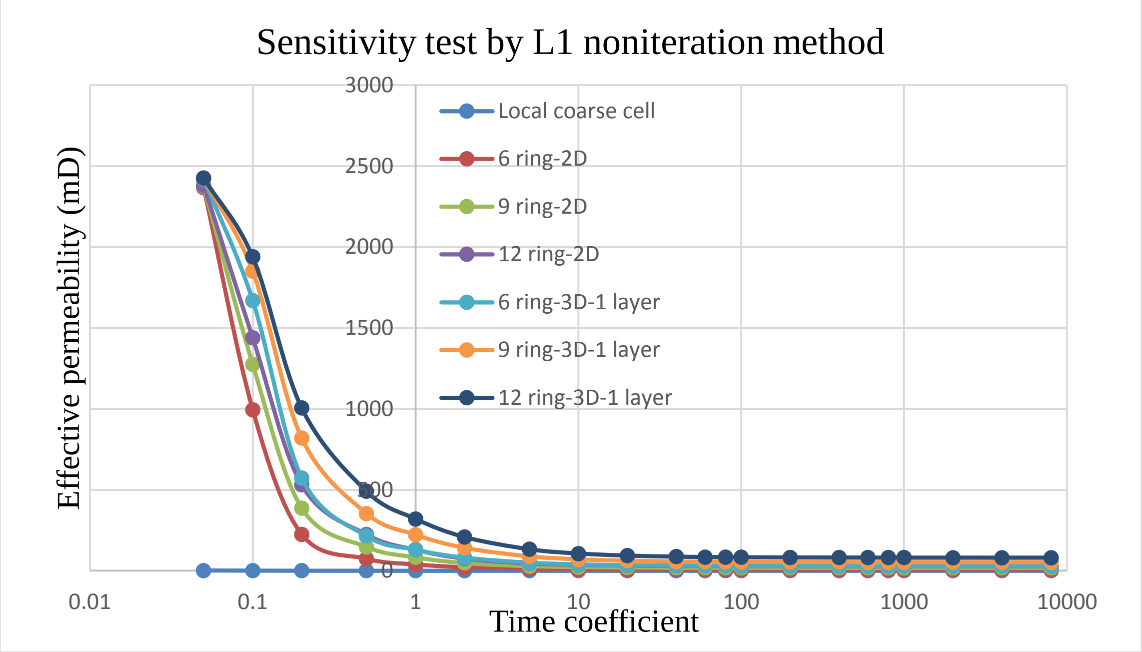

(d)

Figure 49 Continued

The coarse cell averaged DTOF calculated by the four methods is shown in **Table 8**:

	L2-iteration	L1-iteration	L2-noniteration	L1-noniteration
averaged DTOF square (hour)	2.71E-4	8.34E-5	8.34	2.85

Table 6: Diffuse source time (example 5)

Similar to Example 4, here we have three tables which are the effective permeability result obtained by using different buffering regions (**Table 7**).

	Effective permeability (mD)
L2 iteration	0.3178
L1 iteration	2455.8
L2 non-iteration	0.3342
L1 non-iteration	0.326

(a)

	Effective permeability (mD)
L2 iteration	42.5293
L1 iteration	2455.8
L2 non-iteration	74.8
L1 non-iteration	128.6

(b)

	Effective permeability (mD)
L2 iteration	77.381
L1 iteration	2455.8
L2 non-iteration	132.5
L1 non-iteration	222.1

(c)

Table 7: The effective permeability result (example 5). (a) local coarse cell only. (b) 6 ring-3D buffering region. (c) 9 ring-3D buffering region.

This is a tough example. Three methods (L2 iteration, L2-noniteration & L1-noniteration) give very large diffuse source time for the left coarse cell. The consequence of the large diffuse source time is that the computational region needs to be very large before we get the stable effective permeability result. Therefore, in this example it is difficult to do the spatial stability analysis if we use L2 iteration method, L2-noniteration method and L1-noniteration method. Similar to the previous examples, when the left coarse cell diffuse source time is very large, the diffuse source allocated to the low permeable cells will be non-negligible and therefore, the low permeable cells will make contribution to the total flux at the coarse cell face. However, in reality, according to the cell permeability distribution in this local area, the main flow should be concentrated in those high permeable cells. In L1-iteration method, the coarse cell diffuse source time is very small. Therefore, in the sensitivity test by L1-iteration method, we see that the effective permeability gets stable very fast as the size of the computational region increases. In addition, the effective permeability is also very stable with respect to the time coefficient in the sensitivity test by L1-iteration method.

2.3.5.3 Discussion

In this section, we have studied the time sensitivity and spatial sensitivity of the effective permeability in the local diffuse source upscaling. Five examples from the SPE10 model are used for this study. These five examples can be divided into two groups. The first two examples form a group and the last three examples form another group.

The local coarse cells in the first two examples are not high contrasted cells. The averaged DTOF results obtained from different methods have small variation. According to the sensitivity test result, we see that spatially the computational region does not need to be very large before the stabilization of the effective permeability result. Horizontally the 6 ring buffering region is enough and vertically we do not need extra layers. Therefore, a 6 ring-2D buffering region is enough for the first two examples. As for the time sensitivity test, in the first two examples, the effective permeability is stable at the diffuse source time calculated by each method. The effective permeabilities from the four methods are very close to each other in the first two examples. This makes it very hard to decide which method we should use to calculate the diffuse source time for the coarse cell.

In the last three examples, the coarse cells have high contrasted permeability and the resulting averaged DTOF calculated from the four equations has a strong variation. In addition, from Example 3 we see that we can have different effective permeability results which depends on whether we include the vertical connection in upscaling. This leads us to do some more stability analysis for these high contrasted coarse cells. In the last three examples, two 3D effective permeability results are compared. One result is based on the 3D-1 layer upscaling region and the other result is based on the 3D-2 layers upscaling region. We find that one extra layer on each side of the coarse cells vertically is already enough for Example 3 and Example 4. Example 5 is a tough example. In Example 5, L2-iteration method, L2-noniteration method and L1-noniteration method give very large averaged DTOF for the coarse cells, which challenges the spatial sensitivity test. The L1-

iteration method gives very small averaged DTOF for Example 5 and we see the stability of the effective permeability with respect to the diffuse source time and the computational region in the sensitivity test by L1-iteration method. However, it is still hard to decide which method we may use to calculate the coarse cell diffuse source time.

In conclusion, from the sensitivity test we learned that the variation of the averaged DTOF given by the four equations depends on the permeability heterogeneity in the upscaling region. The occurrence of high contrast permeability cell leads to a strong variant averaged DTOF results from different methods. L2-noniteration method yields the largest averaged DTOF and L1-iteration method yields the smallest averaged DTOF. If the permeability field in the upscaling region is not that high contrasted, we can choose any of the four methods to calculate the coarse cell diffuse source time. Secondly, we learned that the effective permeability results depend on where we put the boundary for the upscaling computational region. As the diffuse source time is fixed, we see that the effective permeability results will get stabilized as the upscaling computational region expands. However, since the boundary of the upscaling computational region is determined according to the exponential term in the diffuse source, then the heterogeneity of the permeability field can affect the boundary of the upscaling computational region. If the permeability heterogeneity is very strong, we may need a very large computational region to get the stable effective permeability results. Therefore, the upscaling for very high contrast coarse cells, e.g., Example 5, is a challenging and needs more investigation or new upscaling methods.

2.4 Summary

To conclude this chapter, here I will summarize the diffuse source upscaling algorithm:

Step 1: we have two adjacent coarse cells. Start from the common coarse cell face with the DTOF $\tau = 0$ and find out the DTOF for all the fine cells in each coarse cell.

Step 2: after knowing the diffusive time of flight for all the fine cells in each coarse cell, we calculate the coarse cell diffuse source time. As for which method we use for the calculation of the diffuse source time, I have claimed that we can use any of the four methods from the last section to calculate the coarse cell diffuse source time as long as the two upscaling coarse cells are not very high contrasted. The four methods yield very close result. The upscaling for very high contrast coarse cells is a challenging and needs more investigation or new upscaling methods.

Step 3: in every local upscaling, we set the computational region to be a region that is larger than the region occupied by the two adjacent coarse cells. As for how large the computational region is, according to the result from the last section, this computational region does not need to be very large except when the coarse cells are extremely high contrasted. With the prescribed computational region, find out the DTOF for all the fine cells in this prescribed computational region so that we can allocate the diffuse source to each fine cell.

Step 4: after the allocation of the fine cell diffuse source, we build the pressure equations according to the mass conservation.

Step 5: solve the pressure equations and use only the cell pressure that is right at the coarse cell interface to determine the effective face permeability.

Step 6: with the effective face permeability, we calculate the steady state inter-cell transmissibility that is used in the simulator.

CHAPTER III

TESTING THE DEVELOPMENTS

In this chapter, we will test the DS upscaling algorithm using the SPE10 model. The SPE10 data set will be studied under both primary and secondary recovery. However, we will restrict our current work to “oil injection” to allow us to study pressure and rate upscaling without needing to address multiphase flow issues.

3.1 3x3x1 upscaling

3x3x1 upscaling is conducted on the SPE10 model. In this upscaling, I only did the areal coarsening and the upgridding is not used for the SPE10 model because of the high discontinuity of the permeability in the vertical direction. The upgridding in vertical direction increases the difficulty in the estimation for the local inter-cell permeability. In this work, I studied both primary and secondary recovery. In primary recovery, four vertical production wells are drilled at the four corners of the model and are subject to constant bottomhole pressure. In secondary recovery, two experiments were carried out. In the first experiment, I use one vertical production well and one vertical injection well in which the oil is injected at a voidage replacement ratio equal to 1. Wells have a target flow rate subject to the bottomhole pressure constraint. In the second experiment, the model has one vertical injection well and four vertical production wells. The production wells are located at the four corners of the model and the injection well is located at the center of the model. The bottomhole flowing pressure in the production wells is fixed and the injection well has a target flow rate subject to the bottomhole pressure constraint.

Here is the primary recovery result. In **Figure 50** below, the green cross marker line in each figure is the reference cumulative production result based on the fine scale model. The red solid curve in **Figure 50**(a) is the result from the upscaled model generated by the diffuse source upscaling. The coarse cell diffuse source time is determined by L2-noniteration method and the local upscaling computational domain is a 6 ring-3D-1 layer domain. The red curve in **Figure 50**(b) is the permeability upscaling result and the red curve in **Figure 50**(c) is the result from the flow based plane source upscaling. We can see that all the primary recovery curves show very small variation between different cases.

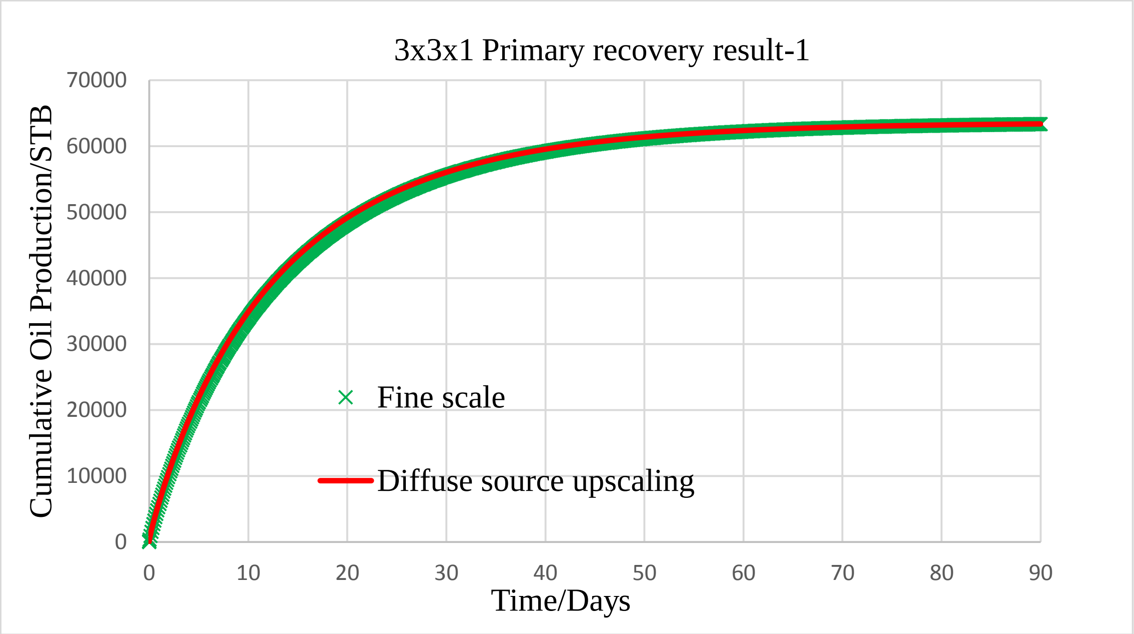

(a)

Figure 50: 3x3x1 Primary recovery result. (a) diffuse source upscaling. (b) permeability upscaling. (c) plane source upscaling.

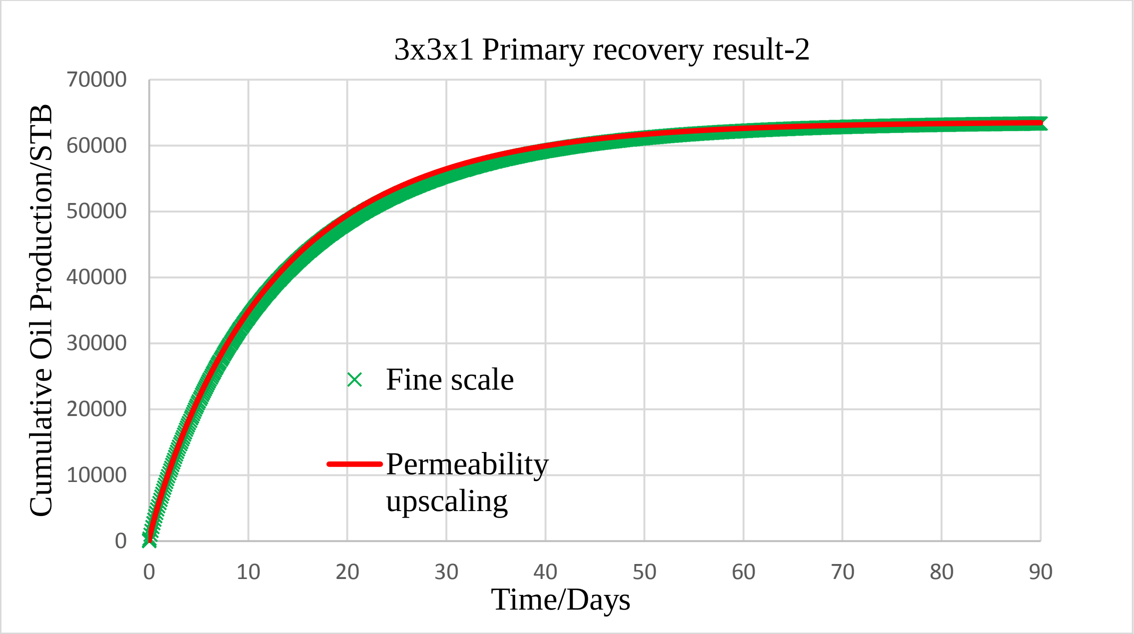

(b)

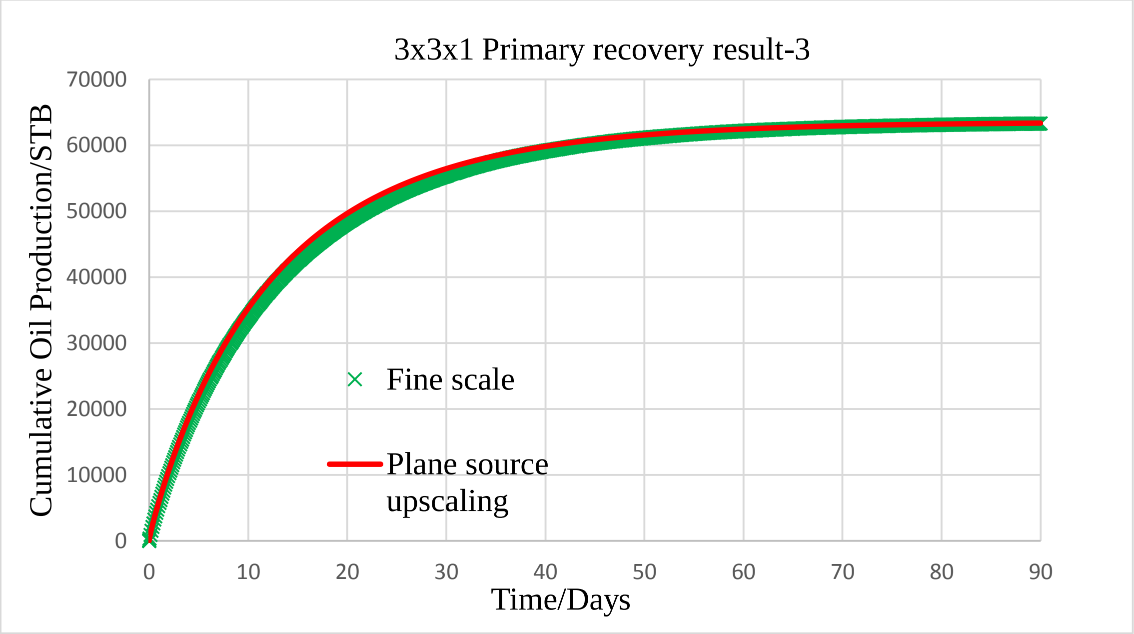

(c)

Figure 50 Continued

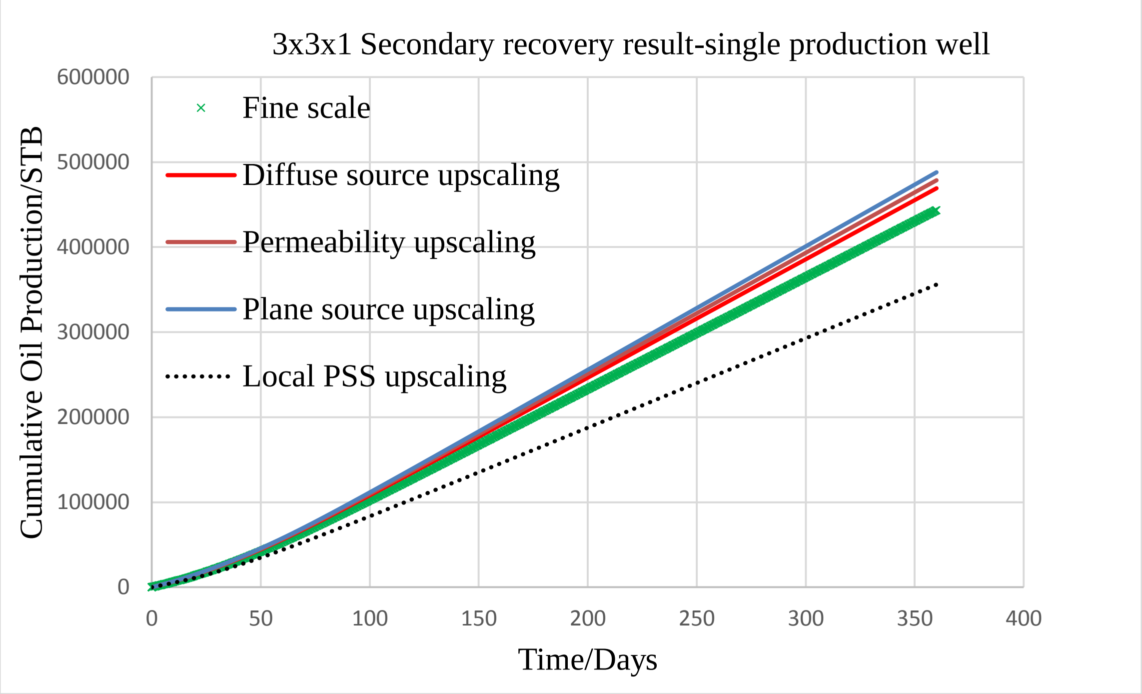

Figure 51: 3x3x1 Secondary recovery result (single injection well and single production well)

In the 3x3x1 secondary recovery, **Figure 51** shows the result for the first experiment. In **Figure 51**, the green cross marker line is the fine scale result; the red curve is the result from the diffuse source upscaling. Similarly, the coarse cell diffuse source time is calculated by L2-noniteration method and the local upscaling computational domain is a 6 ring-3D-1 layer domain. The blue curve in **Figure 51** is the plane source upscaling result and the dark red curve is the result obtained from the permeability upscaling. The previous result based on the local PSS upscaling (black dot line) is also shown in this figure for comparison. From this figure, we can see the result based on the diffuse source upscaling is better than the result obtained from the local PSS upscaling. In addition, the diffuse source upscaling, plane source upscaling and permeability upscaling all generate the results which are above the fine scale result, but this cumulative production difference is small and acceptable.

In the second experiment of the secondary recovery, multiple production wells are used. According to the production result from each production well, we can check the quality of the upscaled model and see if the internal flow is drastically distorted from the fine scale model after upscaling. In the following two figures, I will show the result of the total cumulative production (**Figure 52**) and the production from every single well (**Figure 53**).

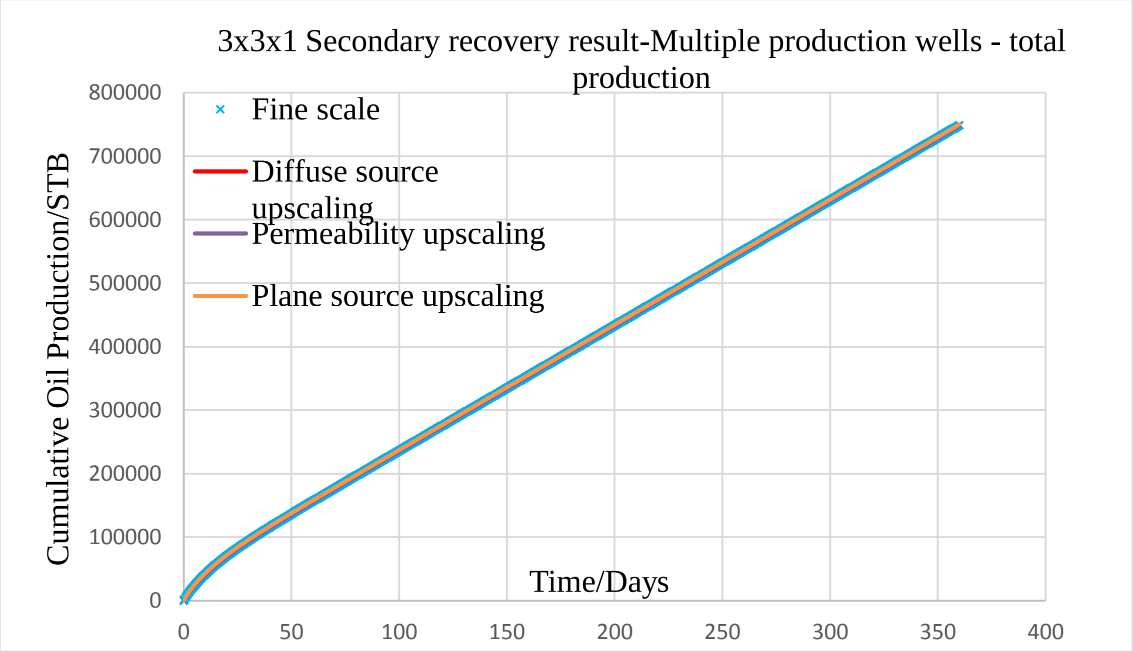

Figure 52: 3x3x1 Secondary recovery result (multiple production wells)-total production

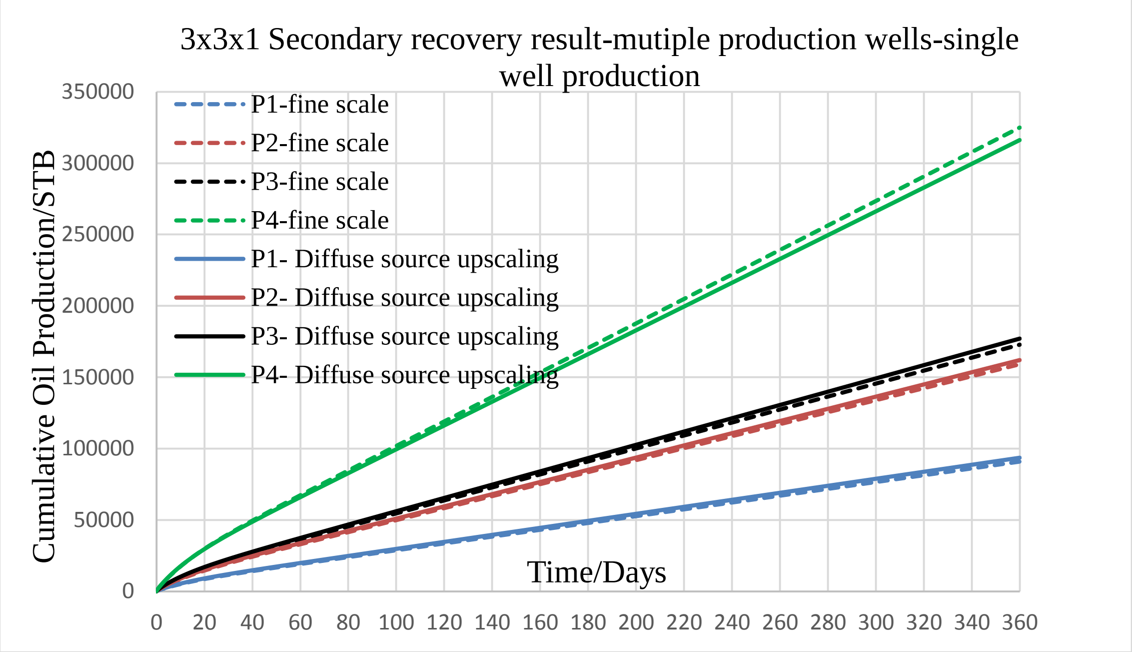

Figure 53: 3x3x1 Secondary recovery result (multiple production wells)-single well production

In **Figure 52**, the blue cross marker line represents the fine scale result; the red curve is the result produced by diffuse source upscaling. The coarse cell diffuse source time is calculated by L2-noniteration method and the local computational region is a 6 ring-3D-1 layer domain. The yellow curve is the result from plane source upscaling and the purple curve is the result from flow based permeability upscaling. We can see the three results all have a good match with the fine scale result.

In **Figure 53**, the four production wells are labelled by the letters “P1”, “P2”, “P3” and “P4”. We can see the oil production from the four production wells. The dash lines represent the fine scale result and the solid lines represent the result from diffuse source upscaling. As we can see, in every production well, the result based on the upscaled model is very close to the fine scale result.

In conclusion, from the primary recovery result and the two secondary recovery result, we can see that the diffuse source upscaling can produce very good results for the SPE10 model. The diffuse source upscaling works well as the other two upscaling methods do.

3.2 Upscaling diagnosis

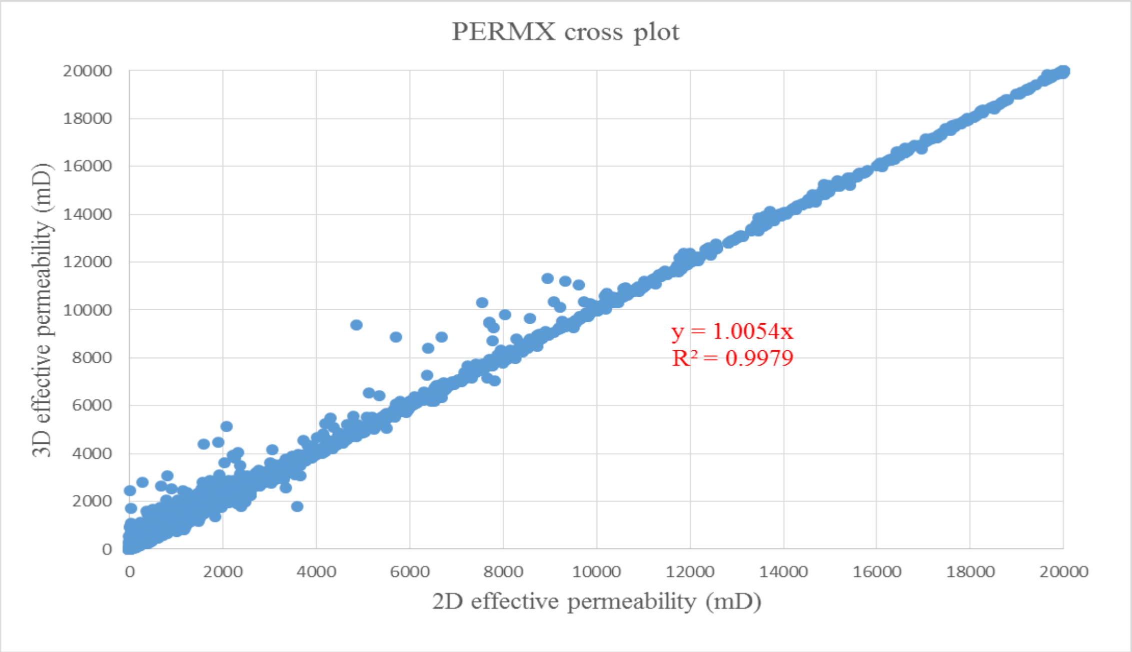

(a)

Figure 54: Permeability cross plot (global). (a) PERMX. (b) PERMY. (c) PERMZ

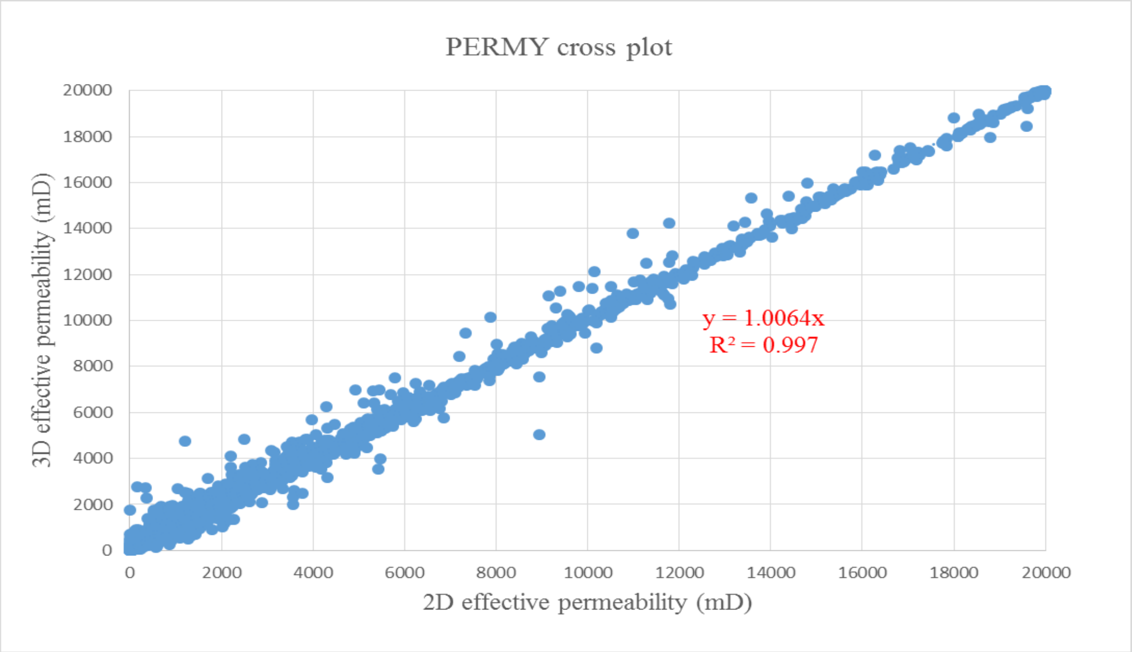

(b)

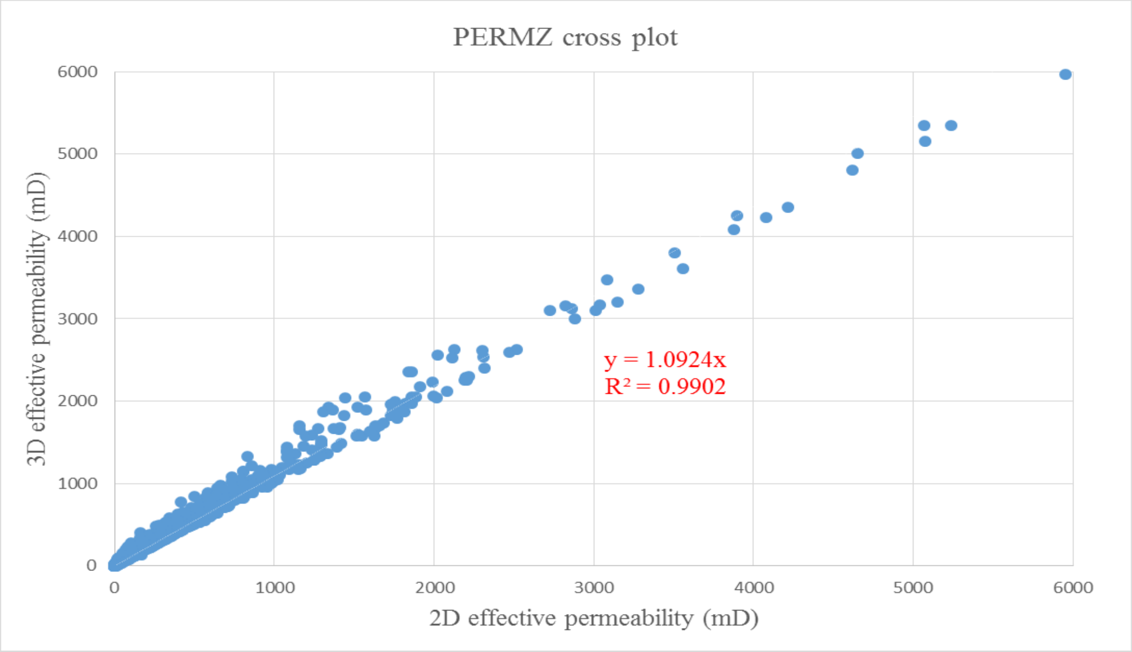

(c)

Figure 54 Continued

In the last chapter, in the sensitivity experiment I have shown that the 2D effective permeability is very close to the 3D effective permeability when the coarse cells are not very high contrasted. To support this statement, next I will show the permeability cross plots in three directions obtained from the entire model.

In the three permeability cross plots above, the horizontal axis represents the 2D effective permeability and the vertical axis represents the 3D effective permeability. Globally, we can see that most of the dots lie around a unit slope line. However, if we compare the three plots in **Figure 54**, we find that the slope of the linear trendline in PERMZ cross plot is not that close to the unit slope when compared to the other two plots. In addition, when we focus on the local region at the lower left corner of each plot in **Figure 54**, we will find many dots lie above the unit slope line (**Figure 55**). The smaller the permeability is, the larger the discrepancy is. Therefore, we need more investigation in the future on the upscaling in the low permeable zone.

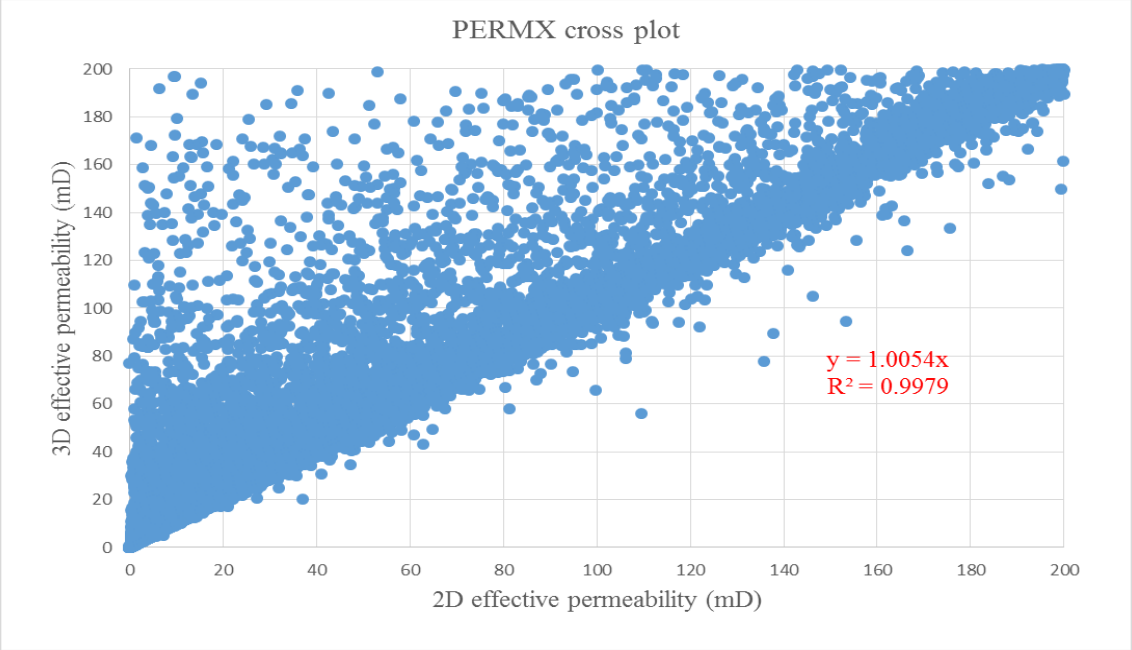

(a)

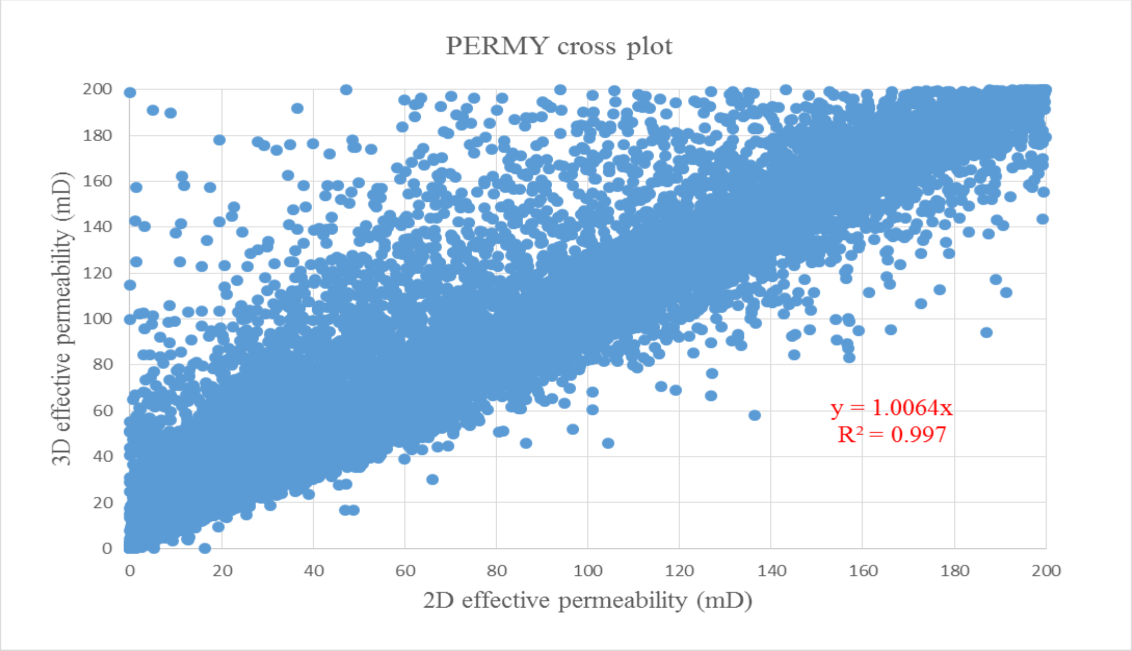

(b)

Figure 55: Permeability cross plot (local). (a) PERMX. (b) PERMY. (c) PERMZ.

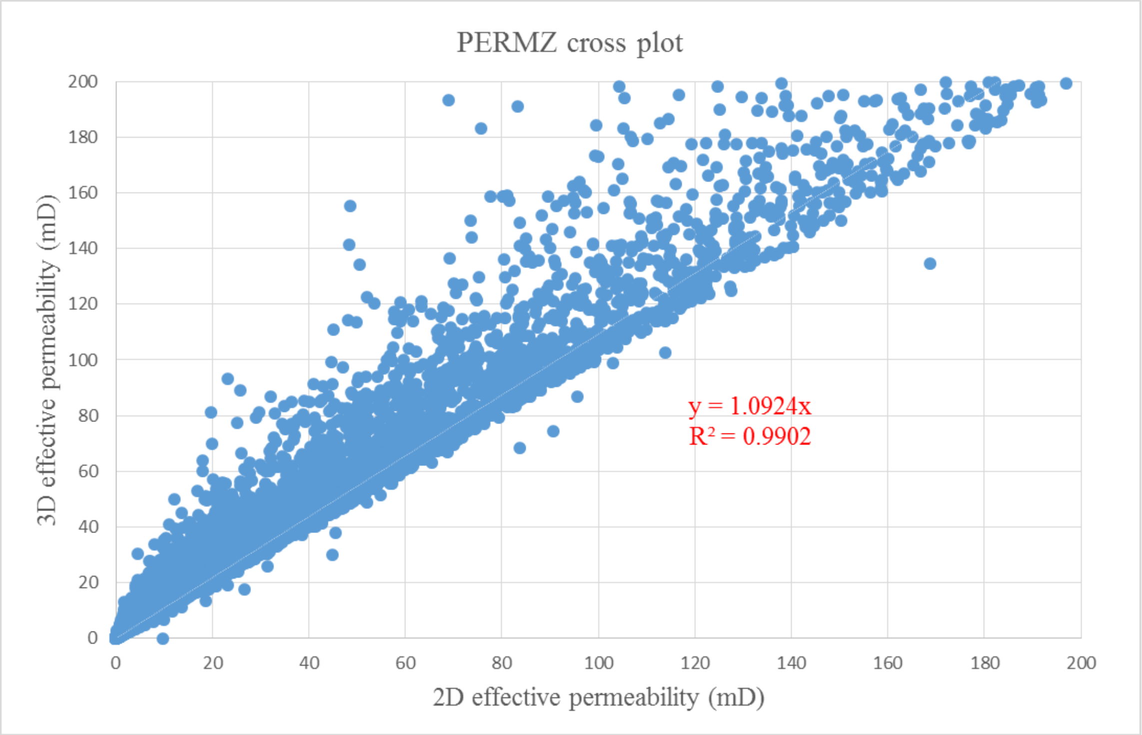

(c)

Figure 55 Continued

Also, I compare the cumulative oil production result using 2D effective permeability and 3D effective permeability. The result is shown in **Figure 56** below.

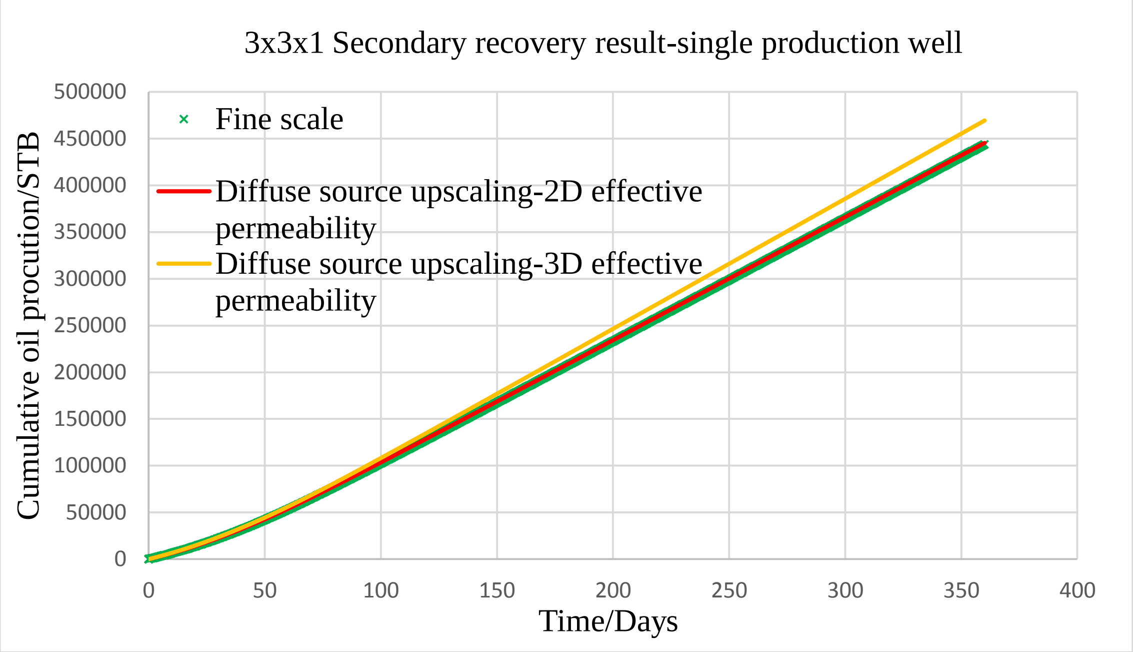

Figure 56: The comparison between 2D and 3D diffuse source upscaling

In **Figure 56**, the green cross marker line is the fine scale result; the red curve is the result from 2D effective permeability; the yellow curve is the result from 3D effective permeability. From **Figure 56**, we see that the difference between the 2D result and 3D result is not very large and the reason for this difference is due to the uncertainty of the upscaling for high contrast coarse cells.

In the last chapter, I also claimed that the four time calculation methods should all work for the diffuse source upscaling as long as the coarse cells are not very high contrasted and the four methods should generate similar effective permeability when the coarse cells are more homogeneous. To support this statement, here I compare the cumulative production results from these four methods, **Figure 57**.

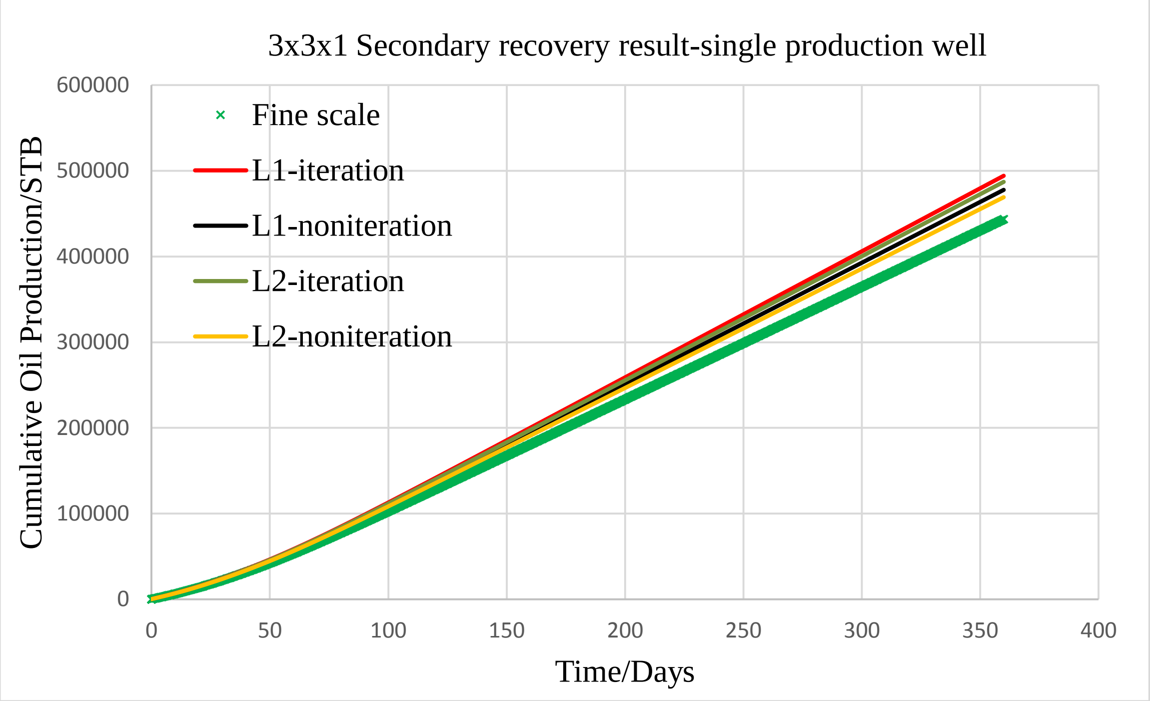

Figure 57: Secondary recovery result from four different time calculation methods

In **Figure 57**, the red line represents the result from L1-iteration method; the black line represents the result from L1-noniteration method; the dark green line represents the result from L2-iteration method; the dark yellow line represents the result from L2-noniteration method. As we can see, these four results are very close, supporting the conclusion in the last chapter.

3.3 Conclusion

In this chapter, using the improved diffuse source upscaling algorithm, I upscaled the SPE10 model. The cumulative oil production based on the upscaled model is close to the results obtained from the fine scale model. In addition, I did some statistical analysis on the effective permeability results from the entire model. The permeability cross-plot shows that in most cases the 2D effective permeability result is close to the 3D effective permeability result. This conclusion is also supported by the simulation results which are based on these two sets of effective permeability. Lastly, I did another experiment to compare the four different time calculation methods. The simulation results are close, which support the conclusion made in the last chapter.

CHAPTER IV

SUMMARY AND CONCLUSIONS

In this work, I had a detailed study on the diffuse source upscaling algorithm which was first introduced for the upscaling of tight gas geological model (Nunna et al. 2015). First, I revisited the effective transmissibility equation which was used in the old algorithm and found that it cannot give us the correct effective transmissibility in the simplest homogeneous model. This observation pushes us to calculate the effective face permeability in the local DS upscaling. The effective face permeability is calculated by using the fine cell pressure immediately adjacent to the coarse cell common flux face and it turns out that we can have the correct upscaled effective transmissibility for the homogeneous model when using the effective face permeability generated from the improved DS upscaling.

The second part of this work is related to the boundary condition for the local upscaling. The DS upscaling algorithm was completely local calculation and the external boundaries of the upscaling region were completely sealed. In this work, I find the simulation result based on the upscaled SPE10 model has a large discrepancy with the fine scale result when I still use the no flow boundary condition in the local upscaling. Therefore, I studied the boundary effect on the local upscaling and had the upscaling computational region extended by including the neighboring cells into every local upscaling. The spatial sensitivity test is also conducted to assist us in defining the upscaling computational region.

The third part of this work is focused on the diffuse source time which is required in defining the transient state diffuse source. I proposed four equations for the calculation of the diffuse source time. To compare these four equations, I did the time sensitivity to see which equation can generate the stable effective face permeability. The time sensitivity test and the spatial sensitivity test were both done at the same time because the value of diffuse source time can affect the specification of the upscaling computational region. It turned out that the effective face permeability results generated by these four equations are close when the fine cells in the upscaling region do not have very high contrast permeabilities. Therefore, it is hard to say which equation is better than the others and finally I selected one non-iterative equation only for the sake of simplicity. The upscaling for the high contrast coarse cells is still a challenging and needs more investigation in the future. Also, in the spatial sensitivity test, it was found that in SPE10 model we need to extend the computational region from the local coarse cell region to a larger region that includes additional 28 coarse cells around the upscaling region.

To test all the developments, the simulation was performed on SPE10 model. The results based on the upscaled model have a good match with the fine scale results in both -primary recovery test and secondary recovery test.

REFERENCES

Aarnes, J.E. 2004. On the Use of a Mixed Multiscale Finite Element Method for Greater Flexibility and Increased Speed or Improved Accuracy in Reservoir Simulation. *Multiscale Modelling and Simulation,* **2** (3): 421-439.

Ambegaokar, V., Halperin, B.I., and Langer, J.S. 1971. Hopping Conductivity in Disordered Systems. *Physical Review B,* **4** (8): 2612-2620.

Arbogast, T. 2002. Implementation of a Locally Conservative Numerical Subgrid Upscaling Scheme for Two-Phase Darcy Flow. *Computational Geosciences,* **6**, 453-481.

Arbogast, T. and Bryant, S.L. 2002. A Two-Scale Numerical Subgrid Technique for Waterflood Simulations. *SPE Journal*, **7** (4): 446-457. Society of Petroleum Engineers. DOI: http://dx.doi.org/10.2118/81909-PA.

Babuska, I., Caloz, G. and Osborn, J.E. 1994. Special Finite Element Methods for a Class of Second Order Elliptic Problems with Rough Coefficients. *SIAM Journal on Numerical Analysis,* **31** (4): 945-981.

Barker, J.W. and Thibeau, S. 1997. A Critical Review of the Use of Pseudorelative Permeabilities for Upscaling. *SPE Reservoir Engineering*, **12** (02): 138-143. Society of Petroleum Engineers. DOI: http://dx.doi.org/10.2118/35491-PA.

Begg, S.H., Carter, R.R., and Dranfield, P. 1989. Assigning Effective Values to Simulator Gridblock Parameters for Heterogeneous Reservoirs. *SPE Reservoir Engineering,* **4** (04): 455-463. Society of Petroleum Engineers. DOI: http://dx.doi.org/10.2118/16754-PA.

Chen, Y., Durlofsky, L.J., Gerritsen, M. et al. 2003. A Coupled Local-Global Upscaling Approach for Simulating Flow in Highly Heterogeneous Formations. *Advances in Water Resources*, **26** (10): 1041-1060. DOI: http://dx.doi.org/10.1016/S0309-1708(03)00101-5

Chen, Z. and Hou, T. 2003. A Mixed Multiscale Finite Element Method for Elliptic Problems with Oscillating Coefficients. *Mathematics of Computation*, **72** (242): 541-576.

Christie, M. 1996. Upscaling for Reservoir Simulation. *Journal of Petroleum Technology*, **48** (11): 1004-1010. Society of Petroleum Engineers. DOI: http://dx.doi.org/10.2118/37324-PT.

Dagan, G. 1979. Models of Groundwater Flow in Statistically Homogeneous Porous Formations. *Water Resource Research*, **15** (1): 47-63.

Darman, N.H., Pickup, G.E., and Sorbie, K.S. 2002. A Comparison of Two-Phase Dynamic Upscaling Methods Based on Fluid Potentials. *Computational Geosciences,* **6** (1): 5-27.

Dijkstra, E. 1959. A Note on Two Problems in Connexion with Graphs. *Numerische Mathematik*, **1**: 269-271.

Du, S. 2012. Multiscale Reservoir Simulation: Layer Design, Full Field Pseudoization and Near Well Modeling, Doctoral dissertation, Texas A&M University. Available electronically from http://hdl.handle.net/1969.1/148248

Durlofsky, L.J. 2005. Upscaling and Gridding of Fine Scale Geological Models for Flow Simulation. In 8th International Forum on Reservoir Simulation Iles Borromees, Stresa, Italy: 20-24.

Durlofsky, L.J., Milliken, W.J., and Bernath, A. 2000. Scale Up in the Near-Well Region. *SPE Journal*, **5** (01): 110-117. Society of Petroleum Engineers. DOI: http://dx.doi.org/10.2118/61855-PA.

Efendiev, Y. 1999. The Multiscale Finite Element Method (MsFEM) and Its Applications. Dissertation (Ph.D.), California Institute of Technology. http://resolver.caltech.edu/CaltechETD:etd-11102005-090314

Efendiev, Y., Hou, T. and Wu, X. 2000. Convergence of a Nonconformal Multiscale Finite Element Method. *SIAM Journal on Numerical Analysis*, **37**: 888-910.

Farmer, C.L. 2002. Upscaling: A Review. *International Journal for Numerical Methods in Fluids*, **40** (1-2): 63-78. DOI: 10.1002/fld.267.

Fayers, F.J. and Hewett, T.A. 1992. A Review of Current Trends in Petroleum Reservoir Description and Assessment of the Impacts on Oil Recovery. *Advances in Water Resources*, **15** (6): 341-365.

Fujita, Y., Datta-Gupta, A. and King, M.J. 2015. A Comprehensive Reservoir Simulator for Unconventional Reservoirs Based on the Fast Marching Method and Diffusive Time of Flight. Society of Petroleum Engineers. DOI: http://dx.doi.org/10.2118/173269-MS.

Gerritsen, M.G. and Durlofsky, L.J. 2005. Modeling Fluid Flow in Oil Reservoirs. *Annual Review of Fluid Mechanics*, **37**: 211-238. DOI: 10.1146/annurev.fluid.37.061903.175748

Gomez-Hernandez, J.J. and Journel, A.G. 1994. Stochastic Characterization of Gridblock Permeabilities. *SPE Formation Evaluation*, **9** (02): 93-99. Society of Petroleum Engineers. DOI: http://dx.doi.org/10.2118/22187-PA.

Hales, H.B. 1983. Parameterization of Match-Derived Pseudo-Relative Permeabilities. Society of Petroleum Engineers. DOI: http://dx.doi.org/10.2118/11494-MS.

Holden, L. and Nielsen, B. F. 2000. Global Upscaling of Permeability in Heterogeneous Reservoirs; The Output Least Squares (OLS) Method. *Transport in Porous Media*, **40** (2): 115-143. DOI: 10.1023/a: 1006657515753

Hosseini, S.A. and Kelkar, M. 2010. Analytical Upgridding Method to Preserve Dynamic Flow Behavior. *SPE Reservoir Evaluation & Engineering*, **13** (03): 473-484. Society of Petroleum Engineers. DOI: http://dx.doi.org/10.2118/116113-PA.

Hou, T.Y. and Wu, X.H. 1997. A Multiscale Finite Element Method For Elliptic Problems in Composite Materials and Porous Media. *Journal of Computational Physics,* **134**, 169-189. DOI: http://dx.doi.org/10.1006/jcph.1997.5682

Jenny, P., Lee, S.H. and Tchelepi, H.A. 2003. Multi-scale Finite Volume Method for Elliptic Problems in Subsurface Flow Simulation. *Journal of Computational Physics,* **187** (1): 47-67.

Kelkar, M. and Perez, G. 2002. Applied Geostatistics for Reservoir Characterization. SPE Textbook Series. Richardson, Texas: Society of Petroleum Engineers.

King, M.J. 2007. Upgridding and Upscaling: Current Trends and Future Directions. Society of Petroleum Engineers. DOI: SPE-112810-DL

King, M.J. 2011. Upscaling of Geologic Models for Flow Simulation. College Station, Texas: Texas A&M University

King, M.J., Burn, K.S., Wang, P. et al. 2006. Optimal Coarsening of 3D Reservoir Models for Flow Simulation. Society of Petroleum Engineers. DOI: http://dx.doi.org/10.2118/95759-MS.

King, M.J., MacDonald, D.G., Todd, S.P. et al. 1998. Application of Novel Upscaling Approaches to the Magnus and Andrew Reservoirs. Society of Petroleum Engineers. DOI: http://dx.doi.org/10.2118/50643-MS.

King, P.R. 1989. The Use of Renormalization for Calculating Effective Permeability. *Transport in Porous Media,* **4** (1): 37-58. DOI: 10.1007/bf00134741

Lee, J. 1982. Well Testing. SPE Textbook Series. Richardson, Texas: Society of Petroleum Engineers.

Lee, S.H., Tchelepi, H.A., Jenny, P. and DeChant, L.J. 2002. Implementation of a Flux-Continuous Finite-Difference Method for Stratigraphic Hexahedron Grids. *SPE Journal,* **7** (03): 267-277. Society of Petroleum Engineers. DOI: http://dx.doi.org/10.2118/80117-PA

Nunna, K.C. 2014. Diffuse Source Transmissibility Upscaling. Master's thesis. Texas A&M University. Available electronically from http://hdl.handle.net/1969.1/153898.

Nunna, K.C., Zhou, P. and King, M.J. 2015. Novel Diffuse Source Pressure Transient Upscaling. Society of Petroleum Engineers. DOI: http://dx.doi.org/10.2118/173293-MS

Peszynska, M., Wheeler, M. F. and Yotov, I. 2002. Mortar Upscaling for Multiphase Flow in Porous Media. *Computational Geosciences*, **6**: 73-100.

Renard, P. and de Marsily, G. 1997. Calculating Equivalent Permeability: A Review. *Advances in Water Resources*, **20** (5-6): 253-278. DOI: http://dx.doi.org/10.1016/S0309-1708(96)00050-4

Sethian, J. 1999. Fast Marching Methods. *SIAM Review,* **41**(2): 199-235.

Tan, T.B. 1995. Estimating Two and Three Dimensional Pseudo-Relative Permeabilities with Non-Linear Regression. Society of Petroleum Engineers. DOI: http://dx.doi.org/10.2118/29129-MS.

Vasco, D.W., Keers, H. and Karasaki, K. 2000. Estimation of Reservoir Properties Using Transient Pressure Data: An Asymptotic Approach. *Water Resources Research,* **36** (12): 3447-3465. DOI: 10.1029/2000wr900179

Warren, J.E. and Price, H.S. 1961. Flow in Heterogeneous Porous Media. *Society of Petroleum Engineers Journal*, **1** (03): 153-169. Society of Petroleum Engineers. DOI: http://dx.doi.org/10.2118/1579-G.

Wen and Gómez-Hernández. 1996. Upscaling Hydraulic Conductivities in Heterogeneous Media: An Overview. *Journal of Hydrology,* **183** (1-2): ix-xxxii. DOI: http://dx.doi.org/10.1016/S0022-1694(96)80030-8

Zhang, Y., Bansal, N., Fujita, Y., Datta-Gupta, A., King, M.J., & Sankaran, S. 2014. From Streamlines to Fast Marching: Rapid Simulation and Performance Assessment of Shale Gas Reservoirs Using Diffusive Time of Flight as a Spatial Coordinate. Society of Petroleum Engineers. DOI: http://dx.doi.org/10.2118/168997-MS.

Zhou, Y. and King, M.J. 2011. Improved Upscaling for Flow Simulation of Tight Gas Reservoir Models. Society of Petroleum Engineers. DOI: http://dx.doi.org/10.2118/147355-MS.

APPENDIX A

DERIVATION of 1D PRESSURE AMPLITUDE EQUATION

In this appendix, I will start from **Eq. (2.11)** to develop a 1D pressure amplitude equation for a slightly compressible fluid in an isotropic medium. The derivation makes use of the eikonal equation and the assumption that $\mathrm{f}(\mathbf{x},\mathrm{s})$ is a function depending on $\tau(\mathbf{x})$ only. The governing equation is:

$$\nabla\cdot\big(\mathrm{k}(\mathbf{x})\nabla \mathrm{f}(\mathbf{x},\mathrm{s})\big)=\sqrt{\mathrm{s}}\big[\nabla\cdot\big(\mathrm{f}(\mathbf{x},\mathrm{s})\mathrm{k}(\mathbf{x})\nabla\tau(\mathbf{x})\big)+\nabla\tau(\mathbf{x})\cdot \mathrm{k}(\mathbf{x})\cdot\nabla \mathrm{f}(\mathbf{x},\mathrm{s})\big]\ \ldots\ldots\ldots\ldots(\mathrm{A}.1)$$

I introduce the diffusivity $\alpha=\mathrm{k}/\phi\mu \mathrm{c_t}$ to simplify our notations. Then **Eq. (A.1)** can be written as

$$\nabla\cdot\big(\phi \mathrm{c_t}\alpha\nabla \mathrm{f}(\mathbf{x},\mathrm{s})\big)=\sqrt{\mathrm{s}}\left[\nabla\cdot\big(\phi \mathrm{c_t}\alpha \mathrm{f}(\mathbf{x},\mathrm{s})\nabla\tau(\mathbf{x})\big)+\phi \mathrm{c_t}\frac{\partial \mathrm{f}}{\partial\tau}\right]\ \ldots\ldots\ldots\ldots\ldots\ldots\ldots\ldots\ldots\ldots.(\mathrm{A}.2)$$

On the left hand side of **Eq. (A.2)**, the term in the bracket can be written as

$$\phi \mathrm{c_t}\alpha\nabla \mathrm{f}(\mathbf{x},\mathrm{s})=\phi \mathrm{c_t}\alpha\frac{\partial \mathrm{f}}{\partial\tau}|\nabla\tau|\mathbf{n}_\tau\ \ldots\ldots\ldots\ldots\ldots\ldots\ldots\ldots\ldots\ldots\ldots\ldots\ldots\ldots\ldots\ldots\ldots\ldots\ldots\ldots\ldots\ldots.(\mathrm{A}.3.1)$$

Similarly, on the right hand side of **Eq. (A.2)**, the first term in the bracket can be written as

$$\phi \mathrm{c_t}\alpha \mathrm{f}(\mathbf{x},\mathrm{s})\nabla\tau(\mathbf{x})=\phi \mathrm{c_t}\alpha \mathrm{f}(\mathbf{x},\mathrm{s})|\nabla\tau|\mathbf{n}_\tau\ \ldots\ldots\ldots\ldots\ldots\ldots\ldots\ldots\ldots\ldots\ldots\ldots\ldots\ldots\ldots\ldots\ldots\ldots.(\mathrm{A}.3.2)$$

where $|\cdot|$ represents the magnitude of the vector $\nabla\tau$; $\mathbf{n}_\tau$ is the unit vector along $\nabla\tau$. Also, from the eikonal equation **Eq. (A.8)** we have

$$|\nabla\tau| = \frac{1}{\sqrt{\alpha}} \quad \ldots\ldots\ldots\ldots\ldots\ldots\ldots\ldots\ldots\ldots\ldots\ldots\ldots\ldots\ldots\ldots\ldots\ldots\ldots\ldots\ldots (\mathrm{A.4})$$

The above three equations yield the following equation

$$\nabla \cdot \left(\phi c_t \sqrt{\alpha} \frac{\partial f}{\partial \tau} \mathbf{n}_\tau\right) = \sqrt{s}\left[\nabla \cdot \left(\phi c_t \sqrt{\alpha} f(\mathbf{x}, s)\mathbf{n}_\tau\right) + \phi c_t \frac{\partial f}{\partial \tau}\right] \ldots\ldots\ldots\ldots\ldots\ldots\ldots\ldots\ldots\ldots\ldots (\mathrm{A.5})$$

Now we would like to do a coordinate transformation from (x, y, z) to (τ, ψ, κ) where τ is the diffusive time of flight. The other two coordinates, ψ and κ, are defined on the contour surfaces of τ and are orthogonal to each other and to τ. The divergence operator in the (τ, ψ, κ) coordinate system can be written as

$$\nabla \cdot \mathbf{V} = \frac{1}{h_\tau h_\psi h_\kappa}\left[\frac{\partial\left(h_\psi h_\kappa V_\tau\right)}{\partial \tau} + \frac{\partial\left(h_\kappa h_\tau V_\psi\right)}{\partial \psi} + \frac{\partial\left(h_\tau h_\psi V_\kappa\right)}{\partial \kappa}\right] \ldots\ldots\ldots\ldots\ldots\ldots\ldots\ldots\ldots\ldots\ldots (\mathrm{A.6})$$

where h_τ, h_ψ, h_κ are the length of the covariant vectors. Using **Eq. (A.6)**, we can write **Eq. (A.5)** as

$$\frac{1}{h_\tau h_\psi h_\kappa} \frac{\partial}{\partial \tau}\left(h_\psi h_\kappa \phi c_t \sqrt{\alpha} \frac{\partial f}{\partial \tau}\right) = \sqrt{s}\left[\frac{1}{h_\tau h_\psi h_\kappa} \frac{\partial}{\partial \tau}\left(h_\psi h_\kappa \phi c_t \sqrt{\alpha} f\right) + \phi c_t \frac{\partial f}{\partial \tau}\right] \ldots\ldots\ldots\ldots (\mathrm{A.7})$$

Since we have the following relation between the two coordinate systems:

$$\left(\frac{\partial x}{\partial \tau}\right)^2+\left(\frac{\partial y}{\partial \tau}\right)^2+\left(\frac{\partial z}{\partial \tau}\right)^2=h_\tau^2 \ldots\ldots\ldots\ldots\ldots\ldots\ldots\ldots\ldots\ldots\ldots\ldots\ldots\ldots\ldots\ldots\ldots\ldots\ldots\ldots\ldots\ldots (A.8.1)$$

$$\left(\frac{\partial \tau}{\partial x}\right)^2+\left(\frac{\partial \tau}{\partial y}\right)^2+\left(\frac{\partial \tau}{\partial z}\right)^2=\frac{1}{\alpha} \ldots\ldots\ldots\ldots\ldots\ldots\ldots\ldots\ldots\ldots\ldots\ldots\ldots\ldots\ldots\ldots\ldots\ldots\ldots\ldots\ldots\ldots. (A.8.2)$$

$$\frac{1}{h_\tau}\frac{\partial x}{\partial \tau}=h_\tau\frac{\partial \tau}{\partial x};\ \frac{1}{h_\tau}\frac{\partial y}{\partial \tau}=h_\tau\frac{\partial \tau}{\partial y};\ \frac{1}{h_\tau}\frac{\partial z}{\partial \tau}=h_\tau\frac{\partial \tau}{\partial z} \ldots\ldots\ldots\ldots\ldots\ldots\ldots\ldots\ldots\ldots\ldots\ldots\ldots\ldots.. (A.8.3)$$

Then we find that $h_\tau=\sqrt{\alpha}$ from **Eq. (A.8)**. Also, the Jacobian J of the (τ,ψ,κ) coordinate system is given by the following product

$$J=h_\tau h_\psi h_\kappa \ldots\ldots\ldots\ldots\ldots\ldots\ldots\ldots\ldots\ldots\ldots\ldots\ldots\ldots\ldots\ldots\ldots\ldots\ldots\ldots\ldots\ldots\ldots\ldots\ldots\ldots\ldots\ldots\ldots\ldots\ldots.. (A.9)$$

Therefore, **Eq. (A.7)** can be written as

$$\frac{\partial}{\partial \tau}\left(J\phi c_t\frac{\partial f}{\partial \tau}\right)=\sqrt{s}\left[\frac{\partial}{\partial \tau}(J\phi c_t f)+J\phi c_t\frac{\partial f}{\partial \tau}\right] \ldots\ldots\ldots\ldots\ldots\ldots\ldots\ldots\ldots\ldots\ldots\ldots\ldots\ldots\ldots\ldots (A.10)$$

The Jacobian J and the porosity ϕ are functions of (τ,ψ,κ). Next, we integrate both sides over the other two coordinates, ψ and κ, which are orthogonal to τ. Because the function f is assumed to be only a function of τ and t, it can be taken out of that integral. Thus **Eq. (A.10)** reduces to

$$\frac{\partial}{\partial \tau}\left(w(\tau)\frac{\partial f}{\partial \tau}\right)=\sqrt{s}\left[\frac{\partial}{\partial \tau}(w(\tau)f)+w(\tau)\frac{\partial f}{\partial \tau}\right] \ldots\ldots\ldots\ldots\ldots\ldots\ldots\ldots\ldots\ldots\ldots\ldots\ldots\ldots\ldots\ldots (A.11)$$

where

$$\mathrm{w}(\tau) = \iint \phi J(\tau, \psi, \kappa) d\psi d\kappa \ldots\ldots\ldots\ldots\ldots\ldots\ldots\ldots\ldots\ldots\ldots\ldots\ldots\ldots\ldots\ldots\ldots\ldots\ldots\ldots\ldots\ldots\ldots\ldots\ldots (A.12)$$

The total pore volume within the τ-contour can be obtained by integrating $\mathrm{w}(\tau)$ over τ

$$V_p(\tau) = \int_{\tau_0}^{\tau} \mathrm{w}(\bar{\tau}) d\bar{\tau} = \int_{\tau_0}^{\tau} \iint \phi J(\bar{\tau}, \psi, \kappa) d\psi d\kappa \, d\bar{\tau} \ldots\ldots\ldots\ldots\ldots\ldots\ldots\ldots\ldots\ldots\ldots\ldots\ldots\ldots (A.13)$$

The relation between $\mathrm{w}(\tau)$ and $V_p(\tau)$ is

$$\mathrm{w}(\tau) = \frac{dV_p(\tau)}{d\tau} \ldots\ldots\ldots\ldots\ldots\ldots\ldots\ldots\ldots\ldots\ldots\ldots\ldots\ldots\ldots\ldots\ldots\ldots\ldots\ldots\ldots\ldots\ldots\ldots\ldots\ldots\ldots (A.14)$$

This completes our derivation of 1D pressure amplitude equation for a slightly compressible fluid in an isotropic medium.